MATRIX-DOMINATED CONSTITUTIVE LAWS FOR COMPOSITE MATERIALS

A Thesis
Presented to
The Academic Faculty

by

Yihong He

In Partial Fulfillment
of the Requirements for the Degree
Doctor of Philosophy in the
School of Aerospace Engineering

Georgia Institute of Technology
August 2010

MATRIX-DOMINATED CONSTITUTIVE LAWS FOR THICK COMPOSITES

Approved by:

Professor Andrew Makeev, Advisor
School of Aerospace Engineering
Georgia Institute of Technology

Professor W. Steven Johnson
School of Material Science & Engineering
Georgia Institute of Technology

Professor and Chair Erian Armanios
Department of Mechanical and Aerospace Engineering
The University of Texas at Arlington

Professor Vitali Volovoi
School of Aerospace Engineering
Georgia Institute of Technology

Professor Dewey Hodges
School of Aerospace Engineering
Georgia Institute of Technology

Date Approved: 21 June 2010

ACKNOWLEDGEMENTS

It is my pleasure to acknowledge my advisor, Professor Andrew Makeev, for his patient guidance, helpful suggestions and consistent support throughout the development of my thesis.

I wish express my appreciation and gratitude to Professor Erian Armanios who provided me the opportunity to pursue my dreams in aerospace engineering. His help and guidance throughout my journey in Georgia Tech is unforgettable in my life.

I am grateful to Professors Dewey Hodges, Steven Johnson and Vitali Volovoi for serving on my thesis committee and providing valuable suggestions.

Special thanks to Paige Carpentier and Brian Shonkwiler for their efforts in experimental work. I would like to thank Dr. Yuri Nikishkov for providing valuable assistance with my numerical calculations. The support from Boeing and Bell Helicopter Textron Inc. for manufacturing the test specimens is also acknowledged.

I am also indebted to the School of Aerospace Engineering that made this achievement possible by funding my studies and research.

I feel very fortunate to having met some incredible friends, colleagues and teachers in my academic life. Without their help, this work would not have been possible. I thank them all.

I would like to extend my appreciation to my dear wife for her love, patience and sacrifices during the entire endeavor. I owe a great deal of gratitude to my parents and my brother for their unconditional support and love.

Most importantly, I want to praise Almighty God for the wisdom given to me from above through His love and grace to complete my thesis.

TABLE OF CONTENTS

LIST OF TABLES

LIST OF FIGURES

SUMMARY

Accurate three-dimensional stress-strain constitutive properties are essential to understanding complex deformation and failure mechanisms for materials with highly anisotropic mechanical properties. The large number of different methods and specimen types currently required to generate three-dimensional allowables for structural design slow down the material characterization. Also, some of the material constitutive properties are never measured due to prohibitive cost of the specimens needed. A method for measurement of three-dimensional constitutive properties using short-beam specimens subject to three-point bend load has been recently developed [39,40]. This method is based on the Digital Image Correlation (DIC) full-field deformation measurement and closed-form stress approximation. The purpose of this work is to improve the accuracy of the constitutive properties through accurate stress solution. A method is developed based on a combination of full-field strain measurement and nonlinear finite element stress analysis in the material characterization. The nonlinear shear stress-strain relations are the major concern in this work. An iterative procedure is applied to update the nonlinear shear properties using iterative finite element simulations. The accuracy of the numerical procedure is verified by comparing the finite element strain results with full-field measurements. The procedure is further verified using the V-notched beam test results. Excellent agreement has been achieved in the verification. Simplicity of the short-beam specimens and accuracy of the constitutive property approximations make the present method attractive for measurement of three-dimensional stress-strain relations for anisotropic materials at various load rates.

CHAPTER I

INTRODUCTION

1.1 Motivation

Analysis of mechanical behavior of materials and structures requires knowledge of material stress-strain constitutive properties. Growing acceptance of composite materials with highly-anisotropic mechanical properties for structural applications, and rapid development of large number of materials including glass and carbon-reinforced polymer-matrix composites, left accurate characterization of their constitutive properties behind. Structural analysis of composites requires accurate assessment of their three-dimensional stress and deformation states to understand complex failure mechanisms. Moreover, accurate through-the-thickness constitutive properties are especially important for structural analysis of thick composites. Examples of thick composite applications include rotor blade spar and blade-to-hub attachment structural details of rotary wing aircraft [25]. Glass/epoxy and carbon/epoxy tape materials are oftentimes used for manufacturing such structures.

Polymer-matrix composites exhibit nonlinear stress-strain behavior. In particular, the shear stress-strain relations are nonlinear for relatively low shear strains and the degree of nonlinearity varies from composite to composite. Figure 1.1 shows a typical interlaminar shear stress-strain response for a unidirectional S2-glass/E773-epoxy prepreg tape, measured by the test method presented in Chapter 3. Deviation from linearity may be observed in transverse loadings; however, the degree of nonlinearity is not comparable to that in the shear behavior [30, 35]. Moreover, the effect of the nonlinear matrix material on the longitudinal modulus E_1 and Poisson's ratio ν_{12} was shown with micromechanics analysis to be negligible for normal combinations of

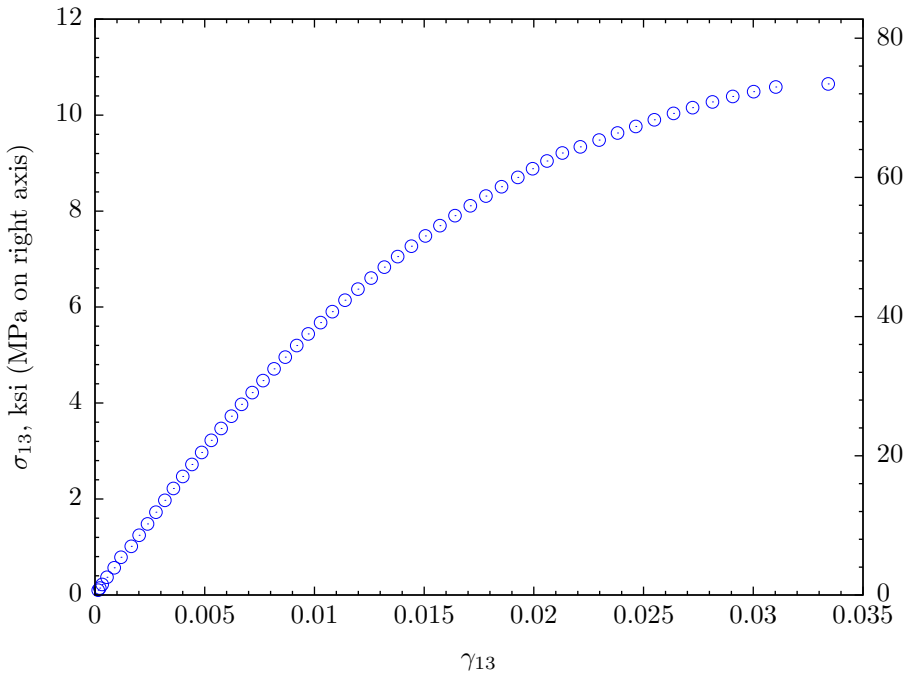

Figure 1.1: Interlaminar shear stress-strain response for a unidirectional S2-glass/E773-epoxy prepreg tape.

fibers and matrix materials [34].

Measuring shear properties is one of the difficult tasks in the characterization of composite materials [5]. Many shear test methods for composite materials have been developed. The five most popular current shear tests include the V-notched beam test, ASTM D 5379 [8]; the two- and three-rail shear tests, ASTM D 4255 [12]; the $[\pm 45^\circ]_{\text{ns}}$ tension test, ASTM D 3518 [13]; and the short-beam shear (SBS) test, ASTM D 2344 [11]. The ideal shear test method should provide a region of pure and uniform shear. None of the existing shear test methods completely satisfies this criterion. Furthermore, due to the anisotropic nature of composite materials and their nonlinear response in shear, experimental results obtained using these different methods are oftentimes inconsistent. Thus, the question remains as to which method is the most reliable [4, 66].

Standard techniques for assessment of stress-strain constitutive relations for materials are based on resistance strain gage measurements. As a strain gage measures

a "point" strain averaged through the gage area, such measurement imposes constraints on the test specimen designs. For example, strain gage measurements in the V-notched beam method drive high specimen cost: at least 19 mm (0.75 inches) thick laminate is required to machine specimens for strain gage placement; and tight geometry tolerances are imposed to minimize variations of strain at the gage location. Also, a large number of different test specimen types used for assessment of constitutive properties, including tensile, compressive, and shear stress-strain curves in the principal material planes [57], slow down the 3D material characterization process and increase cost of test materials.

Full-field strain measurement techniques enable additional flexibility for assessment of stress-strain relations, compared to conventional strain gages. High gradient strain distributions can be evaluated. Such flexibility could enable simpler test specimen design and reduce the number of different specimen types required for assessment of 3D stress-strain constitutive behavior. One such technique, Digital Image Correlation (DIC) [1, 55], is used in this work for full-field strain assessment of the SBS specimens.

The SBS specimens are simple to manufacture. The specimens are small, using a minimal amount of materials. In the SBS test, a specimen with a low span-to-thickness ratio (typically a ratio of 4 or 5) is subjected to three-point bending. Both axial bending and through-the-thickness shear stresses are induced. Based on the classical (mechanics of materials) beam theory assumptions, the axial bending stresses are compressive on the surface of the beam where the load is applied, and tensile on the opposite surface, varying linearity thorough the beam thickness if the longitudinal material response is linear; the shear stress varies parabolically from zero on each surface of the beam and reaches maximum in the neutral plane. However, due to the low span-to-thickness ratio, the concentrated loadings on the beam at the loading and support points may create stress concentrations throughout much of the short

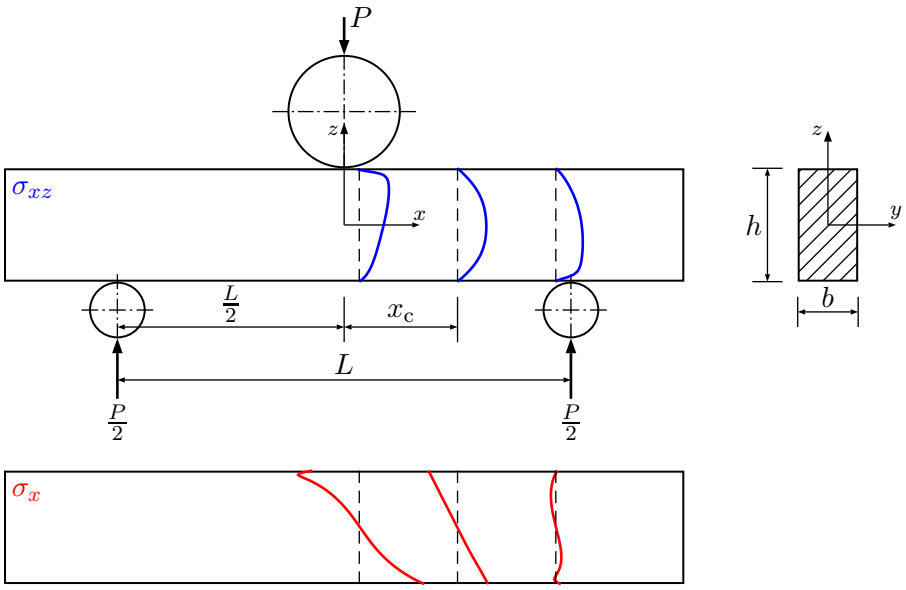

Figure 1.2: Geometry and stress distributions of the SBS specimens.

beam, complicating the stress state. As a result, the assumption of a parabolic stress distribution with a maximum at the neutral plane becomes only an approximation [4]. Figure 1.2 illustrates schematically the axial and shear stress distributions across various sections. The distributions were obtained from a nonlinear finite element model presented in Chapter 5. The numerical result indicates that the stress concentrations induced from the loading and support locations significantly affect the stress distributions of the short beam. Nevertheless, in the sections far away from loading and support locations (e.g., $x = \pm L/4$), the classical beam theory assumptions are often used due to small stress concentration effects. Indeed, ASTM standard D 2344 [11] assumes a parabolic shear stress distribution and suggests calculation of the short-beam shear strength F^{sbs} using the maximum shear stress from the classical beam theory:

$$F^{\text{sbs}} = \frac{3}{4}\frac{P_{\text{m}}}{A} \tag{1.1}$$

where, referring to Figure 1.2, P_{m} is the maximum load observed during the test and A is the cross-sectional area of the beam ($A = bh$). It is noted that, if the

material has different Young's moduli in tension and compression, the neutral plane shifts from middle-thickness and the shear stress distribution is no longer parabolically distributed across the thickness. In fact, one of the important characteristics of composite materials is that they often exhibit different elastic moduli in tension and compression [34]. Numerous investigations have been carried out to explore the behavior of bimodular composite beam, plate and shell structures within the last three decades [16,28]. However, the bimodular behavior was not considered in the previous studies of the SBS test.

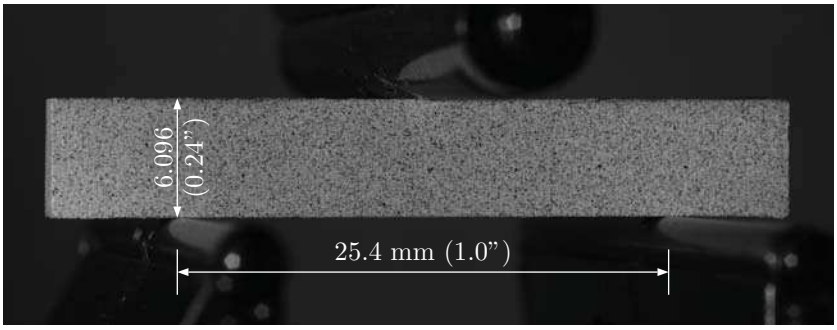

Figure 1.3: Random texture created using black and white spray paints on E-glass/5216-epoxy SBS test specimen surface.

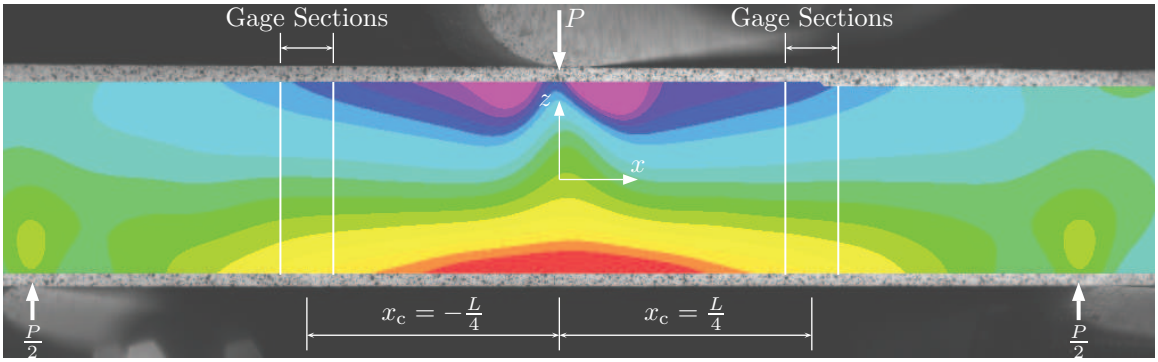

Figure 1.4: Gage sections for strain assessment from full field (DIC) measurement.

The high-gradient strain distributions in the SBS specimens prohibit the use of strain gages. According to Reference [11], instrumentation of SBS test coupons was

not practical, therefore modulus and stress-strain data could not be obtained. The DIC technique overcame the conventional strain gage limitations in the SBS tests since through-the-thickness strain distributions can be obtained from the full-field strain measurements. The DIC technique has been successfully used in Reference [39] for strain assessment in the nonlinear interlaminar shear stress-strain response of a glass/epoxy tape based on the SBS tests. The full-field strain measurement is based on tracking locations of random pattern using stereo images [39]. Figure 1.3 shows a random texture (pattern) created on a short-beam specimen surface using black and white spray paints. While the specimen is subject to load, a sequence of images is acquired using a stereo camera system. The full-field surface strain components are obtained based on an analysis of the stereo images. The VIC-3D [1] software is used in this work to determine three-dimensional positions before and after deformation by tracking the gray value pattern in small subsets throughout the acquired stereo image sequence. The Lagrange strain tensor components can then be obtained via numerical differentiation using the strain computation algorithm in the VIC-3D software. All three surface strain components, i.e., axial strain, transverse normal strain and shear strain, are obtained in a single DIC measurement. Figure 1.4 shows a typical axial stain contour plot for a unidirectional SBS specimen. As also illustrated in Figure 1.4, a number of gage sections, midway between the lower supports and the upper loading locations, are used to extract strain values from full-field measurement.

Numerous full-field strain measurements [39] have revealed that, on the gage sections of a SBS specimen, the axial strain is linearly distributed through the thickness. As an example, Figure 1.5 shows the typical axial strain distributions for a S2-glass/epoxy tape measured by the DIC technique. Linear through the thickness axial strain distributions in the SBS specimens enable simple closed-form solutions for the tensile and compressive moduli as well as shear stresses. As a consequence, the normal elastic moduli (Young's moduli) can be obtained from the axial stress-strain

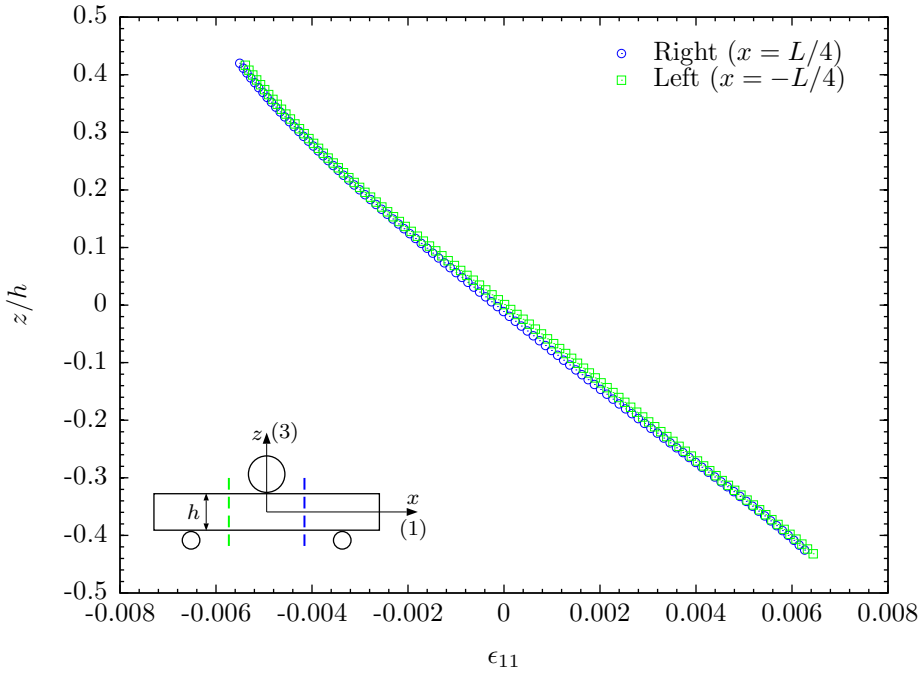

Figure 1.5: Typical axial stain distributions across gage sections of a unidirectional SBS specimen from DIC measurements.

response; the nonlinear shear stress-strain relations up to failure can be generated using the measured shear strains and the calculated shear stresses; and the Poisson's ratio can be calculated as the negative ratios of the transverse and axial strains at the bottom (tensile) surface. Moreover, by loading the SBS specimens in various material planes, a complete set of three-dimensional material properties can be characterized. The SBS specimens could be machined in the 0° and 90° directions from a single unidirectional panel and loaded in any one of the principal material planes. Figure 1.6 shows the principal material planes and corresponding properties measured from the SBS tests, where the subscript "T" denotes tensile property and "C" denotes compressive property, and K_{ij}, n_{ij} are parameters to characterize nonlinear shear behaviors. The method is recently applied to measure the 3D properties for several composite material systems and the material properties are reported in Reference [40].

Accuracy of stress calculation is essential in the material characterization. As mentioned before, the SBS test method, ASTM D 2444 [11], utilizes classical beam

Material Plane	Measured Properties
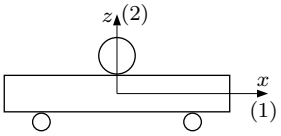	$E_{11\mathrm{T}}$, $E_{11\mathrm{C}}$, ν_{12}, G_{12}, K_{12}, n_{12}
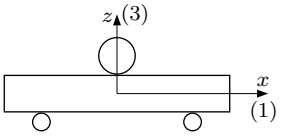	$E_{11\mathrm{T}}$, $E_{11\mathrm{C}}$, ν_{13}, G_{13}, K_{13}, n_{13}
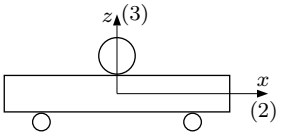	$E_{22\mathrm{T}}$, $E_{22\mathrm{C}}$, ν_{23}, G_{23}, K_{23}, n_{23}

Figure 1.6: Principal material planes and corresponding measured properties for the SBS tests.

theory as the basis for data reduction. The applicability of classical beam theory in the SBS test is questionable since normally a low span-to-thickness ratio is used for a SBS specimen. Furthermore, through-the-thickness shear distribution may become skewed due to the bimodular behavior, inducing additional error in material characterization. A number of studies, using elasticity solutions [52, 59] or finite element models [22, 23, 64, 66], have been conducted to investigate the accuracy of classical beam theory for the various short beam configurations and composite material systems. These studies have demonstrated inadequacies in classical beam theory in defining the shear stress state in the short beam configuration [11]. The deviation from classical beam theory is mainly due to the additional transverse stresses induced by the loading and support cylinders [5]. The stress analyses [22, 23, 52, 59, 64] reveal that the maximum shear stress predicted by the classical beam theory is never fully reached: the effect of nonlinear shear response was found to reduce the maximum shear stress. Consequently, the shear modulus is also overestimated if the closed-form approximation is used in the data reduction. It is worth noting that use of the

SBS test method for the development of design allowables for structural design criteria for composites was discouraged in the literature. Besides the existence of high strain gradient across the thickness, the discrepancy in closed-form approximation is another major reason. This is the reason for the use of "apparent" in the previous title of ASTM D 2344. Indeed, the SBS test is usually used for materials screening and quality control purpose in stead of properties measurement [4].

1.2 Objective and Approach

The purpose of this work is to improve the accuracy of the stress-strain constitutive relations through accurate stress solution. The nonlinear shear stress-strain relations are the major concern.

Finite element analysis provides a powerful tool to improve the accuracy of stress calculation, and consequently, the material characterization. In this work, nonlinear Finite Element Models (FEM) are developed for the SBS specimens and implemented in the material characterization to obtain accurate full-field stress state. Unlike conventional test methods using gage measurement and closed-form stress calculation, this work is a combination of full-field strain measurement and nonlinear finite element stress analysis.

The implementation of finite element analysis in the material characterization is achieved through an iterative procedure. The basic idea is to minimize the errors in stress calculation by using consecutive finite element simulations to update the stress prediction. Since material properties are necessary for a finite element model, the shear properties obtained from closed-form based stresses can be utilized as the initial approximation. Updated shear properties are generated using FE-based stresses. The finite element model can then be updated with the new shear properties. A subsequent finite element simulation is performed and shear properties are updated again using the obtained finite element results. Several iterations may be required

until the amount of update is within a tolerance and good agreement on strain survey has been achieved between finite element results and DIC data.

The composite material systems selected for the investigation are the unidirectional S2-glass/E773-epoxy prepreg tape, the unidirectional E-glass/5216-epoxy prepreg tape and the unidirectional IM7-carbon/8552-epoxy prepreg tape.

1.3 Outline

An outline of the reminder of this thesis is as follows.

A review on the available nonlinear constitutive models are given the following chapter. The nonlinear constitutive model used in this work is then implemented in the finite element code ABAQUS [24] via a user material subroutine.

Chapter 3 presents the method for assessment of 3D material properties for the three composite material systems using the SBS test and the DIC technique. The nonlinear shear stress-strain data are generated using the closed-form based stress approximation.

Various verification tests are performed in this work to validate the assumptions and accuracy of the SBS test. 0° and 90° tests are performed for the E-glass/5216-epoxy prepreg tape to demonstrate that the longitudinal and transverse stress-strain relations are linear to failure. V-notched beam tests are conducted to obtain shear stress-strain curves for the E-glass/5216-epoxy prepreg tape and the IM7-carbon/8552-epoxy prepreg tape. Angle beam tests are also performed to obtain the transverse Young's modulus and interlaminar tensile strength for the IM7-carbon/8552-epoxy prepreg tape. Chapter 4 presents these additional tests.

Chapter 5 is devoted to assessing the accuracy of closed-form stress approximation for the short beam configurations and the three composite material systems used in this work. The iterative procedure using the FE-based stresses is proposed to update the nonlinear shear properties obtained in Chapter 3.

The iterative procedure is performed in Chapter 6 to obtain updated shear properties for the three composite material systems under study. To verify the accuracy of the numerical procedure, the finite element strain results are compared with the DIC measurements. Moreover, the V-notched beam and SBS test results are correlated. As part of the verification program, the obtained nonlinear shear properties are implemented in finite element models to study the mechanical behavior of laminated SBS specimens and wrinkled specimens. Again, the finite element strain results are compared with the DIC measurements.

Conclusions and future work are stated in the final chapter.

CHAPTER II

NONLINEAR SHEAR STRESS-STRAIN RESPONSES

2.1 Nonlinear Constitutive Models for Shear Nonlinearity

A number of nonlinear constitutive models have been developed to study the shear nonlinearity in fiber reinforced composite materials [29–31, 35, 48, 53]. They can be classified into two categories, i.e., nonlinear elasticity models and inelasticity (plasticity) models, depending on whether the existence of permanent deformation upon unloading is assumed. The nonlinear elasticity models assume no permanent deformation upon unloading. They can also be classified based on whether the shear stress-strain behavior is treated as the sole source of material nonlinearity. Nonlinear transverse behavior is considered in some of the models. Three-dimensional effective stress/effective inelastic (plastic) strain models have also been used, in which nonlinear longitudinal behavior may be assumed as well.

The problems under monotonic loadings may be effectively described within the framework of the nonlinear theory of elasticity [30]. Simple mathematical representations, e.g., piecewise linear representations, polynomials, spline functions and Ramberg-Osgood equations are widely adopted.

Early work utilized piecewise approaches to describe the nonlinear behavior. Petit and Waddoups [45] used an incremental approach to determine the stress-strain of a lamina. Amijima and Adachi [14] introduced a simple technique to represent the shear nonlinearity using piecewise linear segments. Sandhu [49] used piecewise cubic spline functions to represent the lamina uniaxial test data and introduced a technique for solution of the nonlinear laminate equations.

Hahn and Tsai [30] used a complementary energy density polynomial function

for a lamina under plane stress state to derive a nonlinear stress-strain relation for laminated composites. An additional third-order term of the axial shear stress (γ_{12}) is added to the polynomial function for in-plane shear nonlinearity. The resulting model is linear in uniaxial loadings in the longitudinal and transverse plane stress (e.g., σ_{11} and σ_{22}), but nonlinear in axial shear stress with the following relation:

$$\gamma_{12} = \frac{\sigma_{12}}{G_{12}} + \alpha_{12}\sigma_{12}^3 \tag{2.1}$$

where α_{12} defines the nonlinearity of the shear stress-strain relation, being equal to zero for a linear shear response. This nonlinear elasticity model has been widely accepted as a candidate for curve fitting the shear stress-strain test data. Examples include, to name a few, the T300-graphite/976-epoxy, T300-graphite/934-epoxy [18] and IM7-carbon/8552-epoxy composites [17]. The equation is also used to characterize the nonlinear shear stress-strain responses in other principal material planes:

$$\gamma_{ij} = \frac{\sigma_{ij}}{G_{ij}} + \alpha_{ij}\sigma_{ij}^3, \quad ij = 12, 13, 23 \tag{2.2}$$

The Ramberg-Osgood equation [46], which is widely used in metal fatigue studies, is another popular model:

$$\gamma_{ij} = \frac{\sigma_{ij}}{G_{ij}} + \left(\frac{\sigma_{ij}}{K_{ij}}\right)^{\frac{1}{n_{ij}}}, \quad ij = 12, 13, 23 \tag{2.3}$$

where K_{ij} and n_{ij} are parameters that define the nonlinearity of the shear stress-strain relation. One of the early applications is due to Renieri and Herakovich [48] who used a quasi-three dimensional finite element analysis to model the response of laminates to thermal and mechanical loading. Nonlinear material properties were introduced via one dimensional Ramberg-Osgood representations.

Some more flexible mathematical representations were proposed simply for curve fitting purposes. For example, the following relation was used to fit the test data for XAS-carbon/914-epoxy composite [62, 63]:

$$\sigma_{12} = 71.41 + 3.66\gamma_{12} - 91.52e^{-\gamma_{12}} + 20.11e^{-2\gamma_{12}} \tag{2.4}$$

Where σ_{12} is the shear stress in MPa, and γ_{12} is the shear strain in %.

The nonlinearities in fiber-reinforced composites can also be treated as plastic behavior. Several nonlinear constitutive models were formulated based on classical incremental plasticity. Hill's yield function, or various modifications, is widely adopted as the yield function. Isotropic strain hardening is often assumed. Kinematic strain hardening or mixed isotropic/kinematic hardening is also used.

Hashin et al. [31] formulated a nonlinear constitutive model where inelastic transverse and axial shear strains exist in a lamina under plane stress conditions. Each inelastic strain component is an independent quadratic function in terms of the stress invariants raised to a general power. The Ramberg-Osgood representation was used to express the nonlinear axial-shear and transverse stress-strain relations.

A three-dimensional theory based on Hill's orthotropic yield criterion and the incremental flow theory was developed by Griffin et al. [29]. It was assumed that the uniaxial stress-strain relations in principal material directions are given in a Ramberg-Osgood form

$$\epsilon_i = \frac{\sigma_i}{E_i} + \beta_i \left(\sigma_i\right)^{n_i}, \quad i = 1, \ldots, 6 \tag{2.5}$$

Thus, the uniaxial plastic strain is assumed to be the power lower portion of the approximation, i.e., $\epsilon_i^{\mathrm{p}} = \beta_i \left(\sigma_i\right)^{n_i}$. The assumption of incompressibility of plastic strains for the Hill-type criterion was enforced for the sake of consistency:

$$\sum_{i=1}^{3} \epsilon_i^{\mathrm{p}} = 0 \tag{2.6}$$

Sun and Chen [53] developed a one parameter orthotropic plasticity model for thermoplastic and metal-matrix composite laminates in plane stress. One-parameter plastic-potential scalar function is proposed in their model. Only transverse and axial shear stresses are involved in the plastic model; therefore, plastic deformation in the axial direction of the lamina is neglected. In addition, a power law relation between

effective plastic strain and the effective stress is proposed; as a results, a total of three-material parameters are needed to fully describe the lamina plastic behavior. The nonlinear parameters were determined by a trial and error optimization from stress-strain responses of simple off-axis tension tests under various loading conditions. The plane stress model was later extended to a three-dimensional model [20].

The Ramberg-Osgood equation is used in this work to fit the nonlinear shear stress-strain responses measured from the SBS tests. Figure 1.1 (on Page 2) shows a typical shear stress-strain response for a unidirectional S2-glass/E773-epoxy tape SBS specimen loaded in 1-3 material plane. The linear shear modulus (e.g., G_{13} in the 1-3 material plane) is determined from linear interpolation of the shear stress-strain data in the small strain regime (e.g., $\gamma_{13} < 0.01$). While the nonlinear parameters (e.g., K_{13} and n_{13} in the 1-3 material plane) are determined from logarithmic linear interpolation of the shear stress-strain data in the large strain regime.

The elastic stress-strain relations for orthotropic material is modified to account for the nonlinear shear behavior:

$$\begin{Bmatrix} \epsilon_{11} \\ \epsilon_{22} \\ \epsilon_{33} \\ \gamma_{23} \\ \gamma_{13} \\ \gamma_{12} \end{Bmatrix} = \begin{bmatrix} \frac{1}{E_1} & -\frac{\nu_{21}}{E_2} & -\frac{\nu_{31}}{E_3} & 0 & 0 & 0 \\ -\frac{\nu_{12}}{E_1} & \frac{1}{E_2} & -\frac{\nu_{32}}{E_3} & 0 & 0 & 0 \\ -\frac{\nu_{13}}{E_1} & -\frac{\nu_{23}}{E_2} & \frac{1}{E_3} & 0 & 0 & 0 \\ 0 & 0 & 0 & \frac{1}{G_{23}} & 0 & 0 \\ 0 & 0 & 0 & 0 & \frac{1}{G_{13}} & 0 \\ 0 & 0 & 0 & 0 & 0 & \frac{1}{G_{12}} \end{bmatrix} \begin{Bmatrix} \sigma_{11} \\ \sigma_{22} \\ \sigma_{33} \\ \sigma_{23} \\ \sigma_{13} \\ \sigma_{12} \end{Bmatrix} + \begin{bmatrix} 0 & 0 & 0 & 0 & 0 & 0 \\ 0 & 0 & 0 & 0 & 0 & 0 \\ 0 & 0 & 0 & 0 & 0 & 0 \\ 0 & 0 & 0 & \frac{1}{K_{23}}\left(\frac{\sigma_{23}}{K_{23}}\right)^{\frac{1}{n_{23}}-1} & 0 & 0 \\ 0 & 0 & 0 & 0 & \frac{1}{K_{13}}\left(\frac{\sigma_{13}}{K_{13}}\right)^{\frac{1}{n_{13}}-1} & 0 \\ 0 & 0 & 0 & 0 & 0 & \frac{1}{K_{12}}\left(\frac{\sigma_{12}}{K_{12}}\right)^{\frac{1}{n_{12}}-1} \end{bmatrix} \begin{Bmatrix} \sigma_{11} \\ \sigma_{22} \\ \sigma_{33} \\ \sigma_{23} \\ \sigma_{13} \\ \sigma_{12} \end{Bmatrix} \tag{2.7}$$

in which

$$\frac{\nu_{12}}{E_1} = \frac{\nu_{21}}{E_2}, \quad \frac{\nu_{13}}{E_1} = \frac{\nu_{31}}{E_3}, \quad \frac{\nu_{23}}{E_2} = \frac{\nu_{32}}{E_3} \tag{2.8}$$

The second term in equation (2.7) is the contribution of nonlinear shear behavior. Several assumptions are implied in the nonlinear constitutive model (2.7):

1. The shear stress-strain behavior is treated as the sole source of material nonlinearity.

2. The nonlinear shear properties are introduced via one-dimensional Ramberg-Osgood representations.

3. Couplings of shear and normal stresses in nonlinear behavior are ignored.

In the present work only monotonic loading condition is considered. Therefore, the nonlinear elastic constitutive formulation is appropriate.

2.2 Implementation of Nonlinear Constitutive Model in Finite Element Analysis

To implement the nonlinear constitutive model (2.7) in commercial finite element codes, a user material subroutine (e.g., the UMAT subroutine in ABAQUS) is needed. Typically, two tasks must be executed in a user material subroutine: the tangent stiffness matrix (material Jacobian) must be provided for the implicit analysis; and the stresses at the end of the (pseudo-)time increment ($t + \Delta t$) must be updated. The implementation of the Ramberg-Osgood shear model in the plane stress analysis is derived in the following. The procedure can be easily extended to the three-dimensional case.

According to equation (2.7), the in-plane stress-strain relations for a lamina with

nonlinear shear behavior can be expressed as

$$\begin{Bmatrix} \epsilon_{11} \\ \epsilon_{22} \\ \gamma_{12} \end{Bmatrix} = \begin{bmatrix} \frac{1}{E_1} & -\frac{\nu_{21}}{E_2} & 0 \\ -\frac{\nu_{12}}{E_1} & \frac{1}{E_2} & 0 \\ 0 & 0 & \frac{1}{G_{12}} \end{bmatrix} \begin{Bmatrix} \sigma_{11} \\ \sigma_{22} \\ \sigma_{12} \end{Bmatrix} + \begin{bmatrix} 0 & 0 & 0 \\ 0 & 0 & 0 \\ 0 & 0 & \frac{1}{K_{12}} \left(\frac{\sigma_{12}}{K_{12}} \right)^{\frac{1}{n_{12}}-1} \end{bmatrix} \begin{Bmatrix} \sigma_{11} \\ \sigma_{22} \\ \sigma_{12} \end{Bmatrix} \tag{2.9}$$

in which

$$\frac{\nu_{21}}{E_2} = \frac{\nu_{12}}{E_1} \tag{2.10}$$

The second term in equation (2.9) represents in-plane nonlinear shear response contribution.

The incremental constitutive equation is obtained by differentiating equation (2.9)

$$\begin{Bmatrix} \Delta\epsilon_{11} \\ \Delta\epsilon_{22} \\ \Delta\gamma_{12} \end{Bmatrix} = \begin{bmatrix} \frac{1}{E_1} & -\frac{\nu_{21}}{E_2} & 0 \\ -\frac{\nu_{12}}{E_1} & \frac{1}{E_2} & 0 \\ 0 & 0 & \frac{1}{G_{12}} \end{bmatrix} \begin{Bmatrix} \Delta\sigma_{11} \\ \Delta\sigma_{22} \\ \Delta\sigma_{12} \end{Bmatrix} + \begin{bmatrix} 0 & 0 & 0 \\ 0 & 0 & 0 \\ 0 & 0 & \frac{1}{n_{12}}\frac{1}{K_{12}} \left(\frac{\sigma_{12}}{K_{12}} \right)^{\frac{1}{n_{12}}-1} \end{bmatrix} \begin{Bmatrix} \Delta\sigma_{11} \\ \Delta\sigma_{22} \\ \Delta\sigma_{12} \end{Bmatrix} \tag{2.11}$$

Inverting the above equation yields

$$\begin{Bmatrix} \Delta\sigma_{11} \\ \Delta\sigma_{22} \\ \Delta\sigma_{12} \end{Bmatrix} = \begin{pmatrix} \frac{E_1}{1-\nu_{12}\nu_{21}} & \frac{\nu_{12}E_2}{1-\nu_{12}\nu_{21}} & 0 \\ \frac{\nu_{21}E_1}{1-\nu_{12}\nu_{21}} & \frac{E_2}{1-\nu_{12}\nu_{21}} & 0 \\ 0 & 0 & \frac{1}{\frac{1}{G_{12}}+\frac{1}{n_{12}}\frac{1}{K_{12}}\left(\frac{\sigma_{12}}{K_{12}}\right)^{\frac{1}{n_{12}}-1}} \end{pmatrix} \begin{Bmatrix} \Delta\epsilon_{11} \\ \Delta\epsilon_{22} \\ \Delta\gamma_{12} \end{Bmatrix} \tag{2.12}$$

As a result, the material Jacobian $\mathbf{J}$ for the Ramberg-Osgood shear model is given by

$$\mathbf{J} = \begin{pmatrix} \frac{\Delta\sigma_{11}}{\Delta\epsilon_{11}} & \frac{\Delta\sigma_{11}}{\Delta\epsilon_{22}} & \frac{\Delta\sigma_{11}}{\Delta\gamma_{12}} \\ \frac{\Delta\sigma_{22}}{\Delta\epsilon_{11}} & \frac{\Delta\sigma_{22}}{\Delta\epsilon_{22}} & \frac{\Delta\sigma_{22}}{\Delta\gamma_{12}} \\ \frac{\Delta\sigma_{12}}{\Delta\epsilon_{11}} & \frac{\Delta\sigma_{12}}{\Delta\epsilon_{22}} & \frac{\Delta\sigma_{12}}{\Delta\gamma_{12}} \end{pmatrix} = \begin{pmatrix} \frac{E_1}{1-\nu_{12}\nu_{21}} & \frac{\nu_{12}E_2}{1-\nu_{12}\nu_{21}} & 0 \\ \frac{\nu_{21}E_1}{1-\nu_{12}\nu_{21}} & \frac{E_2}{1-\nu_{12}\nu_{21}} & 0 \\ 0 & 0 & \frac{1}{\frac{1}{G_{12}}+\frac{1}{n_{12}}\frac{1}{K_{12}}\left(\frac{\sigma_{12}}{K_{12}}\right)^{\frac{1}{n_{12}}-1}} \end{pmatrix} \tag{2.13}$$

In the nonlinear finite element analysis, the stress at the end of the current time increment ($\boldsymbol{\sigma}|_{t+\Delta t}$) is updated by summation of the initial value at the beginning of

the current time increment ($\boldsymbol{\sigma}|_t$) and the incremental values ($\Delta\boldsymbol{\sigma}$) solved from the system of nonlinear equations:

$$\begin{Bmatrix} \sigma_{11} \\ \sigma_{22} \\ \sigma_{12} \end{Bmatrix}^{t+\Delta t} = \begin{Bmatrix} \sigma_{11} \\ \sigma_{22} \\ \sigma_{12} \end{Bmatrix}^{t} + \begin{Bmatrix} \Delta\sigma_{11} \\ \Delta\sigma_{22} \\ \Delta\sigma_{12} \end{Bmatrix} \tag{2.14}$$

The updated normal stresses at the end of the time increment can be determined by substituting equation (2.12) into equation (2.14):

$$\begin{Bmatrix} \sigma_{11} \\ \sigma_{22} \end{Bmatrix}^{t+\Delta t} = \begin{Bmatrix} \sigma_{11} \\ \sigma_{22} \end{Bmatrix}^{t} + \begin{pmatrix} \frac{E_1}{1-\nu_{12}\nu_{21}} & \frac{\nu_{12}E_2}{1-\nu_{12}\nu_{21}} \\ \frac{\nu_{21}E_1}{1-\nu_{12}\nu_{21}} & \frac{E_2}{1-\nu_{12}\nu_{21}} \end{pmatrix} \begin{Bmatrix} \Delta\epsilon_{11} \\ \Delta\epsilon_{22} \end{Bmatrix} \tag{2.15}$$

An iterative procedure is required to obtain the updated shear stress as the shear stress-strain relation is nonlinear. The Newton-Raphson method is used and the shear stress increment for the current iteration i is updated by

$${}^{i}\Delta\sigma_{12} = \frac{\gamma_{12}^{t+\Delta t} - \frac{{}^{i}\sigma_{12}}{G_{12}} - \left(\frac{{}^{i}\sigma_{12}}{K_{12}}\right)^{\frac{1}{n_{12}}}}{\frac{1}{G_{12}} + \frac{1}{n_{12}}\frac{1}{K_{12}}\left(\frac{{}^{i}\sigma_{12}}{K_{12}}\right)^{\frac{1}{n_{12}}-1}} \tag{2.16}$$

The total shear stress increment at the end of the current time increment ($t + \Delta t$) is the sum of the shear stress increments during the Newton-Raphson iterations:

$$\Delta\sigma_{12} = \sum_{i=1}^{N} {}^{i}\Delta\sigma_{12} \tag{2.17}$$

where N is the total number of iterations that have been performed for the converged stress increment $\Delta\sigma_{12}$. Numerical experiments show that the shear-stress update procedure requires only a few number of iterations to achieve satisfactory numerical accuracy.

The nonlinear shear model is implemented in the commercial finite element code ABAQUS [24]. A numerical test with one element model is performed to validate the numerical accuracy. As shown in Figure 2.1, the element is subjected to positive

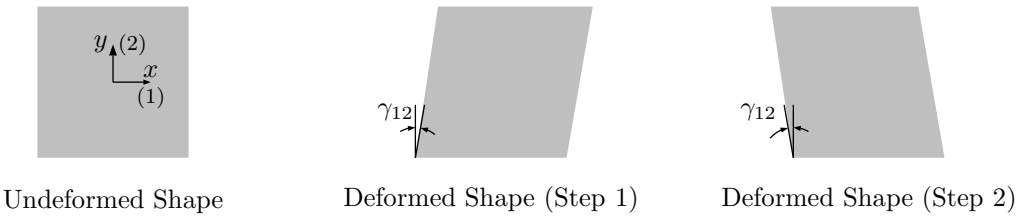

Figure 2.1: Undeformed and deformed shapes of a finite element subjected to pure shear.

pure shear at the first step of the analysis, followed by a reversed loading in step two. The first-order plane stress element with reduced integration (i.e., CPS4R) is used so that the model contains only one Gauss point located at the element center. The following engineering constants

$$E_1 = 47.5\,\text{GPa}, \quad E_2 = 12.5\,\text{GPa}, \quad \nu_{12} = 0.29, \quad G_{12} = 4.24\,\text{GPa}$$

and nonlinear shear parameters

$$K_{12} = 183.1\,\text{MPa}, \quad n_{12} = 0.226$$

are used for a unidirectional glass/epoxy tape. The shear stress-strain data were extracted at the Gauss point and plotted in Figure 2.2. The accuracy of numerical modeling is clearly indicated in the figure - the incremental solution procedure follows the nonlinear shear model.

2.3 Closing Remarks

The implementation procedure can be applied to other nonlinear elasticity model with minor modifications. For example, the material Jacobian **J** for the third-order

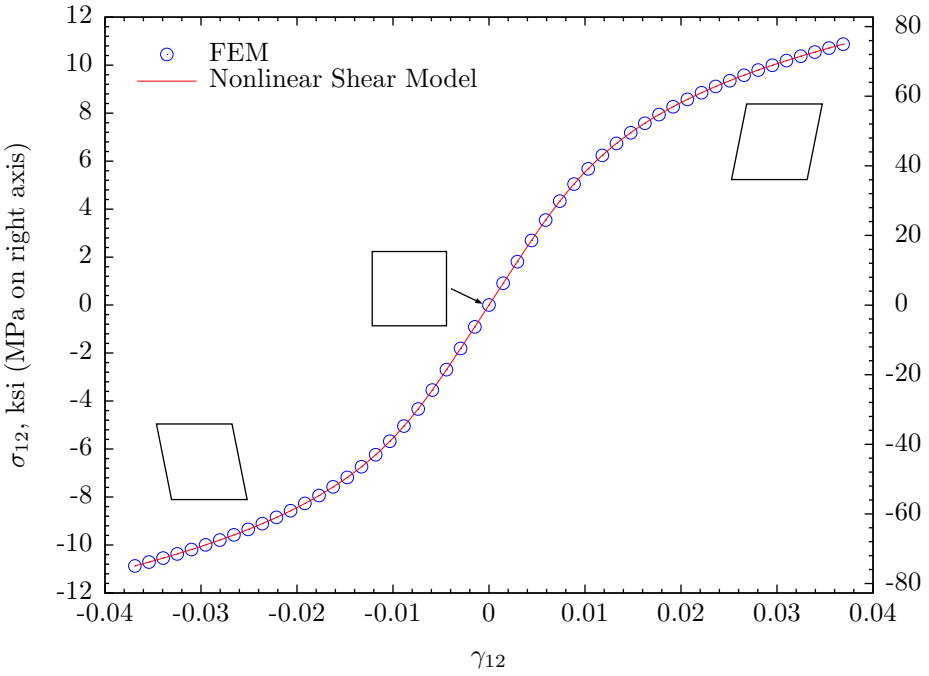

Figure 2.2: Nonlinear shear stress-strain response at Gauss point.

polynomial model (2.1) is given by

$$\mathbf{J} = \begin{pmatrix} \frac{\Delta\sigma_{11}}{\Delta\epsilon_{11}} & \frac{\Delta\sigma_{11}}{\Delta\epsilon_{22}} & \frac{\Delta\sigma_{11}}{\Delta\gamma_{12}} \\ \frac{\Delta\sigma_{22}}{\Delta\epsilon_{11}} & \frac{\Delta\sigma_{22}}{\Delta\epsilon_{22}} & \frac{\Delta\sigma_{22}}{\Delta\gamma_{12}} \\ \frac{\Delta\sigma_{12}}{\Delta\epsilon_{11}} & \frac{\Delta\sigma_{12}}{\Delta\epsilon_{22}} & \frac{\Delta\sigma_{12}}{\Delta\gamma_{12}} \end{pmatrix} = \begin{pmatrix} \frac{E_1}{1-\nu_{12}\nu_{21}} & \frac{\nu_{12}E_2}{1-\nu_{12}\nu_{21}} & 0 \\ \frac{\nu_{21}E_1}{1-\nu_{12}\nu_{21}} & \frac{E_2}{1-\nu_{12}\nu_{21}} & 0 \\ 0 & 0 & \frac{1}{\frac{1}{G_{12}}+3\alpha_{12}\sigma_{12}^2} \end{pmatrix} \tag{2.18}$$

and the shear stress update in the Newton-Raphson iteration (2.16) becomes

$$^i\Delta\sigma_{12} = \frac{\gamma_{12}^{t+\Delta t} - \frac{^i\sigma_{12}}{G_{12}} - \alpha_{12}\,{}^i\sigma_{12}^3}{\frac{1}{G_{12}} + 3\alpha_{12}\,{}^i\sigma_{12}^2} \tag{2.19}$$

The mathematical simplicity of Ramberg-Osgood equation (2.3) enables the implementation of the nonlinear shear model in the closed-form solutions for laminated composites. As an example, the implementation in Classical Laminate Theory (CLT) is demonstrated in Appendix A.

CHAPTER III

TEST PROCEDURE FOR MEASUREMENT OF THREE-DIMENSIONAL CONSTITUTIVE PROPERTIES

3.1 Experiment Description

The SBS test consists of a short-beam specimen of rectangular cross-section loaded in three-point bending so that an interlaminar shear failure occurs. A typical test configuration and specimen geometry is shown in Figure 3.1. The specimen rests on two support cylinders that allow lateral motion, and the load is applied through a loading cylinder located at the mid-span of the specimen. Typically, the loading cylinder is 6.3 mm (0.25 inches) in diameter, and the two support cylinders are 3.1 mm (0.125 inches) in diameter. A span-to-thickness ratio (L/h) of four to five is usually used. ASTM Standard D 2344 [11] also recommends that the specimen overhang the support rollers by at least one specimen thickness. In addition, a width-to-thickness ratio (b/h) of two is suggested since a ratio greater than two can result in a significant width-wise shear stress variation [5].

In the present work the ASTM SBS geometry and supports were modified [40]. The SBS specimen thickness ranges from 3.6 mm (0.14 inches) for carbon/epoxy to 6.4 mm (0.25 inches) for glass/epoxy material systems. The width is reduced from the ASTM recommended 200% to about 100% of the specimen thickness for more uniform strain distributions though the width away from the support locations. Also, the loading nose (upper support) diameter is increased from the ASTM standard [11] of 6.4 mm (0.25 inches) to 12.7 mm (0.5 inches) except for the tests of E-glass/5216-epoxy SBS specimens to reduce compressive damage under the loading nose. Compressive damage issues also result in the reduced SBS specimen thickness

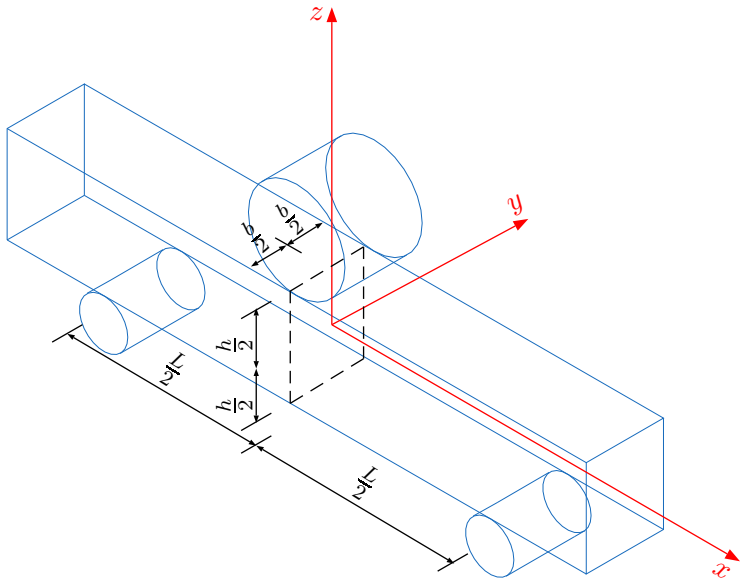

Figure 3.1: Experimental assembly approximation and coordinate notation for SBS testing.

required for carbon/epoxy compared to the more compliant glass/epoxy composite material systems. The standard [11] lower support diameter of 3.2 mm (0.125 inches) is used.

Glass/epoxy and carbon/epoxy unidirectional tape composite SBS specimens machined and loaded in the principal material planes are considered in this work. Conventional material coordinate notations [34] are utilized. The fiber direction is denoted as 1 (0°); the in-ply transverse direction as 2 (90°); and the laminate thickness direction as 3 (interlaminar direction). The principal material planes are denoted as 1-2 (in-ply), 2-3, and 1-3 (interlaminar planes). The global coordinate system is identified in Figure 3.1. As shown in Figure 1.6 (Page 8), by orientating the specimen's longitudinal axis along any one of the three axes of material orthotropy in the test fixture, any one of the material planes can be measured. Shown in Figure 3.2, the SBS specimens are placed in a servohydraulic load frame and subject to monotonic load at 1.0 mm/min (0.05 in./min) crosshead displacement rate till failure. Figure

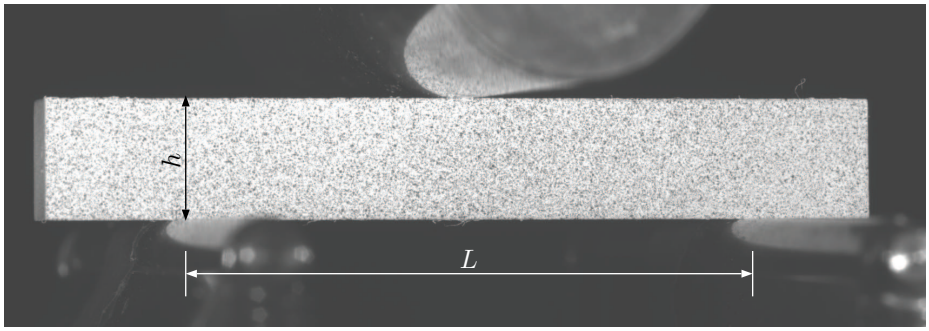

Figure 3.2: Unidirectional S2-glass/E773-epoxy tape SBS specimen geometry and random surface texture created using black and white spray paints.

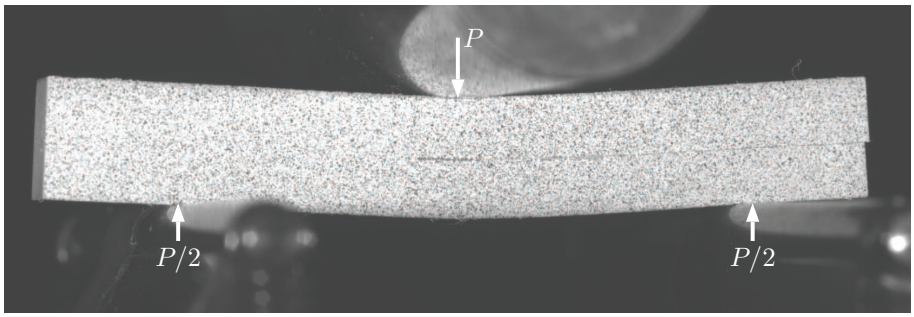

Figure 3.3: Loading conditions and ultimate shear failure of a unidirectional S2-glass/E773-epoxy tape SBS specimen.

3.3 shows a typical shear failure which started between the loading nose and a lower support and propagated to the specimen edge.

As illustrated in Figure 1.4 (on Page 5), a number of gage sections, mid-way between the lower supports and the upper support locations, are used to extract strain values from the full field measurement for the assessment of the tensile, compressive, and shear stress-strain material behavior. The strain values are averaged through the gage sections to minimize noise effects at low strains. Figure 3.4 shows typical measured distributions extracted from several gage sections, for axial strain and shear strain, respectively. Both distributions show low scatter.

Normal elastic moduli (Young's moduli) are obtained from the axial stress-stress

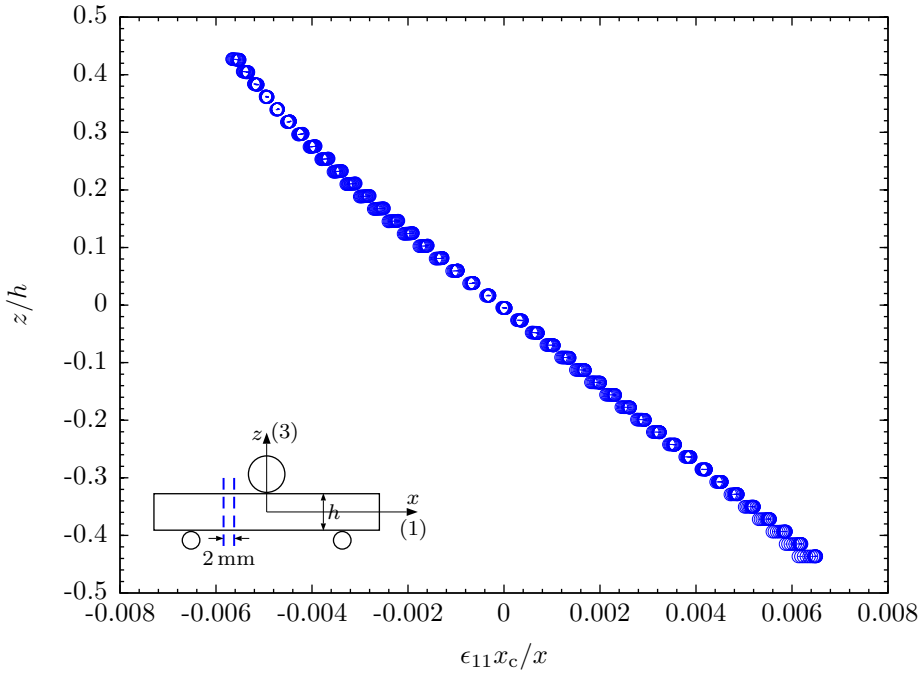

(a)

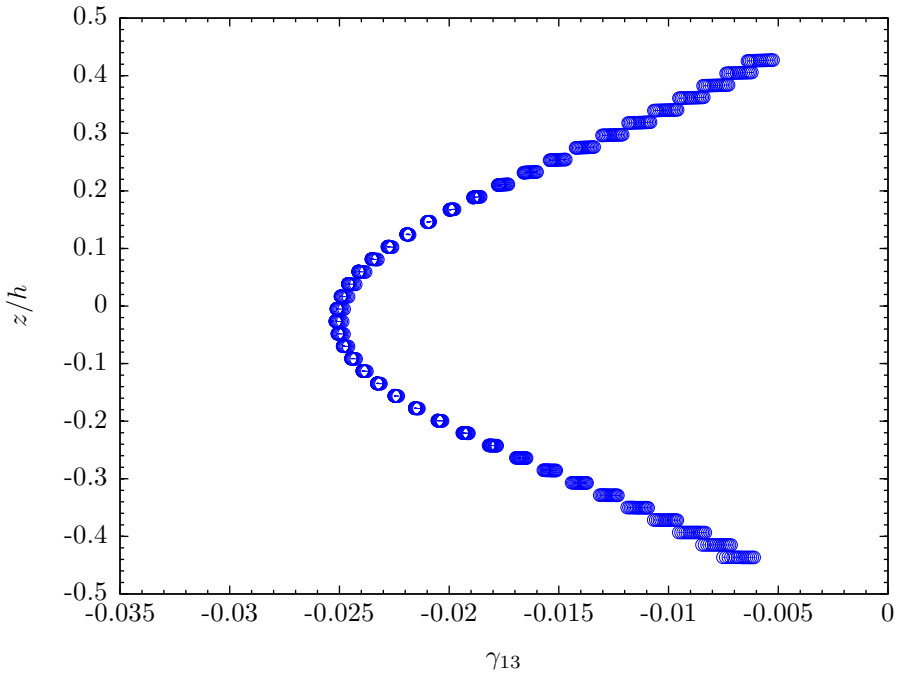

(b)

Figure 3.4: Strain distributions across thickness of a number of gage sections for a S2-glass/E773-epoxy tape SBS specimen at load 3501 N (787 lbs) 95% failure load in the 1-3 material plane (Specimen S3). (a) Normalized axial strain; (b) Shear strain.

responses. Both axial stress and strain distributions are assumed linear across the thickness of gage sections. Some composite systems may have significant difference in tensile modulus and compressive modulus. Consequently, the neutral plane does not necessarily pass through mid-thickness and both tensile modulus E_{T} and compressive modulus E_{C} can be measured.

It is in the neutral plane that the shear stress is theoretically at maximum. The stress state should be pure shear in the neutral plane. Therefore, the maximum shear stress-strain data are used to obtain the shear properties. The Ramberg-Osgood representations, i.e., equation (2.3)

$$\gamma_{ij} = \frac{\sigma_{ij}}{G_{ij}} + \left(\frac{\sigma_{ij}}{K_{ij}}\right)^{\frac{1}{n_{ij}}}, \quad ij = 12,\ 13,\ \text{or}\ 23 \tag{2.3}$$

were used to interpret the experimental results using a least squares approximation.

3.2 Closed-Form Stress and Modulus Approximations

Deformation measurements for several glass/epoxy and carbon/epoxy unidirectional tape composites under quasi-static loading conditions show (a) close to linear axial strain distributions through the SBS specimen thickness far from the support locations at loads close to failure, and (b) linear tensile and compressive stress-strain response till failure. Figures 3.5, 3.6 and 3.7 illustrate axial strain distributions through the thickness for three S2-glass/E773-epoxy composite SBS specimens loaded in the 1-3, 1-2 and 2-3 material plane, respectively. The transverse coordinate z is normalized with respect to the specimen thickness h in the plane of loading.

Linear through the thickness axial distributions in the SBS specimens [40] enable simple closed-form solutions for the tensile and compressive moduli as well as shear stresses. As illustrated schematically in Figure 3.8, a linear axial strain approximation through the thickness is

$$\epsilon_x = -ky - e, \quad -\frac{h}{2} \leqslant y \leqslant \frac{h}{2} \tag{3.1}$$

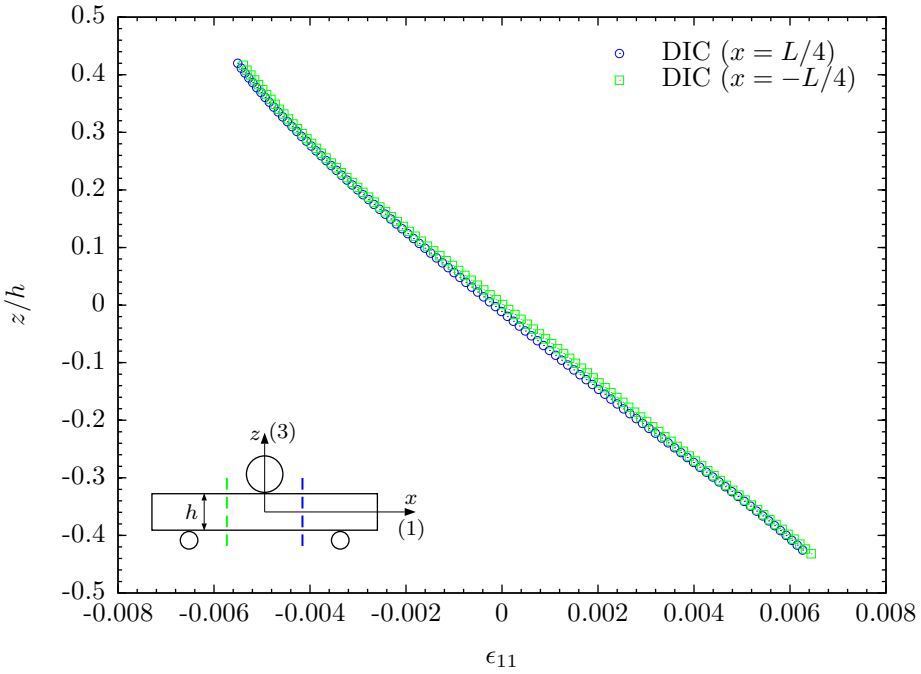

Figure 3.5: Through thickness axial strain distributions for a S2-glass/E773-epoxy tape SBS specimen at load 3501 N (787 lbs) 95% failure load in the 1-3 material plane (Specimen S3).

Figure 3.8 shows the reference coordinate system, which is different from the global coordinate system shown in Figure 3.1 for convenience in derivation.

The thickness coordinate $y = -e/k$ corresponds to the neutral plane location. Neglect the transverse normal stresses away from the support locations and express the linear axial tensile and compressive stress-strain relations (Hooke's Law) as

$$\sigma_x = \begin{cases} E_{\mathrm{T}}\epsilon_x, & -\frac{h}{2} \leqslant y \leqslant -\frac{e}{k} \\ E_{\mathrm{C}}\epsilon_x, & -\frac{e}{k} < y \leqslant \frac{h}{2} \end{cases} \tag{3.2}$$

where E_{T} and E_{C} denote the tensile and compressive moduli. The axial force and bending moment approximations for the specimen cross-section are

$$N = \iint\limits_{\substack{-\frac{h}{2}\leqslant y\leqslant\frac{h}{2} \\ -\frac{b}{2}\leqslant z\leqslant\frac{b}{2}}} \sigma_x \, dydz = 0 \tag{3.3}$$

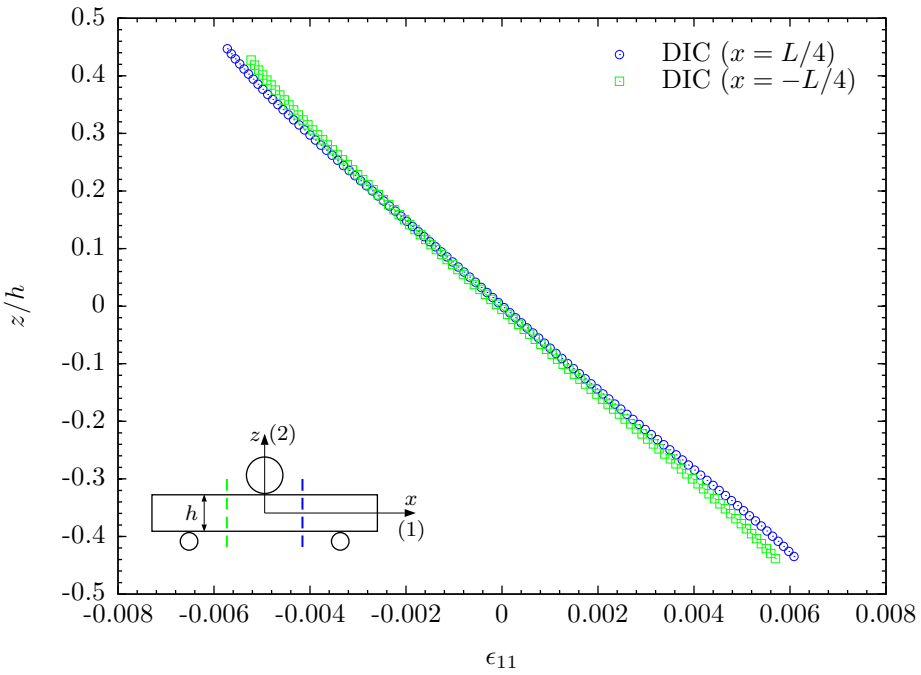

Figure 3.6: Through thickness axial strain distributions for a S2-glass/E773-epoxy tape SBS specimen at load 3532 N (794 lbs) 90% failure load in the 1-2 material plane (Specimen S7).

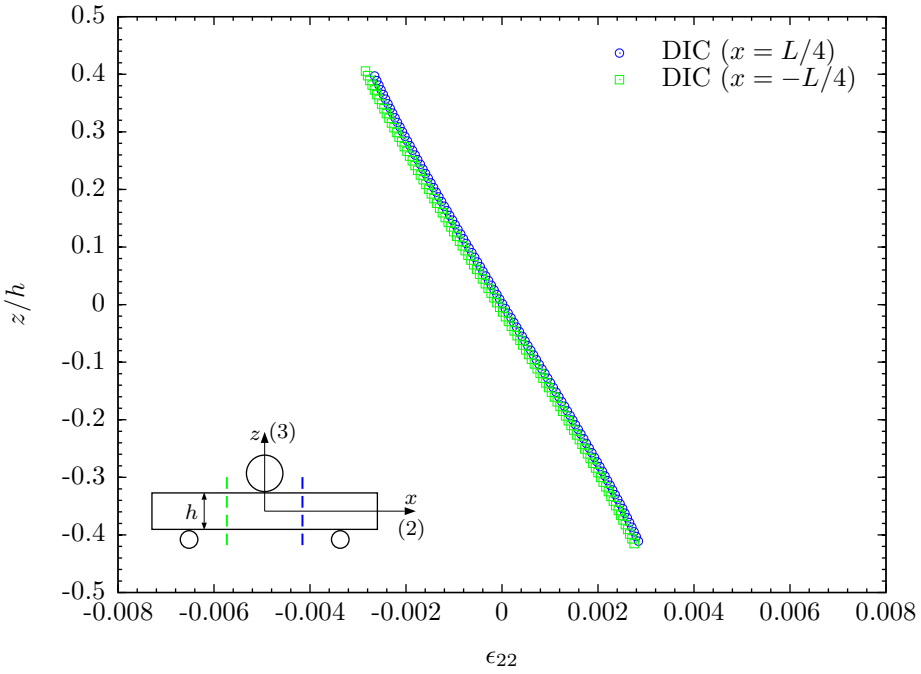

Figure 3.7: Through thickness axial strain distributions for a S2-glass/E773-epoxy tape SBS specimen at load 458 N (103 lbs) 95% failure load in the 2-3 material plane (Specimen S19).

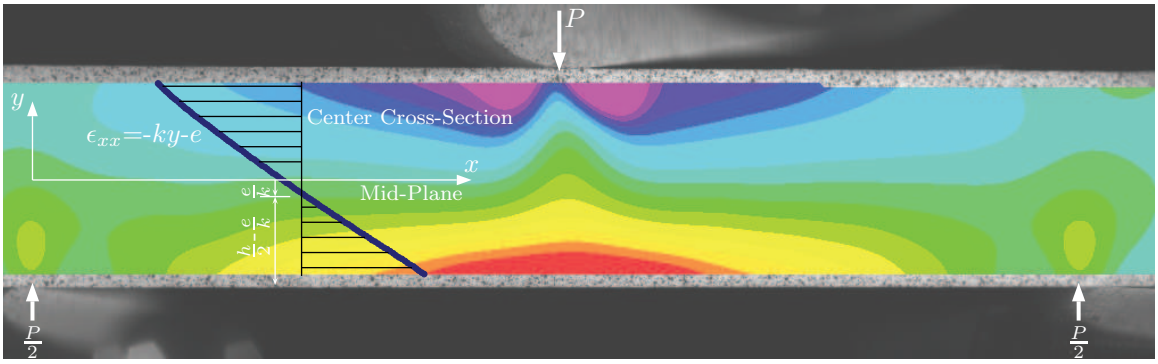

Figure 3.8: Coordinate notation and axial strain distribution.

and

$$M = -\iint\limits_{\substack{-\frac{h}{2}\leqslant y\leqslant\frac{h}{2}\\ -\frac{b}{2}\leqslant z\leqslant\frac{b}{2}}} \sigma_x y\, dydz \tag{3.4}$$

where b is the specimen width. The moment for three-point bending is given by

$$M = \frac{Px}{2} \tag{3.5}$$

where x is axial distance from the closest lower support and P is the applied force. At the cross-sections mid-way between loading nose and supports, i.e., $x = x_c = L/4$, the bending moment is

$$M_c = \frac{PL}{8} \tag{3.6}$$

Substitute equations (3.1) and (3.2) into equations (3.3) and (3.4), neglect the stress variability through the width, integrate and solve equations (3.3) and (3.4) to obtain the following approximations for the tensile and compressive moduli

$$E_{T,C} = \frac{M}{k\frac{bh^3}{12}(1 \mp a)^2}, \quad a = \frac{2}{h}\frac{e}{k} \tag{3.7}$$

As the ratio of the distance e/k between the mid-plane and the neutral plane to the specimen half-thickness is expected to be small such that a^2 is negligible compared to one, equation (3.7) also results in the following expression

$$E_{T,C} = \frac{M(1 \pm a)^2}{k\frac{bh^3}{12}} \tag{3.8}$$

The following maximum shear stress approximation in the SBS specimens away from the support locations is derived using expression (3.8) and force equilibrium in the axial direction on the undeformed beam geometry

$$\sigma_{\mathrm{s}} \approx \frac{3}{4}\frac{P}{A}, \quad A = hb \tag{3.9}$$

The maximum shear stress occurs at the neutral plane $y = -e/k$. It is worth noting that the above equation has the same form as equation (1.1). Indeed, expression (3.9) is a classical (mechanical of materials) approximation for the maximum shear stresses in long beams subject to three-point bending [56]. The closed-form approximation is used to interpret the SBS test data for shear stress in this chapter. The correction for discrepancy of the closed-form approximation is the focus of Chapter 5.

As the tensile and compressive modulus values are material properties independent of the x locations, and the bending moment is a linear function of x, the curvature k and the intercept e are also linear functions of x. The linear axial strain approximation (3.1) for the SBS specimens is generalized as

$$\epsilon_x = -Kxy - Ex, \quad -\frac{h}{2} \leqslant y \leqslant \frac{h}{2} \tag{3.10}$$

where K and E are constants. Equation (3.7) can be rewritten as

$$E_{\mathrm{T,C}} = \frac{M_{\mathrm{c}}}{k_{\mathrm{c}}\frac{bh^3}{12}(1 \mp a)^2}, \quad a = \frac{2}{h}\frac{e_{\mathrm{c}}}{k_{\mathrm{c}}} \tag{3.11}$$

where

$$k_{\mathrm{c}} = Kx_{\mathrm{c}} = \frac{k}{x}x_{\mathrm{c}}, \; e_{\mathrm{c}} = Ex_{\mathrm{c}} = \frac{e}{x}x_{\mathrm{c}} \tag{3.12}$$

The constants k_{c} and e_{c} are measured as the slope and the intercept of the normalized axial strain $\epsilon_x x_{\mathrm{c}}/x$ distributions throughout the SBS specimens away from supports. The measurements in equation (3.11) are not limited to one cross section. Thus, the obtained properties are averages over a number of sections away from support locations.

It is noted that the shear stress distribution reduces to the parabolic distribution if the identical elastic behavior is assumed (i.e., $E_{11\mathrm{T}} = E_{11\mathrm{C}}$). For a beam of rectangular cross-section under three-point bending, we have [56]

$$\sigma_{xy} = \frac{3}{4}\frac{P}{A}\left[1 - \left(\frac{2y}{h}\right)^2\right] \tag{3.13}$$

in the reference coordinate system or

$$\sigma_{xz} = \frac{3}{4}\frac{P}{A}\left[1 - \left(\frac{2z}{h}\right)^2\right] \tag{3.14}$$

in the global coordinate system.

3.3 Experimental Results for S2-Glass Composite Specimens

A total of 15 SBS specimens were machined from a 26-ply 6.1 mm (0.24 inches) thick unidirectional S2-glass/E773-epoxy tape panel [40]. Ten specimens were machined in the fiber (0°) direction and five specimens were machined in the 90° direction. The specimens are 42 mm (1.75 inches) long and 6.4 mm (0.25 inches) wide. The support length L is 30.5 mm (1.2 inches). Five 0° specimens (S1-S5) were loaded in the 1-3 material plane, others (S6-S10) were loaded in the 1-2 plane. The 90° specimens (S11-S15) were loaded in the 2-3 material plane. The specimen dimensions and ultimate failure loads are listed in Tables 3.1, 3.3 and 3.5.

SBS specimens machined in the fiber direction fail in shear. Figure 3.3 shows a typical shear failure which started between the loading nose and a lower support and propagated to the specimen edge. The specimens machined in the 90° direction fail in tension in the middle of the specimen. Figure 3.9 shows a typical tensile failure for a 90° glass/epoxy specimen. As one can see from Tables 3.1, 3.3 and 3.5, the 90° specimens fail at much lower load levels than the specimens loaded in the 1-3 and 1-2 material plane. Therefore, significant nonlinear shear stress-strain response was not observed in the 90° SBS tests.

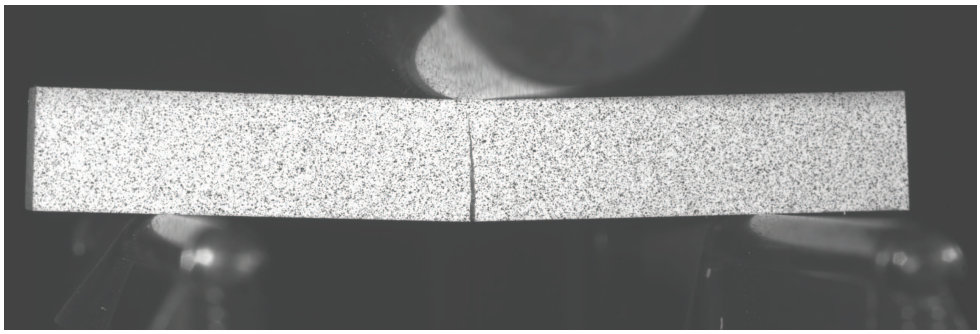

Figure 3.9: Tensile failure of a 90° S2-glass/E773-epoxy tape SBS specimen.

The surface strain components were measured for each specimen in the plane of loading using the DIC technique. The strain contour plots are obtained based on the analysis of stereo images taken with a 16 megapixel camera system. A subset size of 45×45 pixels was chosen, corresponding to approximately 0.67 mm^2 for this particular test. Data was obtained on 9 pixel centers, resulting in approximately 11,000 data points per load case. Figures 3.10, 3.12 and 3.14 illustrate typical axial, transverse and shear surface strain distributions in the 1-2, 1-3 and 2-3 material planes, respectively.

Two-mm long gage sections, mid-way between the lower supports and the upper support locations, were used in the assessment of the tensile, compressive, and shear stress-strain material behavior. Consistent linear through the thickness axial strain distributions were observed for all specimens up to about 95% failure loads. Typical results are shown in Figures 3.5, 3.6 and 3.7 for the 1-2, 1-3 and 2-3 material planes, respectively.

Figures 3.11 and 3.13 show the shear stress-strain response in the 1-3 and 1-2 material plane, respectively, for the 0° SBS specimens. Shear strain in Figures 3.11 and 3.13 is the average maximum shear strain in the two-mm long gage section. The shear stress approximation is based on equation (3.9). The Ramberg-Osgood equation (2.3) was used to generalize the experimental results for each specimen using a least squares approximation. Tables 3.2 and 3.4 list the specimen values for linear

shear modulus G_{ij}, secant-intercept modulus K_{ij}, and exponent n_{ij} in equation (2.3). Sample averages (AVG) and coefficients of variation (COV) are also documented. The trend lines shown in Figures 3.11 and 3.13 are based on the AVG constants. For shear strains γ_{13} and γ_{12} exceeding 1%, the SBS specimens exhibit highly nonlinear shear stress-strain behavior. Tensile failure of the 90° SBS specimens loaded in the 2-3 material plane occurred at shear strain values between 2,000 and 3,000 $\mu\epsilon$. A linear 2-3 plane shear stress-strain response was observed. Table 3.6 lists the 2-3 plane shear modulus values.

It is worth noting that G_{23} value obtained from specimens loaded in the 2-3 material plane is close to a transverse isotropic approximation

$$G_{23} \approx \frac{E_{22}}{2(1+\nu_{23})} = 4.443\,\text{GPa}\,(0.644\,\text{msi}). \tag{3.15}$$

Tables 3.2, 3.4, and 3.6 also list average modulus E_{11}, E_{22}, compressive modulus E_{11C}, E_{22C}, and Poisson's ratio ν_{13}, ν_{23} values. The data reduction procedure described in the previous section was applied to obtained the material properties. It is noted that the Poisson's ratio approximations are based on the axial and transverse strain closest to the tensile (bottom) surface in the center cross-sections between the lower and upper support locations. The Poisson's ratios are calculated as the negative ratios of the slopes of the applied force - axial and transverse strains. The measured applied force - axial and transverse strain relations were linear till failure. It is noted that similar results were obtained in the gage sections in both halves of the specimens. The values listed in Tables 3.2, 3.4, and 3.6 are the average values of the constitutive parameters measured in the gage sections on both sides of the loading nose.

The measured tensile modulus values for S2-glass/E773-epoxy material are similar to the compressive modulus values in the corresponding directions. Higher difference is expected for carbon/epoxy material systems. SBS experiments were accomplished for IM7-carbon/8552-epoxy tape composite in the 1-3 material plane to verify this statement and the results are documented in the next section.

Table 3.1: S2-glass/E773-epoxy tape specimen dimensions and ultimate failure loads (material plane 1-3).

Specimen	h, mm (in.)	b, mm (in.)	F_{u}, N (lbs)
S1	6.198 (0.2440)	6.299 (0.2480)	3745 (842)
S2	6.083 (0.2395)	6.325 (0.2490)	3572 (803)
S3	6.109 (0.2405)	6.299 (0.2480)	3750 (843)
S4	6.071 (0.2390)	6.299 (0.2480)	3767 (847)
S5	6.058 (0.2385)	6.325 (0.2490)	3630 (816)
AVG	6.104 (0.2403)	6.309 (0.2484)	3693 (830)
COV	0.91%	0.22%	2.35%

Table 3.2: S2-glass/E773-epoxy tape constitutive properties (material plane 1-3).

Specimen	G_{13} GPa (msi)	K_{13} MPa (ksi)	n_{13}	E_{11} GPa (msi)	$E_{11\mathrm{C}}$ GPa (msi)	ν_{13}
S1	4.23 (0.614)	194 (28.1)	0.223	45.7 (6.62)	45.5 (6.60)	0.28
S2	4.11 (0.596)	191 (27.6)	0.219	47.9 (6.94)	47.8 (6.94)	0.26
S3	4.09 (0.594)	192 (27.9)	0.218	46.7 (6.77)	46.2 (6.70)	0.26
S4	4.23 (0.613)	186 (27.0)	0.212	46.8 (6.79)	47.4 (6.88)	0.27
S5	4.15 (0.602)	192 (27.8)	0.222	48.2 (6.99)	46.1 (6.69)	0.27
AVE	4.16 (0.604)	191 (27.7)	0.219	47.0 (6.82)	46.6 (6.76)	0.27
COV	1.56%	1.47%	1.93%	2.16%	2.07%	2.89%

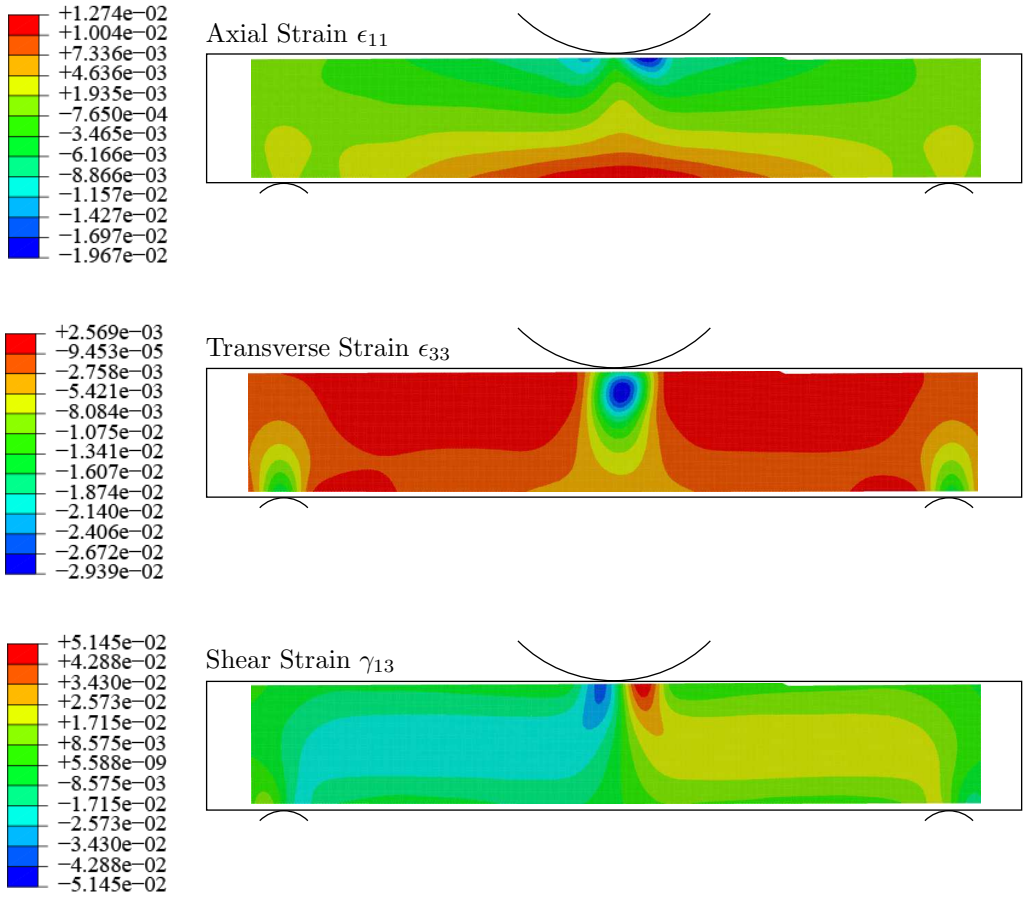

Figure 3.10: Surface strain components for a S2-glass/E773-epoxy tape SBS specimen at 3501 N (787 lbs) 95% failure load in the 1-3 material plane (Specimen S3).

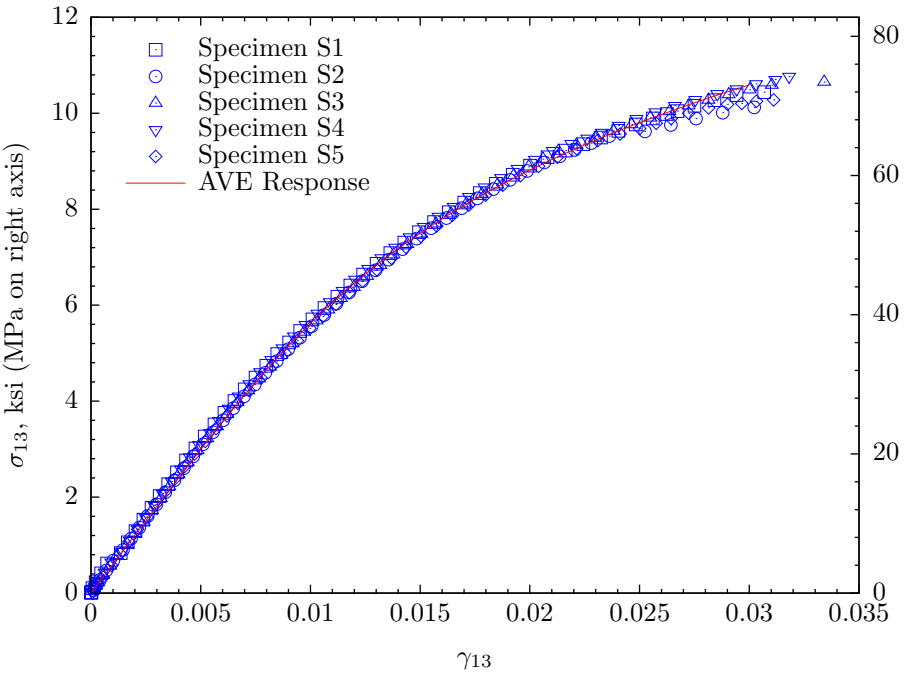

Figure 3.11: Shear stress-strain response for the S2-glass/E773-epoxy tape SBS specimens in the 1-3 material plane.

Table 3.3: S2-glass/E773-epoxy tape specimen dimensions and ultimate failure loads (material plane 1-2).

Specimen	h, mm (in.)	b, mm (in.)	F_{u}, N (lbs)
S6	6.299 (0.2480)	6.096 (0.2400)	3904 (878)
S7	6.287 (0.2475)	6.109 (0.2405)	4029 (906)
S8	6.287 (0.2475)	6.223 (0.2450)	4081 (918)
S9	6.299 (0.2480)	6.083 (0.2395)	3965 (891)
S10	6.350 (0.2500)	6.058 (0.2385)	3951 (888)
AVG	6.304 (0.2482)	6.114 (0.2407)	3986 (896)
COV	0.42%	1.04%	1.75%

Table 3.4: S2-glass/E773-epoxy tape constitutive properties (material plane 1-2).

Specimen	G_{12} GPa (msi)	K_{12} MPa (ksi)	n_{12}	E_{11} GPa (msi)	$E_{11\mathrm{C}}$ GPa (msi)	ν_{12}
S6	4.07 (0.590)	204 (29.6)	0.230	48.1 (6.98)	47.1 (6.84)	0.28
S7	4.36 (0.633)	218 (31.6)	0.247	47.8 (6.93)	47.6 (6.91)	0.28
S8	4.14 (0.600)	216 (31.3)	0.239	47.6 (6.90)	46.2 (6.70)	0.29
S9	4.33 (0.629)	223 (32.3)	0.250	48.2 (6.99)	47.2 (6.84)	0.30
S10	4.35 (0.631)	196 (28.5)	0.221	47.8 (6.94)	46.1 (6.68)	0.28
AVE	4.25 (0.617)	211 (30.7)	0.237	49.1 (6.95)	47.9 (6.79)	0.29
COV	3.22%	5.13%	5.01%	0.56%	1.43%	3.09%

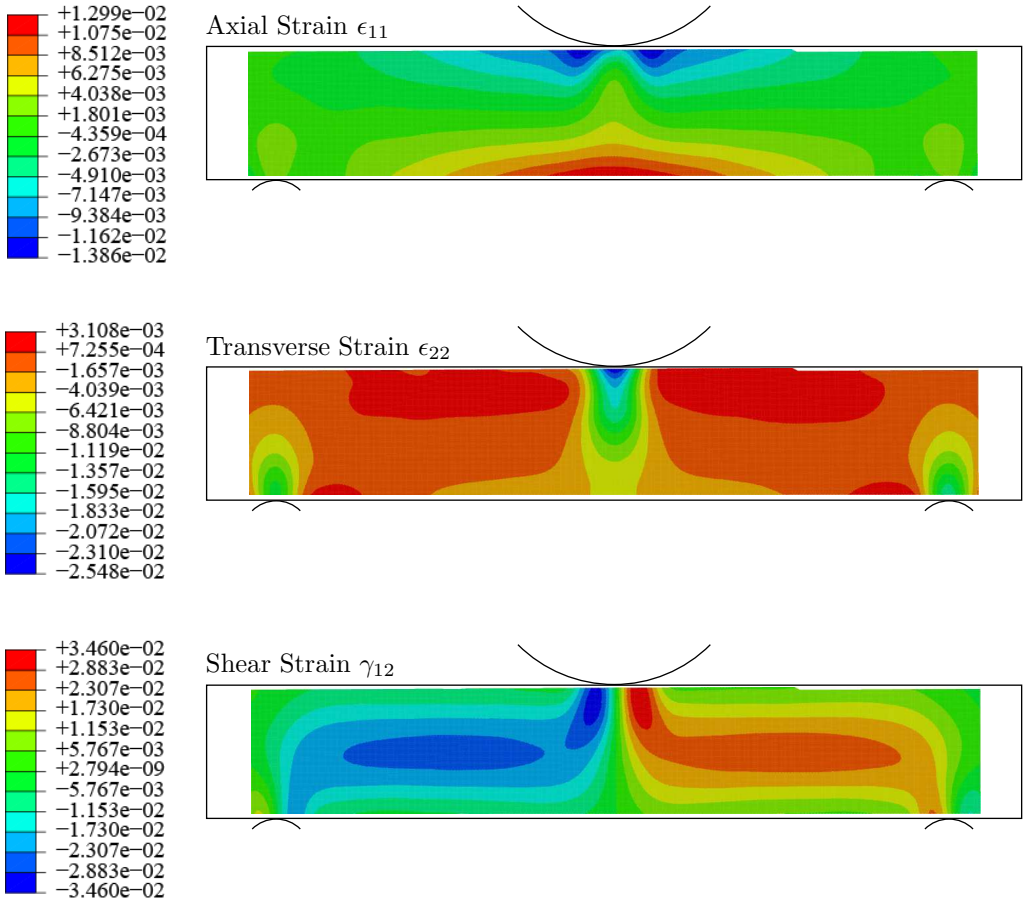

Figure 3.12: Surface strain components for a S2-glass/E773-epoxy tape SBS specimen at 3532 N (794 lbs) 95% failure load in the 1-2 material plane (Specimen S7).

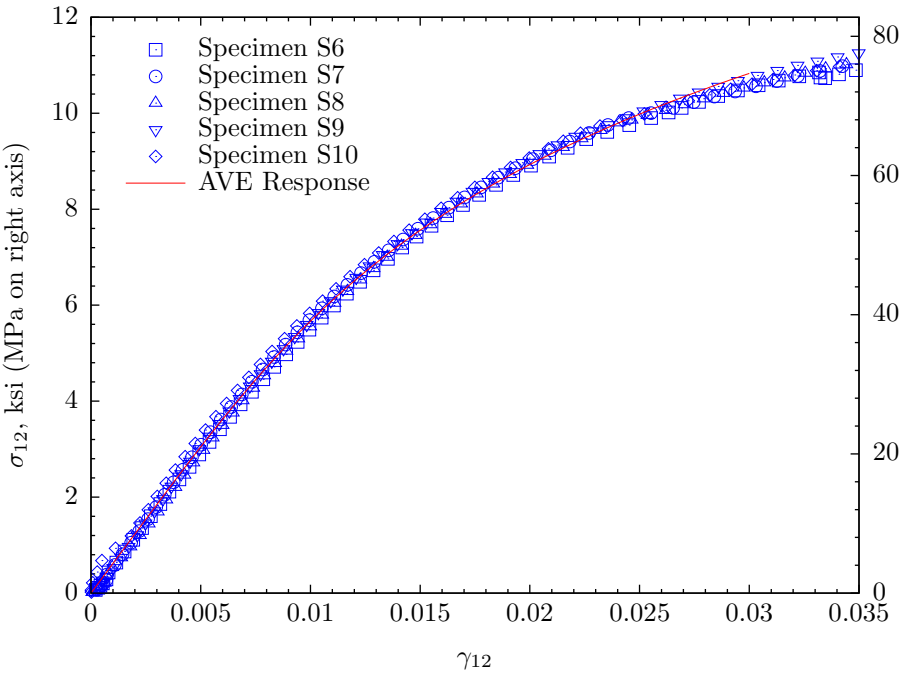

Figure 3.13: Shear stress-strain response for the S2-glass/E773-epoxy tape SBS specimens in the 1-2 material plane.

Table 3.5: S2-glass/E773-epoxy tape specimen dimensions and ultimate failure loads (material plane 2-3).

Specimen	h, mm (in.)	b, mm (in.)	F_{u}, N (lbs)
S11	6.096 (0.2400)	6.287 (0.2475)	497 (112)
S12	6.096 (0.2400)	6.287 (0.2475)	533 (120)
S13	6.096 (0.2400)	6.287 (0.2475)	451 (101)
S14	6.096 (0.2400)	6.299 (0.2480)	457 (103)
S15	6.096 (0.2400)	6.299 (0.2480)	547 (123)
AVG	6.096 (0.2400)	6.292 (0.2477)	497 (112)
COV	0.00%	0.11%	8.76%

Table 3.6: S2-glass/E773-epoxy tape constitutive properties (material plane 2-3).

Specimen	G_{23} GPa (msi)	E_{22} GPa (msi)	$E_{22\mathrm{C}}$ GPa (msi)	ν_{23}
S11	4.47 (0.648)	12.6 (1.83)	12.3 (1.79)	0.42
S12	4.54 (0.658)	12.6 (1.82)	12.6 (1.83)	0.40
S13	4.52 (0.655)	12.6 (1.83)	12.2 (1.77)	0.42
S14	4.43 (0.643)	12.7 (1.84)	12.4 (1.79)	0.41
S15	4.41 (0.640)	12.3 (1.78)	12.2 (1.77)	0.40
AVE	4.47 (0.649)	12.8 (1.82)	12.5 (1.79)	0.41
COV	1.20%	1.29%	1.39%	2.56%

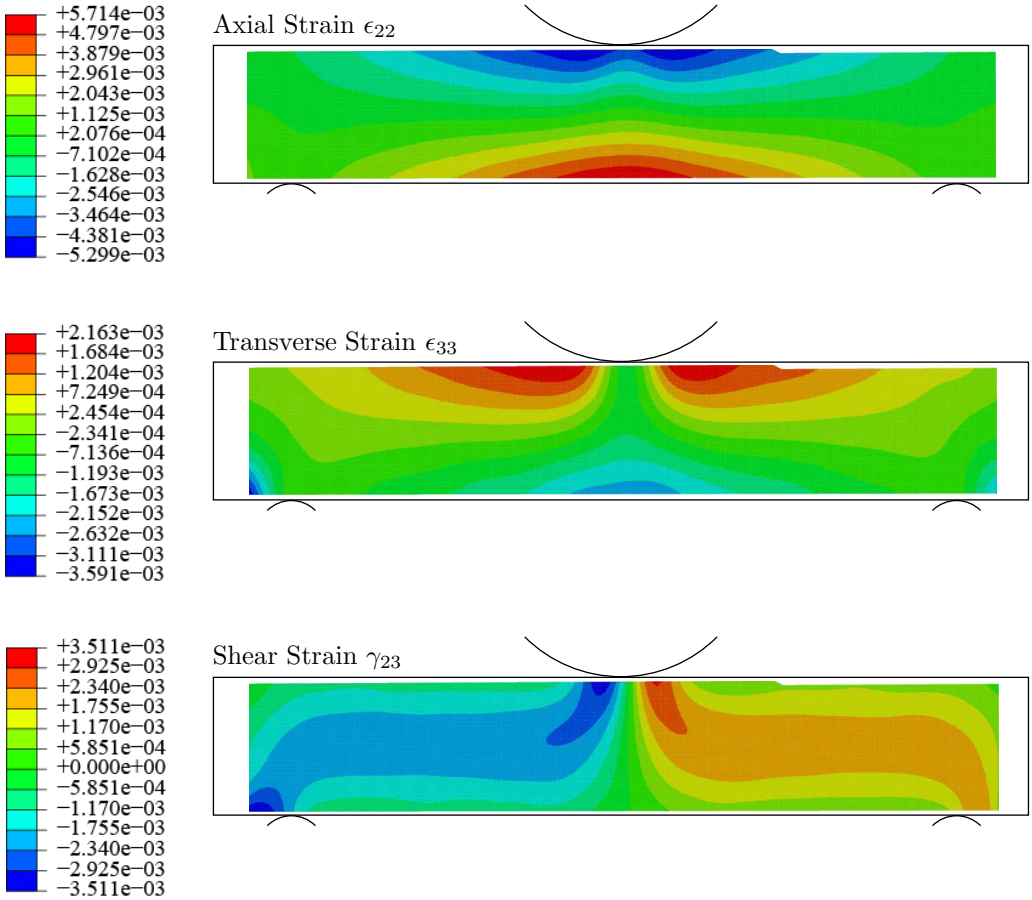

Figure 3.14: Surface strain components for a 90° S2-glass/E773-epoxy tape SBS specimen at 458 N (103 lbs) 95% failure load in the 2-3 material plane (Specimen S14).

3.4 Experimental Results for Carbon Composite Specimens

Five 20-ply unidirectional IM7-carbon/8552-epoxy tape SBS specimens S16 through S20 were manufactured and loaded in the 1-3 material plane to failure [40]. The specimens are 26.7 mm long (1.05 inches), 3.8 mm thick (0.15 inches), and 3.05 mm wide (0.12 inches). Support length is 19.1 mm (0.75 inches). Table 3.7 lists the specimen dimensions and ultimate failure loads. Table 3.8 lists the nonlinear shear properties as well as the average and compressive modulus values.

It is noted that carbon/epoxy SBS specimens have lower thickness compared to the glass/epoxy SBS specimens. A subset size of 21×21 pixels ($0.25\ \text{mm}^2$) was chosen. Data was obtained on 4 pixel centers, resulting in approximately 11,000 data points per load case. Figures 3.15 shows typical axial, transverse, and shear surface strain distributions on beam surface. Figure 3.16 shows the shear stress-strain response measured from gage sections. Highly nonlinear shear response is evident. The trend line shown in Figure 3.16 is based on the average constants listed in Table 3.8.

The axial modulus data listed in Table 3.8 agree with the tensile and compressive modulus values, $E_{11} = 164\,\text{GPa}\,(23.8\,\text{msi})$ and $E_{11\text{C}} = 150\,\text{GPa}\,(21.7\,\text{msi})$, generated using ASTM standard methods for measurement of the unidirectional tensile and compressive constitutive properties and published by the prepreg manufacturer [2].

Five 90° specimens S21 through S25 were loaded in the 2-3 material plane to failure. The specimen dimensions, failure loads and shear moduli are listed in Table 3.9. Similar to Specimens S11 to S15 in the S2-glass case, these 90° specimens failed early at small strain regime. Thus only linear shear stiffnesses were measured.

Table 3.7: IM7-carbon/8552-epoxy tape specimen dimensions and ultimate failure loads (material plane 1-3).

Specimen	h, mm (in.)	b, mm (in.)	F_{u}, N (lbs)
S16	3.848 (0.1515)	3.086 (0.1215)	1605 (361)
S17	3.823 (0.1505)	3.086 (0.1215)	1610 (362)
S18	3.886 (0.1530)	3.099 (0.1220)	1679 (378)
S19	4.001 (0.1575)	3.112 (0.1225)	1703 (383)
S20	3.797 (0.1495)	3.086 (0.1215)	1671 (376)
AVG	3.871 (0.1524)	3.094 (0.1218)	1653 (372)
COV	2.05%	0.37%	2.64%

Table 3.8: IM7-carbon/8552-epoxy tape constitutive properties (material plane 1-3).

Specimen	G_{13} GPa (msi)	K_{13} MPa (ksi)	n_{13}	E_{11} GPa (msi)	$E_{11\mathrm{C}}$ GPa (msi)
S16	5.34 (0.774)	250 (36.2)	0.205	162.3 (23.54)	146.0 (21.17)
S17	5.34 (0.774)	233 (33.8)	0.191	166.2 (24.11)	152.1 (22.06)
S18	5.51 (0.799)	260 (37.7)	0.215	168.1 (24.39)	156.9 (22.75)
S19	5.41 (0.785)	289 (42.0)	0.236	161.5 (23.45)	144.9 (21.02)
S20	5.47 (0.794)	258 (37.5)	0.212	157.4 (22.83)	141.2 (20.48)
AVE	5.41 (0.785)	258 (37.4)	0.212	163.1 (23.66)	148.2 (21.50)
COV	1.44%	7.94%	7.70%	1.39%	4.20%

Table 3.9: IM7-carbon/8552-epoxy tape specimen dimensions, ultimate failure loads and constitutive properties (material plane 2-3).

Specimen	b, mm (in.)		h, mm (in.)		G_{23}, GPa (msi)		F_{u}, N (lbs)	
S21	3.708	(0.1460)	4.623	(0.1820)	3.05	(0.442)	401	(90)
S22	3.670	(0.1445)	4.750	(0.1870)	3.01	(0.437)	473	(106)
S23	3.645	(0.1435)	4.648	(0.1830)	3.14	(0.456)	536	(121)
S24	3.708	(0.1460)	4.763	(0.1875)	3.19	(0.463)	479	(108)
S25	3.670	(0.1445)	4.572	(0.1800)	3.03	(0.440)	392	(88)
AVG	3.680	(0.1449)	4.671	(0.1839)	3.09	(0.447)	456	(103)
COV	0.75%		1.77%		2.50%		13.14%	

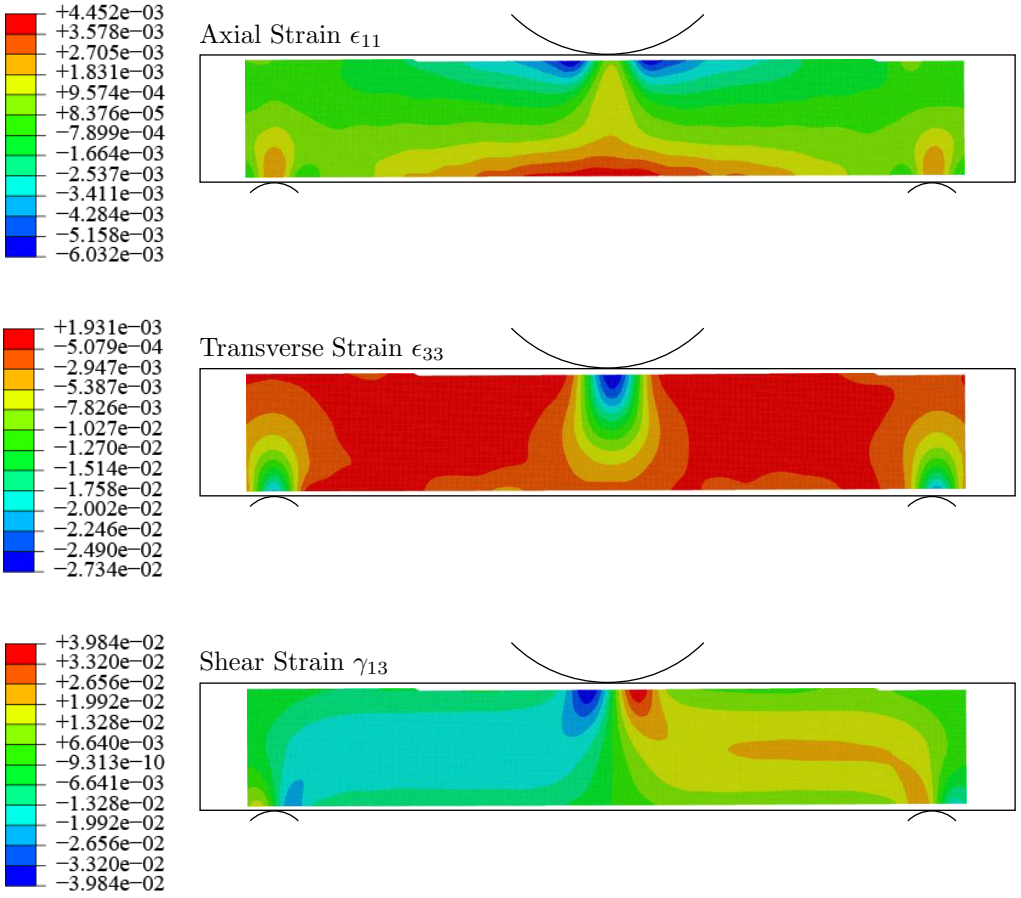

Figure 3.15: Surface strain components for an IM7-carbon/8552-epoxy tape SBS specimen at 1312 N (295 lbs) 82% failure load in the 1-3 material plane (Specimen S16).

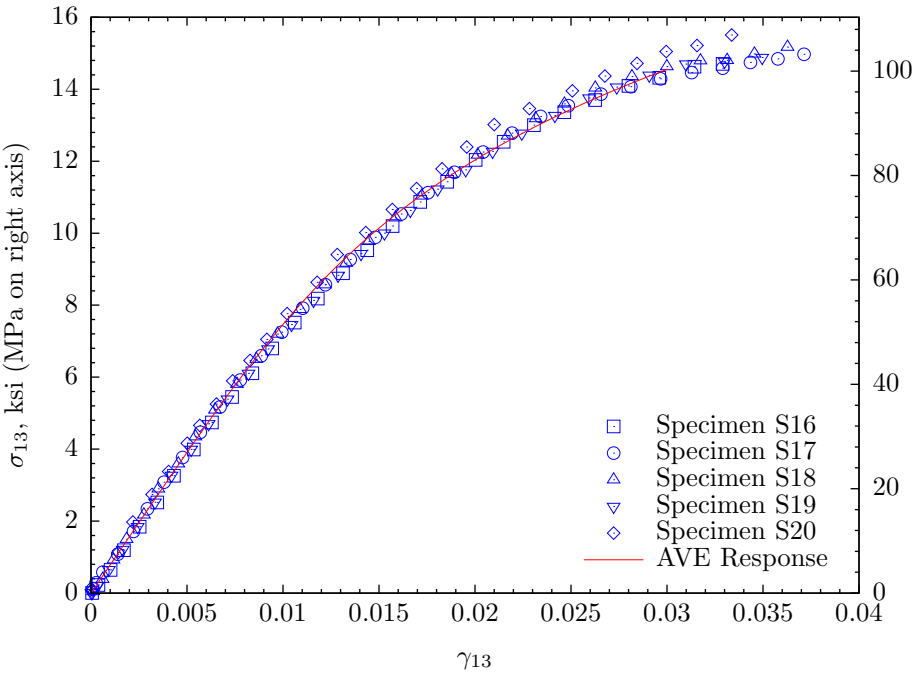

Figure 3.16: Shear stress-strain response for the IM7-carbon/8552-epoxy tape SBS specimens in the 1-3 material plane.

3.5 Experimental Results for E-Glass Composite Specimens

Five 30-ply E-glass/5216-epoxy unidirectional tape SBS specimens (S26-S30) [40] were manufactured and statically loaded (with 0.05 in./min head displacement rate) in the transverse (1-3) material direction to failure following ASTM Standard D 2344 guidelines [11]. The specimens are 38 mm (1.5 inches) long, 6 mm (0.24 inches) thick, and 4.4 mm (0.17 inches) wide. Support length is 25.4 mm (1 inches). Table 3.10 lists specimen dimensions and ultimate failure loads.

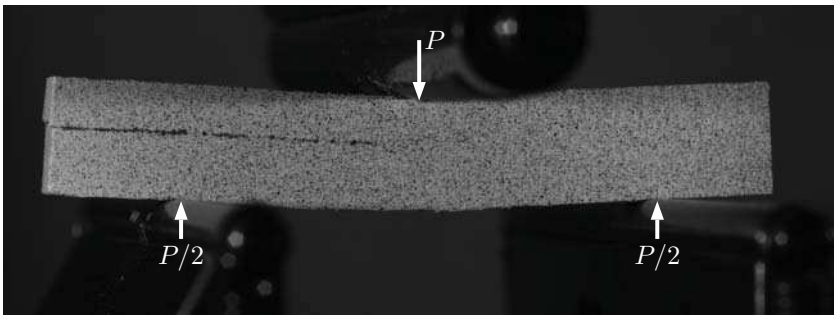

Figure 3.17: Loading conditions and ultimate shear failure of a unidirectional E-Glass/5216-epoxy tape SBS test specimen.

Figure 3.17 shows specimen failure. Loading conditions are also shown. The failure mode is a shear delamination starting between the upper support and a lower support and propagating to the edge. Figure 3.18 shows the five specimens tested. All specimens exhibited similar behavior.

Figure 3.19 illustrates the axial, transverse, and shear strain tensor components for one of the specimens (Specimen S28) at 2153 N (484 lbs), i.e., 92% ultimate failure load. The strain contour plots are obtained based on the analysis of stereo images taken with a 16 megapixel camera system. For the case shown, a subset size of 21×21 pixels was chosen, corresponding to approximately $0.25\,\mathrm{mm}^2$ for this particular test. Data was obtained on 4 pixel centers, resulting in approximately 20,000 data points per load case.

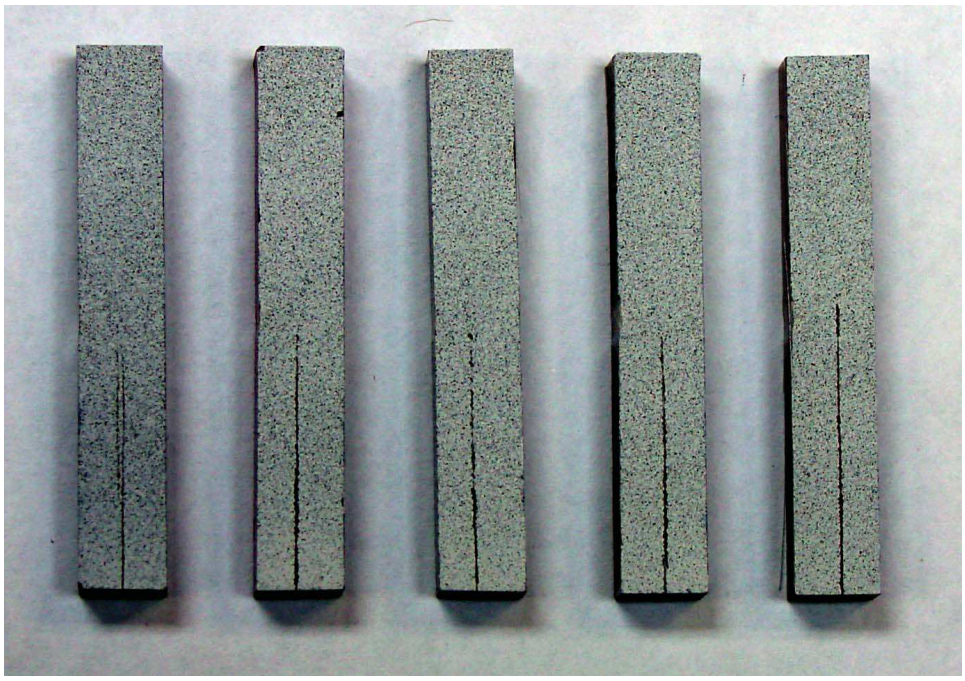

Figure 3.18: Failure mode for five E-glass/5216-epoxy SBS test specimens.

Figure 3.20 shows the interlaminar shear stress-strain response for the five SBS specimens tested (Specimens S26-S30). Table 3.11 lists the values for the interlaminar shear strength S_{13} corresponding to the ultimate failure load, and linear modulus G_{13}, secant-intercept modulus K_{13}, and exponent n_{13} in the Ramberg-Osgood equation (2.3). The trend line shown in Figure 3.20 is based on equation (2.3) and Table 3.11 for the average constants. For shear strain γ_{13} exceeding 1%, the E-glass/5216-epoxy tape SBS specimens exhibit highly nonlinear shear stress-strain behavior.

Table 3.10: E-glass/5216-epoxy tape specimen dimensions and ultimate failure loads (material plane 1-3).

Specimen	h, mm (in.)	b, mm (in.)	F_{u}, N (lbs)
S26	5.994 (0.2360)	4.432 (0.1745)	2540 (571)
S27	6.020 (0.2370)	4.394 (0.1730)	2522 (567)
S28	6.007 (0.2365)	4.382 (0.1725)	2353 (529)
S29	6.045 (0.2380)	4.407 (0.1735)	2455 (552)
S30	5.982 (0.2355)	4.407 (0.1735)	2460 (553)
AVG	6.010 (0.2366)	4.404 (0.1734)	2466 (554)
COV	0.41%	0.43%	2.97%

Table 3.11: E-glass/5216-epoxy tape constitutive properties (material plane 1-3).

Specimen	G_{13}, GPa (msi)	K_{13}, MPa (ksi)	n_{13}
S26	4.51 (0.654)	128 (18.6)	0.147
S27	4.16 (0.603)	128 (18.6)	0.147
S28	4.10 (0.595)	130 (18.8)	0.152
S29	4.04 (0.585)	137 (19.9)	0.168
S30	4.29 (0.622)	124 (18.0)	0.142
AVE	4.22 (0.612)	130 (18.8)	0.151
COV	4.43%	3.74%	6.59%

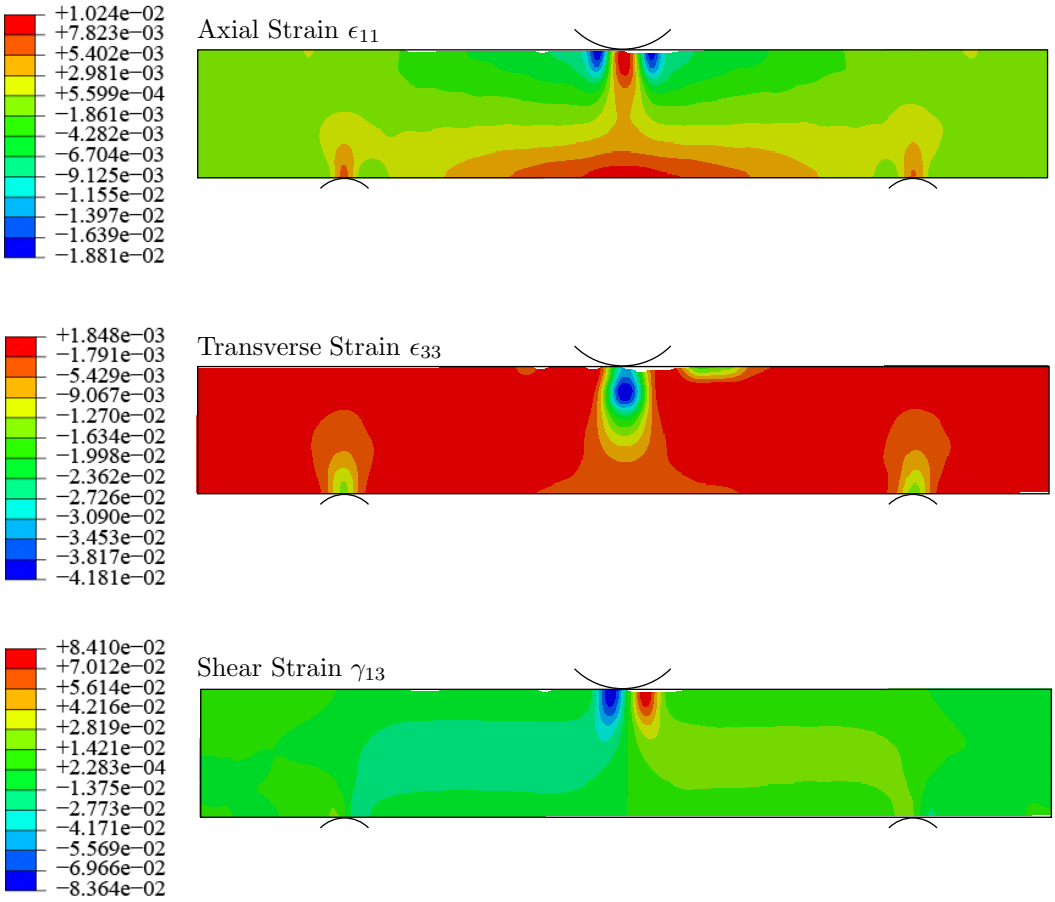

Figure 3.19: Surface strain components for an E-glass/5216-epoxy tape SBS specimen at 2153 N (484 lbs) 92% failure load in the 1-3 material plane (Specimen S28).

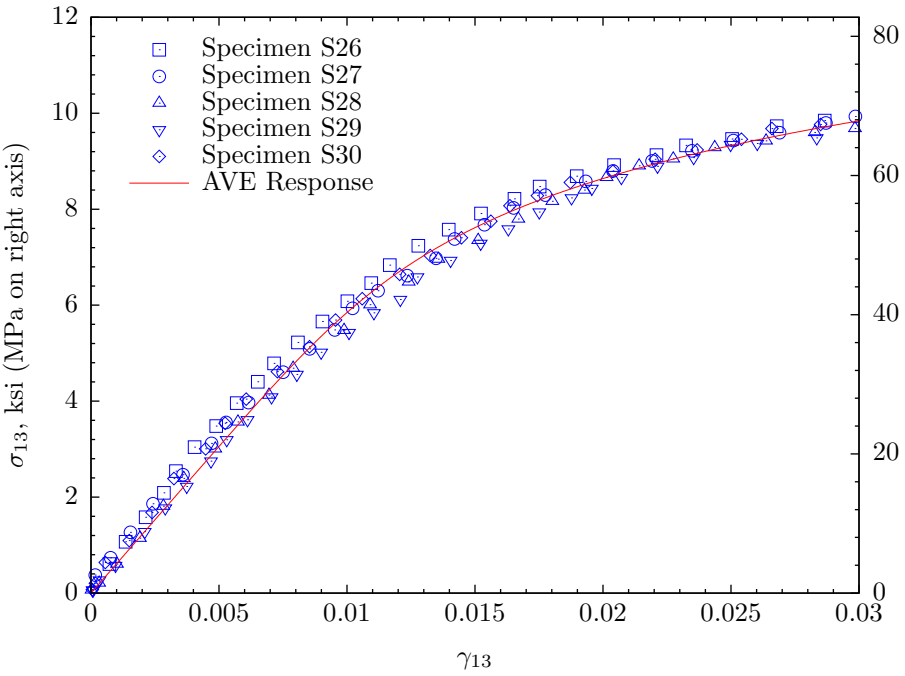

Figure 3.20: Shear stress-strain response for the E-glass/8552-epoxy tape SBS specimens in the 1-3 material plane.

CHAPTER IV

VERIFICATION TESTS

4.1 Unidirectional Tensile Tests

To verify the normal stress-strain response for the unidirectional tape composites used in this work is linear until failure, unidirectional tensile tests were performed for the 0° and 90° specimens [40].

A total of 20 unidirectional E-glass/5216-epoxy tape tensile specimens were machined from a 19 mm (0.75 inches) thick $[0°]_{90}$ E-glass/5216-epoxy panel. Figure 4.1 shows the panel and material directions. This panel was also utilized to manufacture the unidirectional V-notched specimens considered in the next section. X-ray detectable glass tracer fibers are present in the panel to follow material specifications for structural applications. Figure 4.1 shows the location of tracer fibers as red and black lines.

The unidirectional tensile test specimens are 305 mm (12 inches) long and 2.54 mm (0.1 inches) thick. The static tensile tests were accomplished following ASTM Standard D 3039 [9] guidelines. Figure 4.2 shows the linear stress-strain response. The tensile strength corresponds to a 2% axial strain exceeding the axial strain level in the SBS tests. The tensile modulus (E_{11}), Poisson's ratio (ν_{13}), and tensile strength (S_{11}) properties were also obtained from the tensile test and listed in Table 4.1.

To verify accuracy of the DIC technique, conventional strain gage measurements were compared with full-field strain measurements used in the tensile tests. DIC measurements (averaged to the strain gage scale) and strain gage measurements are in excellent agreement: a 0.3% difference for the tensile modulus and a 1% difference for Poisson's ratio are documented.

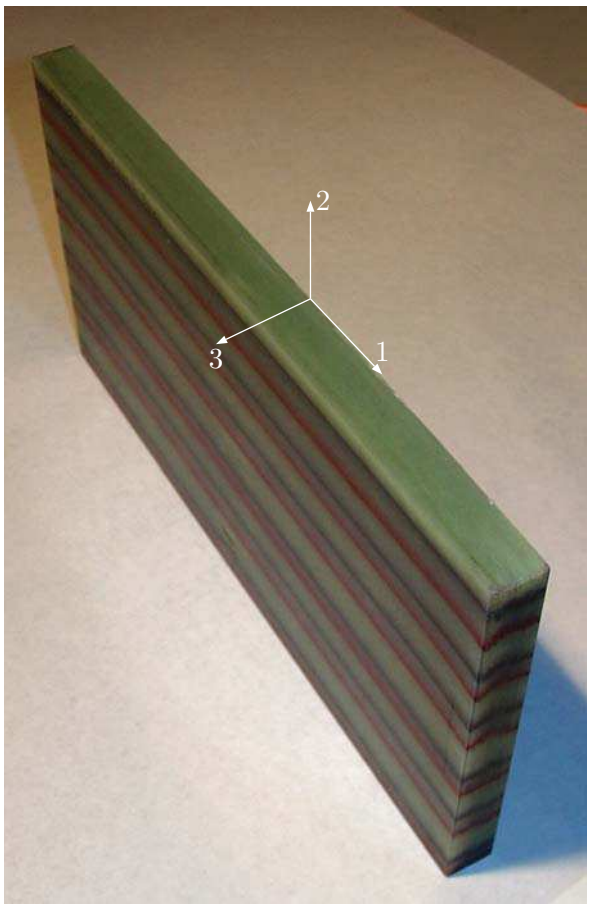

Figure 4.1: $[0°]_{90}$ E-glass/5216-epoxy panel and material directions.

To obtain the transverse normal stress-strain response for the unidirectional E-glass/5216-epoxy tape, a total of 20 $[90°]_{12}$ 19 mm (0.75 inches) wide, 2.54 mm (0.1 inches) thick, and 203 mm (8 inches) long tensile specimens were tested following ASTM Standard D 3039 [9] guidelines. All specimens failed at tracer fibers next to tab locations, resulting in a low average value and high scatter for the material strength in the 90° direction. Test data for 90° modulus and strength are listed in Table 4.2. The stress-strain response for all $[90°]_{12}$ was linear until failure.

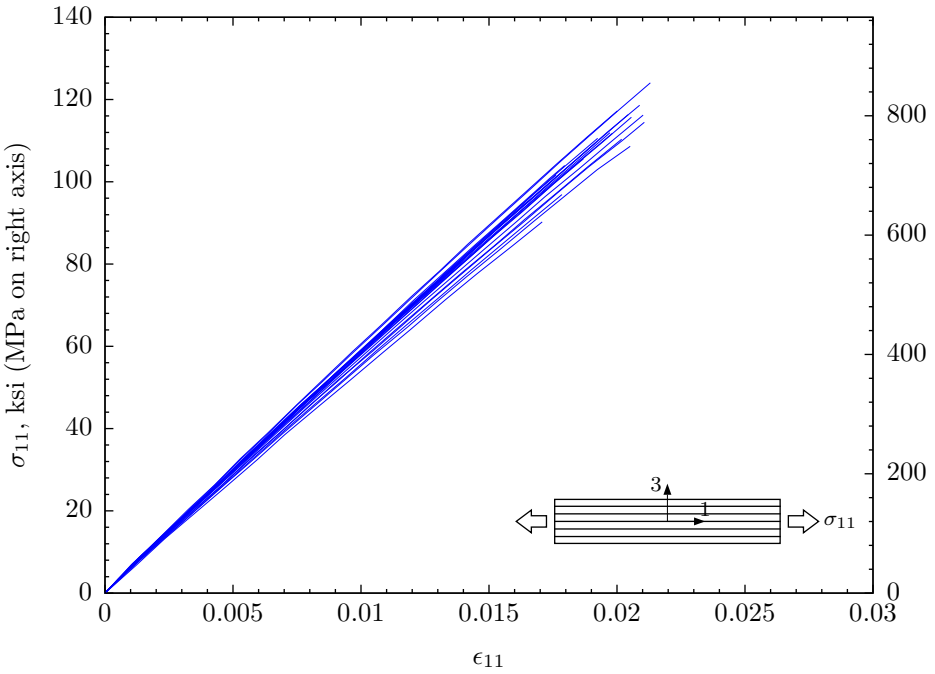

Figure 4.2: Tensile (1-3 material plane) stress-strain response for the $[0^\circ]_{90}$ E-glass/5216-epoxy unidirectional tape specimens.

Table 4.1: Tensile modulus, Poisson's ratio and tensile strength values for $[0°]_{90}$ E-glass/5216-epoxy unidirectional tape.

Specimen	E_{11}, GPa (msi)	ν_{13}	S_{11}, MPa (ksi)	Tracers
B1	41.50 (6.018)	0.3132	843.1 (122.3)	Present
B2	41.90 (6.077)	0.3204	810.3 (117.5)	Not Present
B3	41.55 (6.027)	0.3078	805.4 (116.8)	Present
B4	40.00 (5.801)	0.3153	812.3 (117.8)	Not Present
B5	41.58 (6.031)	0.3119	777.3 (112.7)	Present
B6	41.30 (5.990)	0.3078	800.6 (116.1)	Not Present
B7	39.15 (5.678)	0.3166	768.3 (111.4)	Present
B8	40.75 (5.910)	0.3090	812.6 (117.9)	Present
B9	41.41 (6.005)	0.3127	673.4 (97.7)	Not Present
B10	41.94 (6.082)	0.3041	724.3 (105.1)	Not Present
B11	41.52 (6.022)	0.3119	764.9 (110.9)	Not Present
B12	38.37 (5.565)	0.3294	668.8 (97.0)	Not Present
B13	42.27 (6.131)	0.3073	754.8 (109.5)	Present
B14	39.38 (5.711)	0.3166	696.0 (100.9)	Not Present
B15	41.28 (5.987)	0.3170	805.9 (116.9)	Present
B16	42.41 (6.152)	0.3086	875.9 (127.0)	Present
B17	42.93 (6.227)	0.3019	847.6 (122.9)	Present
B18	41.34 (5.996)	0.3049	834.3 (121.0)	Present
B19	40.23 (5.834)	0.3134	798.1 (115.8)	Not Present
B20	41.13 (5.966)	0.3075	742.3 (107.7)	Not Present
AVG	41.10 (5.961)	0.3119	780.8 (113.2)	
COV	3%	2%	7%	
Specimens with Tracers:				
AVG	41.37 (6.000)	0.3107	808.9 (117.3)	
COV	3%	1%	5%	
Specimens without Tracers:				
AVG	40.83 (5.922)	0.3131	752.7 (109.2)	
COV	3%	2%	8%	

Table 4.2: Tensile modulus and strength values for $[90^\circ]_{12}$ E-glass/5216-epoxy tape.

Specimen	E_{22}, GPa (msi)		ν_{21}	S_{22}, MPa (ksi)	
C1	10.87	(1.577)	0.08896	21.55	(3.126)
C2	10.48	(1.520)	0.08529	27.08	(3.928)
C3	11.23	(1.629)	0.08559	25.91	(3.758)
C4	11.02	(1.598)	0.08474	29.58	(4.290)
C5	11.25	(1.631)	0.08730	17.92	(2.599)
C6	11.67	(1.693)	0.08839	32.35	(4.692)
C7	10.61	(1.538)	0.08408	20.40	(2.958)
C8	10.93	(1.585)	0.08540	22.31	(3.236)
C9	10.43	(1.513)	0.08949	20.11	(2.917)
C10	10.27	(1.489)	0.08616	23.45	(3.401)
C11	10.78	(1.563)	0.08724	18.27	(2.650)
C12	10.98	(1.592)	0.08804	26.24	(3.806)
C13	11.29	(1.637)	0.08743	26.30	(3.814)
C14	11.08	(1.607)	0.08507	17.81	(2.583)
C15	10.85	(1.573)	0.08677	25.39	(3.683)
C16	11.11	(1.611)	0.08766	30.95	(4.489)
C17	10.73	(1.556)	0.08422	29.12	(4.223)
C18	11.28	(1.637)	0.08388	27.11	(3.932)
C19	10.99	(1.594)	0.08714	29.66	(4.302)
C20	10.39	(1.506)	0.08688	27.20	(3.945)
AVG	10.91	(1.582)	0.08649	24.94	(3.617)
COV	3%		2%	18%	

4.2 V-notched Beam Tests

The V-notched beam tests were performed to verify accuracy of the SBS test procedure. References [8] and [57] give a clear description of the experimental setup and loading conditions and parameters for the V-notched beam tests. The test fixture and specimen schematics is shown in Figure 4.3. Analysis of the specimen under load reveals that a state of uniform shear stress exists in the center of the notched specimen on the symmetry section (i.e., the cross-section though the notches), although not in the immediate vicinity of the notch roots [4,8,33]. In addition, the normal stresses are low everywhere on this section. The average shear stress across the notched section of the specimen is calculated using the simple formula [8]:

$$\sigma_{13} = \frac{P}{A}, \qquad A = wt. \tag{4.1}$$

where P is the applied force, and A is the area of the section between the notches.

The interlaminar shear stress-strain data for the unidirectional E-glass/5216-epoxy tape composite are presented in this section. The $[0^\circ]_{90}$ 19 mm (0.75 inches) thick panel shown in Figure 4.1 was used to machine 20 unidirectional V-notched beam specimens following the ASTM Standard [8] requirements. The specimens are in the form of a rectangular flat strip with symmetrically located V-notches.

The DIC tool VIC-3D [1] was used for strain monitoring of the V-notched beam specimens. A line average shear strain through the symmetry section between the V-notch roots is used in the shear stress-strain response approximation. Close-to-uniform shear strain and stress distributions in the symmetry section enable the use of the average values which minimize the noise effects.

The specimens were statically loaded with 1.0 mm/min (0.05 in./min) head displacement rate to failure. Test data for 10 specimens were discarded due to excessive twist deformation. Table 4.3 lists specimen thickness t and width w at the notch root; shear modulus G_{13}; load F_{i} and shear stress $S_{13\mathrm{i}}$ at damage initiation; and ultimate

failure load F_{u} and shear stress $S_{13\mathrm{u}}$. The shear stress-strain response for the 10 specimens are shown in Figure 6.20 (on Page 123) for the comparison with the SBS test results.

The V-notched beam tests were also performed to obtain the nonlinear shear stress-stain responses of the unidirectional IM7-carbon/8552-carbon tape composite in the 1-3 and 2-3 material planes. A total of 12 V-notched beam specimens were tested. The specimen geometry and test data are listed in Table 4.4. The measured shear stress-strain response for the 12 V-notched beam specimens are plotted in Figure 6.16 (on Page 117), again for the comparison purpose. A total of 6 V-notched beam specimens were loaded in the 2-3 material plane to failure. The specimen geometry and test data are listed in Table 4.5. Compared to the specimens loaded in the 1-3 material plane, these 90° specimens failed much earlier at small strain regime. As shown in Figure 4.4, the interlaminar shear stress-strain response is linear up to failure for all specimens.

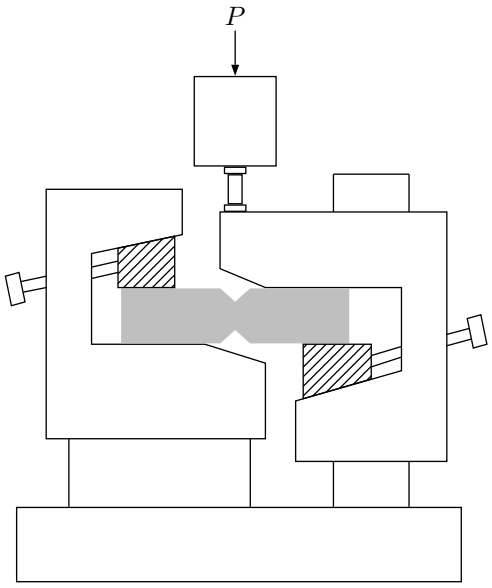

(a)

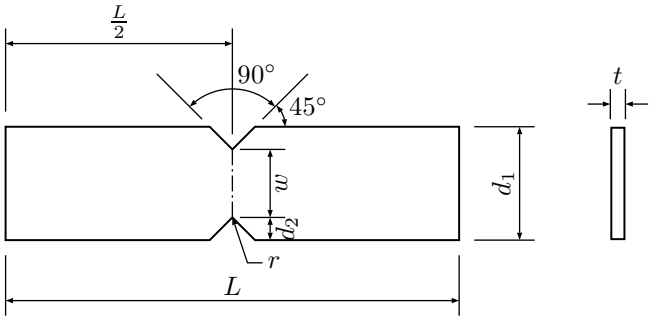

Specimen Dimensions
$d_1 = 20.0\,\text{mm}\ (0.75\,\text{in.})$
$d_2 = 4.0\,\text{mm}\ (0.15\,\text{in.})$
$L = 76.0\,\text{mm}\ (3.0\,\text{in.})$
$r = 1.3\,\text{mm}\ (0.05\,\text{in.})$
$w = 12.0\,\text{mm}\ (0.45\,\text{in.})$

(b)

Figure 4.3: V-notched beam test fixture and specimen schematics.

Table 4.3: Geometry, stiffness and strength test data for the E-glass/5216-epoxy tape V-notched beam specimens.

Specimen	t	w	G_{13}	F_{i}	F_{u}	$S_{13\mathrm{i}}$	$S_{13\mathrm{u}}$
	mm (in.)	mm (in.)	MPa (ksi)	N (lbs)	N (lbs)	MPa (ksi)	MPa (ksi)
V1	2.527	13.20	4613	2273	2500	68.17	74.96
	(0.0995)	(0.5195)	(669.1)	(511)	(562)	(9.887)	(10.87)
V2	2.502	13.09	4689	2126	2411	64.90	73.60
	(0.0985)	(0.5155)	(680.1)	(478)	(542)	(9.413)	(10.67)
V3	2.540	13.14	4312	2286	2469	68.44	73.94
	(0.1)	(0.5175)	(625.3)	(514)	(555)	(9.927)	(10.73)
V4	2.464	13.18	3954	2037	2353	62.75	72.45
	(0.097)	(0.519)	(573.5)	(458)	(529)	(9.102)	(10.51)
V5	2.502	13.13	4087	2224	2491	67.73	75.82
	(0.0985)	(0.517)	(592.8)	(500)	(560)	(9.824)	(11.00)
V6	2.515	13.08	3531	2051	2318	62.29	70.46
	(0.099)	(0.515)	(512.2)	(461)	(521)	(9.034)	(10.22)
V7	2.400	13.08	4137	2042	2344	65.00	74.66
	(0.0945)	(0.515)	(600.0)	(459)	(527)	(9.428)	(10.83)
V8	2.324	13.14	4220	1953	2237	63.98	73.24
	(0.0915)	(0.5175)	(612.1)	(439)	(503)	(9.279)	(10.62)
V9	2.540	12.73	4084	2286	2415	70.77	74.73
	(0.1)	(0.501)	(592.3)	(514)	(543)	(10.264)	(10.84)
V10	2.273	13.11	4477	1859	2202	62.37	73.90
	(0.0895)	(0.516)	(649.3)	(418)	(495)	(9.046)	(10.72)
AVG	2.459	13.09	4210	2114	2374	65.64	73.78
	(0.0968)	(0.5153)	(610.7)	(475)	(534)	(9.520)	(10.70)
COV	3.85%	1.02%	8.06%	7.10%	4.31%	4.51%	2.04%

Table 4.4: Geometry, stiffness and strength test data for the unidirectional IM7-carbon/8552-epoxy tape V-notched beam specimens in the 1-3 material plane.

Specimen	t	w	G_{13}	F_{u}	S_{13}
	mm (in.)	mm (in.)	GPa (msi)	N (lbs)	MPa (ksi)
V11	2.81	11.65	5.10	2896	88.6
	(0.111)	(0.459)	(0.740)	(651)	(12.85)
V12	2.84	11.73	5.08	3211	96.2
	(0.112)	(0.462)	(0.736)	(722)	(13.95)
V13	2.86	11.77	5.08	3038	90.3
	(0.113)	(0.464)	(0.736)	(683)	(13.10)
V14	2.87	11.71	4.66	3194	95.0
	(0.113)	(0.461)	(0.676)	(718)	(13.78)
V15	2.83	11.75	4.96	3105	93.3
	(0.112)	(0.463)	(0.720)	(698)	(13.54)
V16	2.83	11.70	5.21	2873	86.7
	(0.112)	(0.461)	(0.755)	(646)	(12.58)
V17	2.83	11.66	4.95	3131	94.8
	(0.112)	(0.459)	(0.718)	(704)	(13.76)
V18	2.82	11.68	5.01	2967	90.1
	(0.111)	(0.460)	(0.726)	(667)	(13.06)
V19	2.82	11.76	4.91	3216	97.0
	(0.111)	(0.463)	(0.713)	(723)	(14.07)
V20	2.82	11.68	4.96	2758	83.7
	(0.111)	(0.460)	(0.719)	(620)	(12.14)
V21	2.82	11.71	4.91	2709	82.1
	(0.111)	(0.461)	(0.713)	(609)	(11.90)
V22	2.83	11.71	4.92	2704	81.6
	(0.112)	(0.461)	(0.714)	(608)	(11.83)
AVE	2.83	11.71	4.98	2983	90.0
	(0.112)	(0.461)	(0.722)	(671)	(13.05)
COV	0.63%	0.33%	2.71%	6.50%	6.12%

Table 4.5: Geometry, stiffness and strength test data for the unidirectional IM7-carbon/8552-epoxy tape V-notched beam specimens in the 2-3 material plane.

Specimen	t	w	G_{23}	F_{u}	S_{23}
	mm (in.)	mm (in.)	GPa (msi)	N (lbs)	MPa (ksi)
V23	2.82	11.71	2.08	1164	35.3
	(0.111)	(0.461)	(0.425)	(262)	(5.11)
V24	2.82	11.71	2.11	888	26.9
	(0.111)	(0.461)	(0.430)	(200)	(3.90)
V25	2.82	11.71	2.07	1027	31.1
	(0.111)	(0.461)	(0.422)	(231)	(4.51)
V26	2.82	11.71	2.10	1058	32.1
	(0.111)	(0.461)	(0.430)	(238)	(4.65)
V27	2.82	11.71	2.02	998	30.2
	(0.111)	(0.461)	(0.412)	(224)	(4.38)
V28	2.82	11.71	2.03	1036	31.4
	(0.111)	(0.461)	(0.415)	(233)	(4.55)
AVG	2.82	11.71	2.07	1028	31.2
	(0.111)	(0.461)	(0.422)	(231)	(4.52)
COV			1.79%	8.71%	8.71%

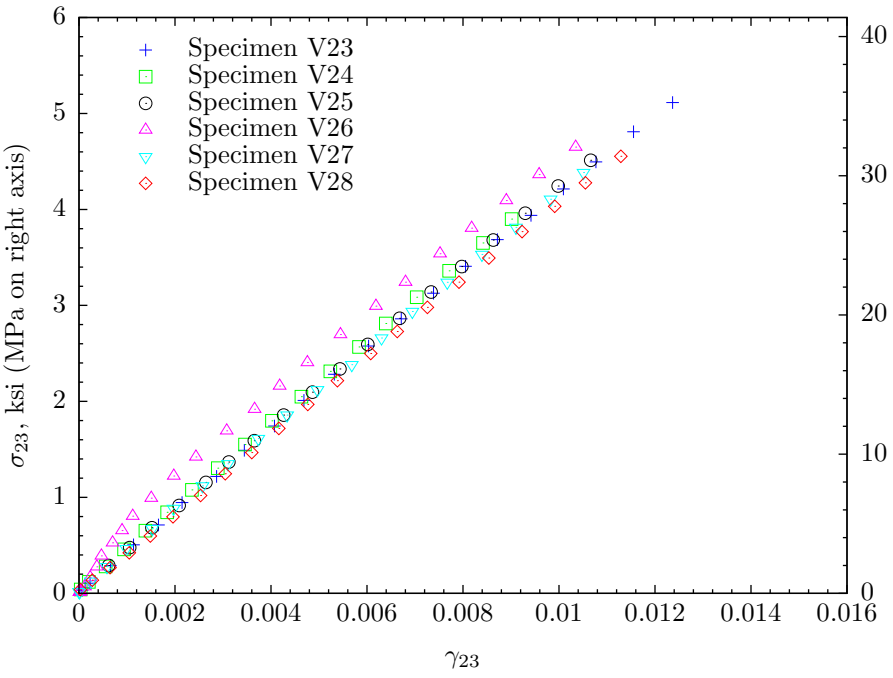

Figure 4.4: Shear stress-strain response for the IM7-carbon/8552-epoxy tape V-notched beam tape specimens in the 2-3 material plane.

4.3 Curved Beam Tests

The curved beam tests [10] were performed to characterize through-the-thickness tensile properties for the unidirectional IM7-carbon/8552-epoxy prepreg tapes. A finite element model was also developed to validate the data reduction procedure.

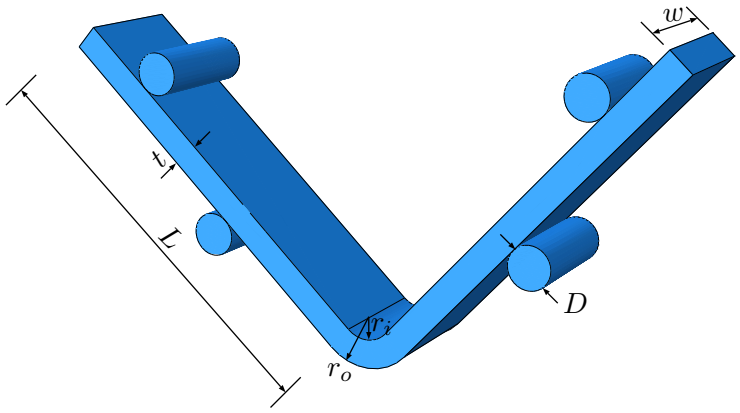

Figure 4.5: Specimen geometry for the 90° curved beam test.

As illustrated in Figures 4.5 and 4.6, the curved beam has uniform thickness and consists of two straight legs connected by a 90° bend with a 6.4 mm (0.25 inches) inner radius [10]. The curved beam is loaded in four-point bending to apply a constant bending moment across the curved test section. The stress state in the curved region is complex. Circumferential tensile stress are produced along the inner surface, and circumferential compressive stresses are produced on the outer surface. The radial tensile stress ranges from zero at the inner and outer surfaces to a peak in the middle third of the thickness. Thus, an out-of-plane tensile stress is produced in the curved region of the specimen to cause the interlaminar tensile failure. The interlaminar tensile strength is defined as the maximum radial stress at failure [10]. Stresses in curved region are usually deduced based on two-dimensional analysis using simple bending theory [32,36], Lekhnitskii's elasticity solution [37], or finite element analysis

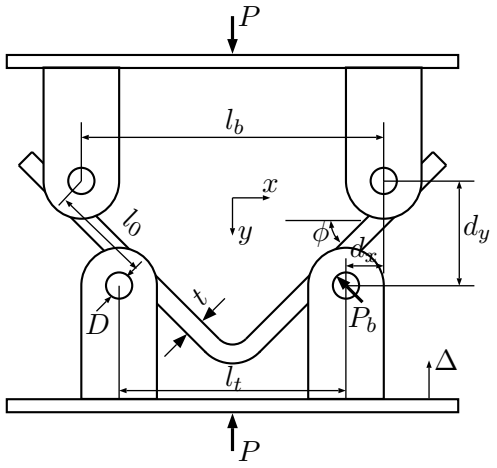

Figure 4.6: Curved beam in four-point bending.

[19, 21, 36, 51, 54]. Three-dimensional finite element models are used to account for the restraint on anticlastic bending due to the curvature [61].

The curved beam test is designed to investigate the interlaminar tensile strength. However, full-field strain measurement techniques enable assessment of through-the-thickness stress-strain relations. By using the radial stress from closed-form solution and radial strain from full-field strain survey (e.g., DIC measurements), through-the-thickness Young's modulus E_3 can be determined.

4.3.1 Closed-Form Stresses

The stress calculation for the curved beam test is given in the ASTM standard [10]. Referring to Figure 4.7, the applied moment M on the curved section of the specimen is the product of the force exerted by one of the cylindrical loading bars, P_b, and the distance, l_0, between two bars along a leg. From the force equilibrium and the geometries of the loading fixture and test specimen, we have

$$P_b = \frac{P}{2\cos(\phi)} \tag{4.2}$$

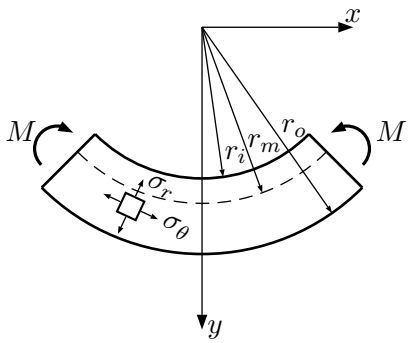

Figure 4.7: Moment on curved test section.

and

$$l_0 = \frac{d_x}{\cos(\phi)} + (D+t)\tan(\phi) \tag{4.3}$$

where ϕ is the angle in degrees of the loading arm from horizontal, d_x is the horizontal distance between the centerlines of two top and bottom adjacent rollers $(l_b - l_t)/2$, D is the diameter of the cylindrical loading bars, and t is the specimen thickness. The curved beam strength (CBS) can be calculated from the total force, P, at the first force drop [10]:

$$CBS = \frac{M}{w} = \frac{P_b l_0}{w} = \left(\frac{P_b}{2w\cos(\phi)}\right)\left(\frac{d_x}{\cos(\phi)} + (D+t)\tan(\phi)\right) \tag{4.4}$$

where w is the width of the specimen.

To calculate ϕ during loading, the vertical displacement, d_y, between the cylindrical loading bars is calculated by subtracting the vertical displacement, Δ, of the loading fixture from the initial value of d_y

$$d_y = (d_y)_i - \Delta = d_x\tan(\phi_i) + \frac{D+t}{\cos(\phi_i)} - \Delta \tag{4.5}$$

where the initial angle ϕ_i is half the overall angle between the loading arms of the specimen prior to test, i.e., $\phi_i = 45^\circ$ for a 90° curved beam specimen. The vertical

displacement, Δ, is obtained from the stoke output of the test stand.

Using trigonometric functions, a value of ϕ can be calculated for a given value of d_y [10]:

$$\phi = \sin^{-1}\left(\frac{-d_x(D+t) + d_y\sqrt{d_x^2 + d_y^2 - D^2 - 2Dt - t^2}}{d_x^2 + d_y^2}\right) \tag{4.6}$$

All other parameters in the above equation remain fixed during loading.

A two-dimensional elasticity solution was developed by Lekhniskii [37] for stresses in a curve beam segment by cylindrical anisotropy. The radial stress σ_r, circumferential stress σ_θ and shear stress $\sigma_{r\theta}$ under pure bending moment M are given by

$$\sigma_r = -\frac{M}{r_o^2\, bg}\left[1 - \frac{1-\rho^{\kappa+1}}{1-\rho^{2\kappa}}\left(\frac{r}{r_o}\right)^{\kappa-1} - \frac{1-\rho^{\kappa-1}}{1-\rho^{2\kappa}}\rho^{\kappa+1}\left(\frac{r_o}{r}\right)^{\kappa+1}\right] \tag{4.7}$$

$$\sigma_\theta = -\frac{M}{r_o^2\, bg}\left[1 - \frac{1-\rho^{\kappa+1}}{1-\rho^{2\kappa}}\kappa\left(\frac{r}{r_o}\right)^{\kappa-1} - \frac{1-\rho^{\kappa-1}}{1-\rho^{2\kappa}}\kappa\rho^{\kappa+1}\left(\frac{r_o}{r}\right)^{\kappa+1}\right] \tag{4.8}$$

$$\sigma_{r\theta} = 0 \tag{4.9}$$

As illustrated in Figure 4.7, r is the radius of the considered location, r_i and r_o are the inner and outer radii of curve segment respectively. The expression for g is given by

$$g = \frac{1-\rho^2}{2} - \frac{\kappa}{\kappa+1}\frac{(1-\rho^{\kappa+1})^2}{1-\rho^{2\kappa}} + \frac{\kappa\rho^2}{\kappa-1}\frac{(1-\rho^{\kappa-1})^2}{1-\rho^{2\kappa}}, \quad \kappa = \sqrt{\frac{E_\theta}{E_r}}, \quad \rho = \frac{r_i}{r_o} \tag{4.10}$$

The moduli in the radial and circumferential directions (E_r and E_θ) may be approximated with the moduli of a flat unidirectional laminate in the 90° and 0° directions respectively.

The maximum radial stress occurs at the radial distance:

$$r_m = \left[\frac{(1-\rho^{\kappa-1})(\kappa+1)(\rho r_o)^{\kappa+1}}{(1-\rho^{\kappa+1})(\kappa-1)r_o^{-(\kappa-1)}}\right]^{\frac{1}{2\kappa}} \tag{4.11}$$

Using the curved beam strength (CBS) calculated from equation (4.4) in equation (4.7), the maximum radial stress can be obtained, i.e.,

$$\sigma_r^{\max} = -\frac{CBS}{r_o^2\, g}\left[1 - \frac{1-\rho^{\kappa+1}}{1-\rho^{2\kappa}}\left(\frac{r_m}{r_o}\right)^{\kappa-1} - \frac{1-\rho^{\kappa-1}}{1-\rho^{2\kappa}}\rho^{\kappa+1}\left(\frac{r_o}{r_m}\right)^{\kappa+1}\right] \tag{4.12}$$

Lekhniskii's elasticity solution results in a very complicated expression for the maximum radial stress $\sigma_r^{\max}$. For a wide range of geometries and materials, a much simpler but accurate expression for $\sigma_r^{\max}$ is given by Kedward et al. [36]:

$$\sigma_r^{\max} = \frac{3 \cdot CBS}{2t\sqrt{r_i r_o}} \tag{4.13}$$

The approximation was developed from the classical (mechanics of materials) beam theory and based on the assumption that maximum radial stress occurs at

$$r_m = \sqrt{r_i r_o} \tag{4.14}$$

The accuracy of this equation decreases as the E_θ/E_r ratio increases or the r_i/r_o ratio (ρ) decreases. For the ASTM suggested geometry, an E_θ/E_r ratio of less than 20 produces an error of less than 2% from the use of equation (4.12) [10].

To verify accuracy of the elasticity solution (4.12) and approximation (4.13) for the maximum radial stress, two-dimensional finite element analysis was performed using the commercial finite element code ABAQUS [24]. A typical mesh of the finite element model is shown in Figure 4.8. Three sources of nonlinearity were considered in the analysis: geometric nonlinearity, material nonlinearity and contact interaction. Geometric nonlinearity was included to account for large deflection. The nonlinear shear stress-strain response was implemented via user material subroutine UMAT as described in Chapter 2. The loading and supporting cylinders were assumed to be rigid and modeled with cylindrical rigid surfaces. The surface-to-surface contact algorithm was implemented to simulate the contact interaction between cylinders and beam specimen. Second-order plane stress elements with reduced integration (i.e., the CPS8R elements in ABAQUS) were used. Owing to symmetry, half of the specimen was modeled. A concentrated load P was assumed to act at the center of the loading cylinder and the center of the supporting cylinder was fixed.

Figure 4.9 shows the radial stress distribution across the thickness of the symmetry section. Excellent agreement between the finite element analysis and the elasticity

solution can be observed. The accuracy of simple calculation (4.13) is also verified. Therefore, equation (4.13) was adopted in the data reduction.

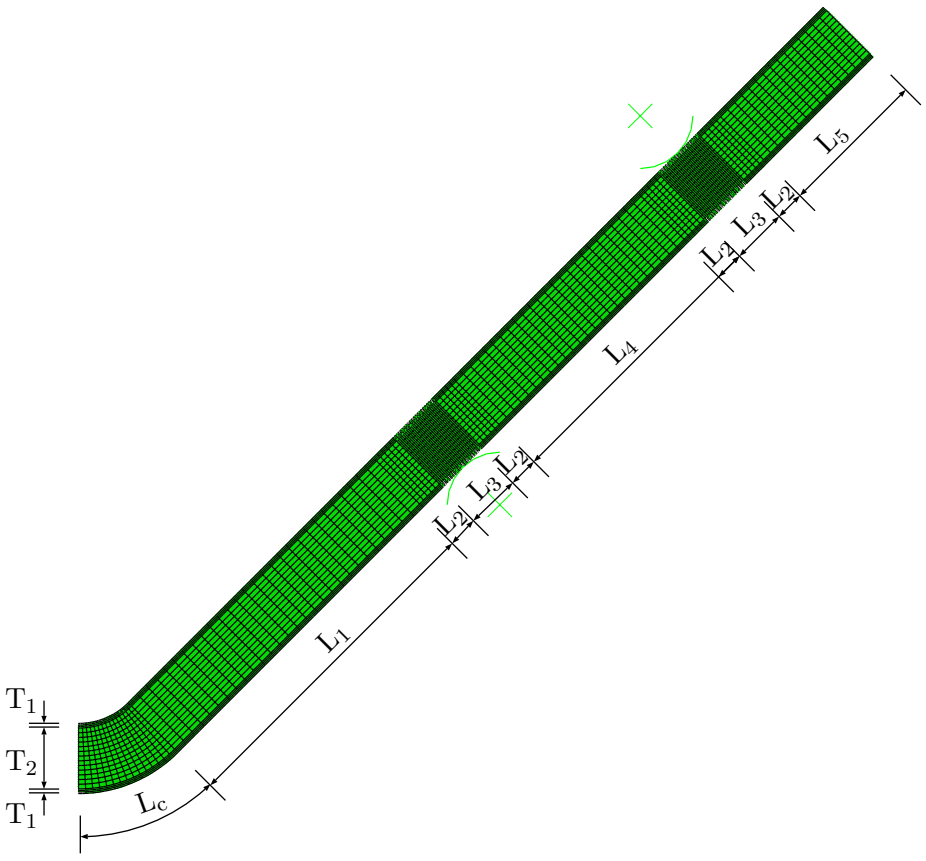

Figure 4.8: A typical finite element mesh of the curved beam specimen.

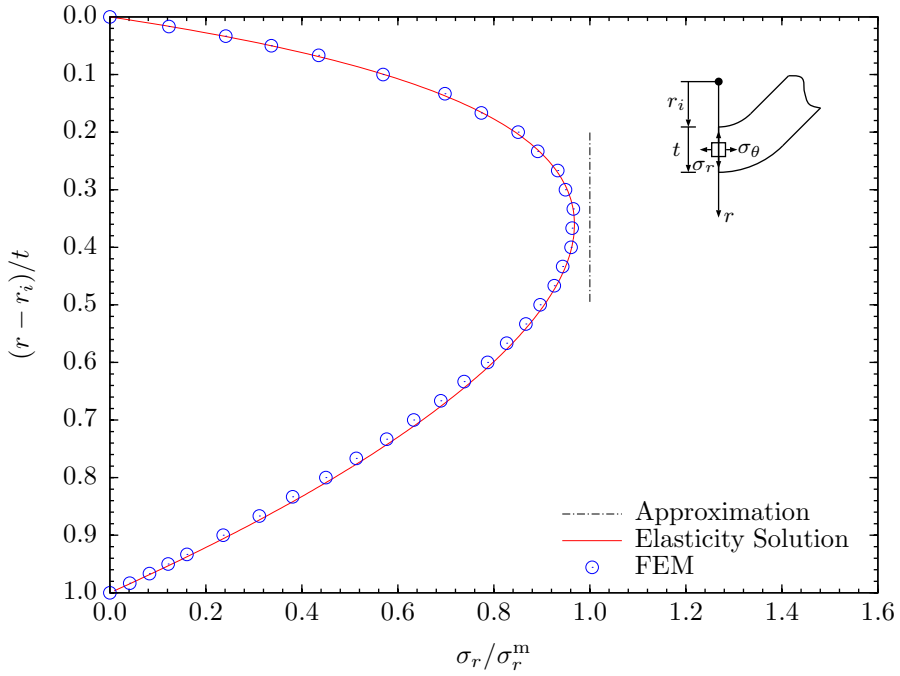

Figure 4.9: Radial stress distribution for a unidirectional IM7-carbon/8552-epoxy curved beam specimen at 3901 N (877 lbs) 95% failure load (Specimen A5).

4.3.2 Experimental Results

A total of 17 curved beam specimens, manufactured to the ASTM standard specifications [10], were statically loaded with a 0.50 mm/min (0.02 in./min) head displacement rate to failure. The curved beam specimens have a loading leg length of 90 mm (3.5 inches). Five specimens have a width of 25.4 mm (1.0 inches) and the rest have a width of 12.7 mm (0.5 inches). The specimen dimensions are listed in Table 4.6 for the half-inch-width specimens and Table 4.7 for the one-inch-width specimens respectively, in which t_{r} is the average thickness of the curved region and t_{s} is the leg thickness.

The DIC technique was used to obtain the full-field strain measurements. Figure 4.10 shows the texture created on the specimen surface using black and white spray paints. The interlaminar stress-strain response was linear till failure. Through-the-thickness Young's modulus E_3 is determined from the initial slope of radial stress-strain response (σ_r-ϵ_r). The obtained values are listed in Tables 4.6 and 4.7 respectively for one-inch-width and half-inch-width specimens. These results are in good agreement with measurements obtained from the 90° SBS specimens machined from the edges of 90° V-notched beam specimens, That is, the SBS specimens were 19.0 mm (0.75 inches) long, 3.81 mm (0.15 inches) thick and 2.79 mm (0.11 inches) wide. The loading plane is the 2-3 material plane that corresponds to the SBS thickness direction. The average E_3 value based on the SBS test is 9.24 MPa (1.34 msi) with a COV less than 5%. The ultimate failure loads F_u and the maximum radial stresses (interlaminar tensile stresses) S_{33} calculated from the approximation (4.13) are also listed in the Tables 4.6 for the one-inch-width specimens.

Figure 4.10: Random texture created using black and while spray paints on IM7-carbon/8552-epoxy curved beam test specimen surface.

Table 4.6: Geometry, stiffness and strength of the unidirectional IM7-carbon/8552-epoxy tape curved beam specimens ($b \approx 1.0$ inches).

Specimen	b	t_{r}	t_{s}	E_3	F_{u}	S_{33}
	mm (in.)	mm (in.)	mm (in.)	GPa (msi)	N (lbs)	MPa (ksi)
A1	25.400	6.998	6.414	9.34	3567	67.6
	(1.000)	(0.2755)	(0.2525)	(1.354)	(802)	(9.81)
A2	25.375	6.871	6.579	9.94	3896	75.0
	(0.999)	(0.2705)	(0.2590)	(1.442)	(876)	(10.87)
A3	25.425	6.896	6.598	9.69	5395	97.4
	(1.001)	(0.2715)	(0.2598)	(1.405)	(1213)	(14.13)
A4	25.451	6.972	6.668	9.04	5204	93.6
	(1.002)	(0.2745)	(0.2625)	(1.311)	(1170)	(13.58)
A5	25.476	6.744	6.661	9.69	3959	77.7
	(1.003)	(0.2655)	(0.2623)	(1.406)	(890)	(11.27)
AVE	25.425	6.896	6.584	9.54	4404	82.3
	(1.001)	(0.2715)	(0.2592)	(1.384)	(990)	(11.93)
COV	0.16%	1.45%	1.56%	3.71%	18.93%	15.47%

Table 4.7: Geometry, stiffness and strength of the unidirectional IM7-carbon/8552-epoxy tape curved beam specimens ($b \approx 0.5$ inches).

Specimen	b mm (in.)	t_{r} mm (in.)	t_{s} mm (in.)	E_3 GPa (msi)
A6	12.700	6.985	6.680	9.34
	(0.5000)	(0.2750)	(0.2630)	(1.354)
A7	12.687	7.112	6.426	9.73
	(0.4995)	(0.2800)	(0.2530)	(1.411)
A8	12.725	7.036	6.464	11.98
	(0.5010)	(0.2770)	(0.2545)	(1.738)
A9	12.687	6.960	6.629	8.75
	(0.4995)	(0.2740)	(0.2610)	(1.269)
A10	12.675	6.998	6.610	9.42
	(0.4990)	(0.2755)	(0.2603)	(1.366)
A11	12.687	7.023	6.674	9.57
	(0.4995)	(0.2765)	(0.2628)	(1.387)
A12	12.687	7.010	6.668	9.11
	(0.4995)	(0.2760)	(0.2625)	(1.322)
A13	12.675	6.985	6.585	9.00
	(0.4990)	(0.2750)	(0.2593)	(1.305)
A14	12.700	7.010	6.629	8.83
	(0.5000)	(0.2760)	(0.2610)	(1.280)
A15	12.675	7.049	6.566	8.00
	(0.4990)	(0.2775)	(0.2585)	(1.161)
A16	12.700	7.010	6.674	8.68
	(0.5000)	(0.2760)	(0.2628)	(1.259)
A17	12.662	6.972	6.579	10.03
	(0.4985)	(0.2745)	(0.2590)	(1.455)
AVE	12.688	7.013	6.599	9.37
	(0.4995)	(0.2761)	(0.2598)	(1.359)
COV	0.13%	0.58%	1.24%	10.51%

CHAPTER V

NUMERICAL PROCEDURE FOR ASSESSMENT OF NONLINEAR SHEAR PROPERTIES

5.1 Discrepancy of the Closed-Form Approximation

In the assessment of nonlinear shear properties presented in Chapter 3, the stress reduction was based on the closed-form approximation (3.9), i.e.,

$$\sigma_s \approx \frac{3}{4}\frac{P}{A} \tag{3.9}$$

Therefore the accuracy of the closed-form approximation is essential in the material characterization.

A number of stress analyses [22,23,52,59,64,66] have been conducted to assess the accuracy of the closed-form approximation. It is worth noting that all the previous studies assume identical elastic behavior in tension and compression. These studies show that the parabolic shear-stress distribution described by the classical (mechanics of materials) beam theory only occurs on planes midway between the loading and support points. Moreover, the maximum shear stress σ_s predicted by equation (3.9) is never fully reached and the effect of nonlinear shear response was found to reduce the maximum shear stress. Also no strain measurements were taken to substantiate such approximation.

Whitney [59] analyzed the stress distribution of short-beam shear and four-point shear (FPS) specimens by using a two-dimensional elasticity solution. Force applied by the cylinders was modelled as a uniform stress distributed over a small length of the beam. Unidirectional AS1-carbon/3502-epoxy specimens with a L/h ratio of 4 for SBS specimens and 16 for FPS specimens were modeled. Whitney found that the results of the closed-form approximation are never completely recovered in the

SBS case, whereas in the FPS case, the shear stress close to the middle between the loading and support cylinders corresponds to the closed-form approximation. Another elasticity solution was developed by Sullivan and Van Oene [52] and applied to a unidirectional glass-reinforced vinyl ester composite with an orthotropy ratio (E_1/E_2) of 3.5, and to an isotropic material. The predicted shear stress distribution through specimen thickness was similar to that reported by Whitney [59].

Finite element models were extensively used for better modeling the boundary condition and nonlinear material behavior. These models range from simple linear analysis [15, 50] with simplified loading condition to more computational involved nonlinear analysis with nonlinear shear stress-strain response, contact interaction and geometric nonlinearity being taken into account [3, 22, 23, 26, 64, 66].

An early model was developed by Berg et al. [15] using a two-dimensional finite element analysis. The material behavior was assumed elastic-plastic and represented by a simple bilinear stress-strain relationship. The applied force was assumed to be uniformly distributed over a small length of the beam. Berg et al. also found that the actual distribution of shear stress never fully reaches the distribution from classical beam theory.

Cui and Wisnom [22, 23] conducted a more rigorous study by performing a non-linear two-dimensional finite element analysis with contact elements. Both linear and nonlinear shear models were used in their study, and the nonlinear shear response was assumed trilinear. They found that, if the material is assumed to be linear, a parabolic assumption for the shear stress distribution is good for large parts of the beam between the loading nose and supports. The influence of shear nonlinearity on the shear stress distribution was found to be significant in two-fold. First, taking account of the real nonlinear shear response of the material significantly reduced the shear stresses compared to the closed-form approximation. Second, the shear stresses were much more uniform near the middle of the section than the classical parabolic

distribution. The value of this uniform stress is about 15% lower than the maximum value given by equation (3.9).

Two-dimensional and three-dimensional nonlinear finite element models were developed by Xie and Adams [64, 66] by implementing a simplified contact algorithm in an in-house finite element code. The nonlinear shear response was approximately modeled by a plasticity model with isotropic hardening [20, 53, 65]. The span-to-thickness ratio was varied for 10 to 2 to investigate its effects on stress distributions in the beam specimen. It was observed that maximum shear stresses at the mid-thickness of all the specimens were lower than those predicted by equation (3.9), although the shear stress was still distributed parabolically. The numerical results revealed that the shear stresses at the mid-thickness decreased with decreasing span-to-thickness ratios. Thus equation (3.9) overestimates the shear strength for the specimen with lower span-to-thickness ratios. In addition, a comparison of two-dimensional analysis with three-dimensional analysis using five layers of elements in the width direction revealed no significant influence of width. Thus, one-layer model was used in their three-dimensional analysis.

A correction factor (α) was introduced by Cui and Wisnom [23] to quantitatively characterize the deficiency of the closed-form approximation, specially in the presence of pronounced shear nonlinearity. Equation (3.9) is modified through the correction factor α:

$$\sigma_{xz}^{\max} = \alpha \left(\frac{3}{4} \frac{P}{A} \right) \tag{5.1}$$

Note that α depends on shear nonlinearity, material orthotropy and specimen geometry since these factors affect the closed-form approximation (3.9) as revealed by previous studies. It is obvious that when the material is nonlinear, the shear stress will not be proportional to the applied load. Therefore, α is also a function of applied load [23].

5.2 Finite Element Analysis of SBS Specimens

5.2.1 Finite Element Models

To investigate the accuracy of the closed-form approximation (3.9) for the specimen configurations and the composite material systems used in this work, nonlinear finite element simulations were performed using the commercial finite element code ABAQUS [24].

Both two-dimensional and three-dimensional finite element models were used. Plane stress was assumed in the two-dimensional analysis. The finite element models involve geometric nonlinearity, material nonlinearity and contact interaction. Geometric nonlinearity was assumed to account for the large deformation in the vicinity of loading and support cylinders and the large deflection at mid-span. The nonlinear constitutive model, i.e., equation (2.7), was implemented in the finite element code via the user material subroutine UMAT as described in Chapter 2. Contact interaction was included to provide a more realistic approximation of loading transfer from fixture to beam specimen. The contact interaction between cylinders and beam specimen was modeled with the surface-to-surface contact algorithm in ABAQUS. The loading and supporting cylinders were assumed to be rigid and modeled with cylindrical surfaces. This assumption is reasonable because the stiffness of the cylinders, which are made of high stiffness steel, is much higher than the transverse stiffness of composites under study. Rigorous modeling of friction on contact surfaces is quite difficult as the friction depends on many factors of the contacting surface. To simplify the finite element analysis, the effect of friction was ignored and so only compressive forces can be transmitted across the interface. The finite element models were meshed with second-order continuum elements with reduced integration (i.e., the CPS8R elements for the plane stress analysis and the C3D20R elements for the three dimensional analysis). These elements are able to avoid shear locking in bending and thus are often used in ABAQUS for the bending problems [24].

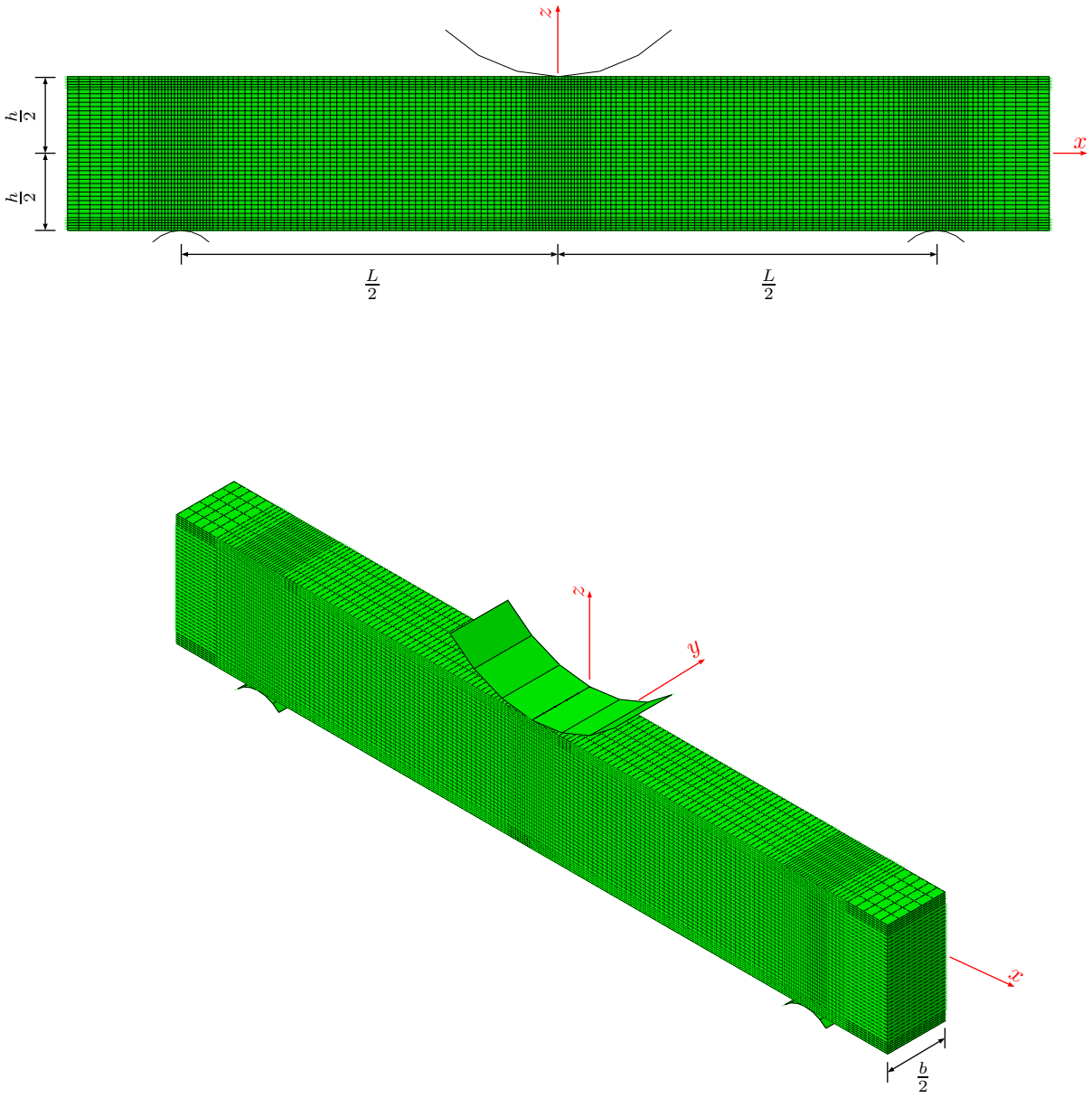

(b)

Figure 5.1: A typical finite element mesh of SBS specimen. (a) x-z plane view; (b) Three-dimensional view.

A typical finite element mesh is shown in Figure 5.1. Symmetry condition was applied in the width direction, therefore only half of the specimen was modeled in the three-dimensional approach. It is noted that, in order to accommodate the deviation of loading point from the midspan, no symmetry condition is assumed in the span direction. The finite element discretization in the x-z plane is similar to that used by Cui and Wisnom [23] in the plane stress analysis. A schematic of refined regions in mesh discretization is shown in Figure 5.2. The elements were refined along the longitudinal direction (x) in the areas where the specimen contacts the loading and support cylinders (L_1). Along the thickness direction (z), extremely small mesh size is employed in the top and bottom regions (T_1). In the three-dimensional model, relatively coarse mesh is used through the width direction (y) to save computational efforts.

A concentrated load P was applied at the reference point of loading cylinder (upper cylinder). The referent points of support cylinders (lower cylinders) were fixed so that no translation or rotation was allowed.

5.2.2 Mesh Convergence Study

Mesh convergence study was conducted to investigate the influence of mesh size on the stress distribution. Four meshes were used with plane stress elements and two meshes were used with three-dimensional elements. Table 5.1 summarizes the region dimensions of the mesh schemes and the number of elements employed in the regions. Mesh 4 varies from mesh 3 by refining mesh in the thickness direction. The element thickness is very small and no further refinement in this direction is considered. The three-dimensional meshes utilize the plane discretization of mesh 2 and the number of elements in width direction varies from case to case. Relatively coarse mesh was employed in the width direction for computational efficiency.

Table 5.1: Mesh schemes used in the mesh convergence study.

Region	Length	Number of Discretizations					
		Mesh 1	Mesh 2	Mesh 3	Mesh 4	Mesh 5	Mesh 6
L_1	$0.05L$	8	10	12	12	10	10
L_2	$0.04L$	4	5	8	8	5	5
L_3	$0.32L$	24	40	40	40	40	40
T_1	$0.08h$	3	5	5	7	5	5
T_2	$0.84h$	20	30	30	50	30	30
W	b					3	5

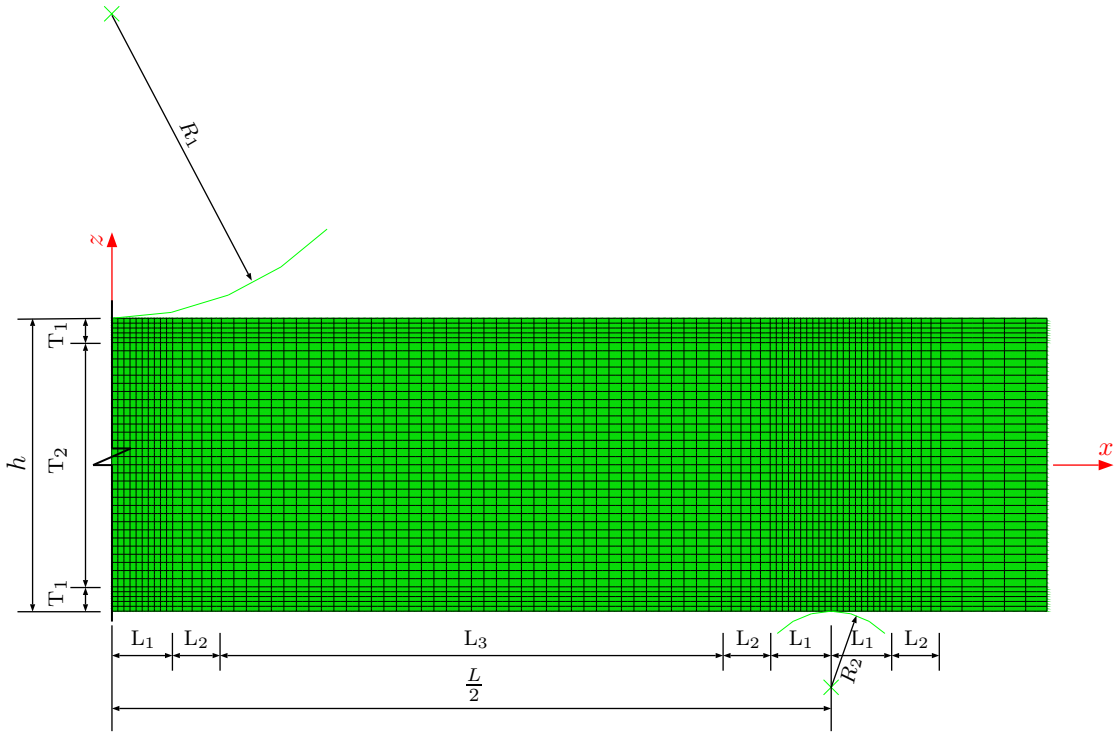

Figure 5.2: Schematic of refined regions in mesh discretization.

Table 5.2: Specimens used in the mesh convergence study.

Specimen	Material	Geometry			Load
		h	b	L	P
		mm (in.)	mm (in.)	mm (in.)	N (lbs)
S3	S2-glass/E773-epoxy	6.109 (0.2405)	6.299 (0.2480)	30.0 (1.18)	3501 (787)
S16	IM7-carbon/8552-epoxy	3.848 (0.1515)	3.086 (0.1215)	19.2 (0.76)	1312 (295)
S28	E-glass/5216-epoxy	6.007 (0.2365)	4.382 (0.1725)	25.4 (1.00)	2153 (484)

Table 5.3: Mesh convergence of a S2-glass/E773-epoxy tape SBS specimen at 3501 N (787 lbs) in the 1-3 material plane (Specimen S3).

	w_c		σ_{11}^{max}		σ_{13}^{max}	
	mm (in.)		MPa (ksi)		MPa (ksi)	
Closed-Form			$\sigma_a = 335.26$ (48.6)		$\sigma_s = 68.27$ (9.9)	
Mesh 1	-0.610 (-0.0240)		337.7 (48.98)		65.0 (9.42)	
Mesh 2	-0.610 (-0.0240)		337.8 (49.00)		64.9 (9.42)	
Mesh 3	-0.610 (-0.0240)		337.6 (48.97)		64.9 (9.42)	
Mesh 4	-0.610 (-0.0240)		337.6 (48.96)		64.9 (9.42)	
	$z = 0$	$y = -b/2$	$y = 0$	$y = -b/2$	$y = 0$	$y = -b/2$
Mesh 5	-0.606 (-0.0238)	-0.615 (-0.0242)	339.9 (49.29)	335.0 (48.59)	64.4 (9.35)	65.7 (9.53)
Mesh 6	-0.606 (-0.0238)	-0.615 (-0.0242)	339.8 (49.29)	335.1 (48.61)	64.5 (9.35)	65.7 (9.53)

Three SBS specimens, each corresponds to one of the three composite material systems under study, were adopted in the mesh convergence study. The specimen dimensions are listed in Table 5.2. Loading magnitudes used in the finite element simulations are also listed. The diameter of loading cylinder (R_1) is 12.7 mm (0.50 inches) for Specimens S3 and S16 and 9.5 mm (0.375 inches) for Specimen S28. The diameter of supports (R_2) is 3.2 mm (0.125 inches) for all cases.

Table 5.4: Mesh convergence of an IM7-carbon/8552-epoxy tape SBS specimen at 1312 N (295 lbs) in the 1-3 material plane (Specimen S16).

	w_c mm (in.)		σ_{11}^{max} MPa (ksi)		σ_{13}^{max} MPa (ksi)	
Closed-Form			$\sigma_a = 414.12$ (60.1)		$\sigma_s = 83.00$ (12.0)	
Mesh 1	-0.230 (-0.00904)		454.0 (65.84)		75.8 (10.99)	
Mesh 2	-0.230 (-0.00904)		453.6 (65.78)		75.8 (10.99)	
Mesh 3	-0.230 (-0.00904)		453.9 (65.83)		75.8 (10.99)	
Mesh 4	-0.230 (-0.00904)		453.8 (65.82)		75.8 (10.99)	
	$y = 0$	$y = -b/2$	$y = 0$	$y = -b/2$	$y = 0$	$y = -b/2$
Mesh 5	-0.227 (-0.00893)	-0.230 (-0.00905)	459.8 (66.68)	443.9 (64.39)	75.4 (10.93)	76.4 (11.09)
Mesh 6	-0.227 (-0.00893)	-0.230 (-0.00905)	459.7 (66.67)	444.1 (64.41)	75.4 (10.94)	76.4 (11.09)

These meshes are analyzed consecutively and the results are summarized in Tables 5.3, 5.4 and 5.5 for Specimens S3, S16, S28, respectively. The maximum vertical displacement w_c is used to examine the influence of mesh size on the structural stiffness. This value is extracted from the node located at the bottom of the midspan section ($x = 0$, $z = -h/2$). The stress distributions across the gage section (i.e., $x = L/4$ or $x = -L/4$) is the major concern. The maximum axial stress σ_{11}^{max} is extracted from the node located at the bottom of gage section, and σ_{13}^{max} is the maximum interlaminar shear stress on the gage section. From the tables, it can be seen that the mesh refining process are well converged for general stiffness analyses. The mesh size has little influence on the maximum axial and shear stresses of the gage section. Moreover, the mesh influence in the width direction can be neglected.

Plane stress mesh 2 and three-dimensional mesh 6 will be used in the subsequent simulations. The three-dimensional model consists of 36,000 elements and the total number of variables (degrees of freedom plus Lagrange multiplier variables) in the

Table 5.5: Mesh convergence of an E-glass/5216-epoxy tape SBS specimen at 2153 N (484 lbs) in the 1-2 material plane (Specimen S28).

	w_c mm (in.)		σ_{11}^{max} MPa (ksi)		σ_{13}^{max} MPa (ksi)	
Closed-Form			$\sigma_a = 259.58$ (37.6)		$\sigma_s = 60.39$ (8.9)	
Mesh 1	-0.417 (-0.0164)		265.1 (38.45)		58.1 (8.42)	
Mesh 2	-0.417 (-0.0164)		265.5 (38.51)		58.0 (8.42)	
Mesh 3	-0.417 (-0.0164)		265.3 (38.47)		58.0 (8.42)	
Mesh 4	-0.417 (-0.0164)		265.3 (38.47)		58.0 (8.42)	
	$y = 0$	$y = -b/2$	$y = 0$	$y = -b/2$	$y = 0$	$y = -b/2$
Mesh 5	-0.414 (-0.0163)	-0.418 (-0.0165)	267.2 (38.76)	263.4 (38.20)	57.7 (8.37)	58.4 (8.48)
Mesh 6	-0.414 (-0.0163)	-0.419 (-0.0165)	267.2 (38.75)	263.5 (38.22)	57.7 (8.37)	58.4 (8.48)

model is 513,930. Thus the three-dimensional analysis is computational expensive. It took about 10 hours CPU time to run a single analysis on a workstation with a 2.33 GHz CPU and 8 GB memory assigned. However, a two-dimensional analysis only took less than 2 minutes.

5.2.3 Finite Element Stress Analysis

The stress distributions from finite element simulations are plotted through the thickness to compare with the classical beam theory for axial stress [56]:

$$\sigma_x = -\frac{Mz}{I} \tag{5.2}$$

and the classical beam theory for shear stress, i.e., equation (3.14):

$$\sigma_{xz} = \frac{3}{4}\frac{P}{A}\left[1 - \left(\frac{2z}{h}\right)^2\right] \tag{3.14}$$

The axial stress distribution is normalized with respect to σ_a, i.e., the maximum

axial stress from the closed-from solution of homogeneous beam (5.2):

$$\sigma_{\mathrm{a}} = -\frac{M}{I}\left(-\frac{h}{2}\right) = \frac{M}{S} \tag{5.3}$$

where $S = bh^2/6$ is the section modulus of the rectangular cross-sectional area. The shear stress distribution is normalized with respect to σ_{s}, i.e., the maximum shear stress given by equation (3.9).

Figure 5.3 shows the stress distributions across various sections of the S2-glass composite specimen (S3) from plane stress analysis. Figure 5.4 shows the shear stress distributions across the gage section (i.e., $x = L/4$ or $x = -L/4$) at various loading magnitudes for the Specimen S3 and the carbon composite specimen (S16). The axial and shear stress distributions across the gage section are shown in Figures 5.5, 5.6 and 5.7 for the Specimens S3, S16 and the E-glass composite specimen (S28) respectively at loads close to failure. To investigate the width-wise stress variation, in each case, stress distributions from three-dimensional analysis were plotted for the symmetry edge ($y = 0$) and the outside edge ($y = -b/2$) in conjugation with the plane stress result. The width-wise shear stress variation was further investigated by varying the specimen width-to-thickness (b/h) ratio. Figure 5.8 shows the shear stress distributions across the width for Specimen S3. Three aspect ratios were studied, e.g., b/h=0.50, 1.03 and 2.00, in which the aspect ratio of 1.03 is the actual configuration. The specimen S16 was also studied by increasing the width-to-thickness ratio from 0.80 to 2.00, the results are shown in Figure 5.9.

Several observations can be made from Figures 5.3-5.9:

1. The parabolic distribution is acceptable for the gage section midway between loading nose and support points. However, for sections close to loading or support cylinders (e.g., sections A and C in Figure 5.3), this assumption is invalid due to the local stress concentration effects. The shear stress distributions can be seen to be skewed, with peak stresses occurring near the loading nose and

support points.

2. The maximum shear stresses of all the specimens are lower than that predicted by the closed-form approximation (3.9). Moreover, the discrepancy is found to be material dependent. Much larger discrepancy can be observed in the carbon composite specimen (S16).

3. As indicated in Figure 5.5, the discrepancy is also a function of load. Furthermore, the discrepancy increases dramatically at the final stage of loading.

4. The axial stress distributed linearly across the gage section for the glass composite specimens (S3 and S28). Minor deviation can be observed in the carbon composite specimen (S16), where the stress distribution remains linearly across major portion of the thickness and becomes skewed toward the bottom edge.

5. The widthwise shear stress variation is small in all cases. This observation is consistent with the numerical results in Reference [66]. In addition, as one can expect, through-the-thickness distribution from plane stress analysis is between the distribution on the symmetry edge ($y = 0$) and the distribution on the outside edge ($y = -b/2$) from three-dimensional analysis.

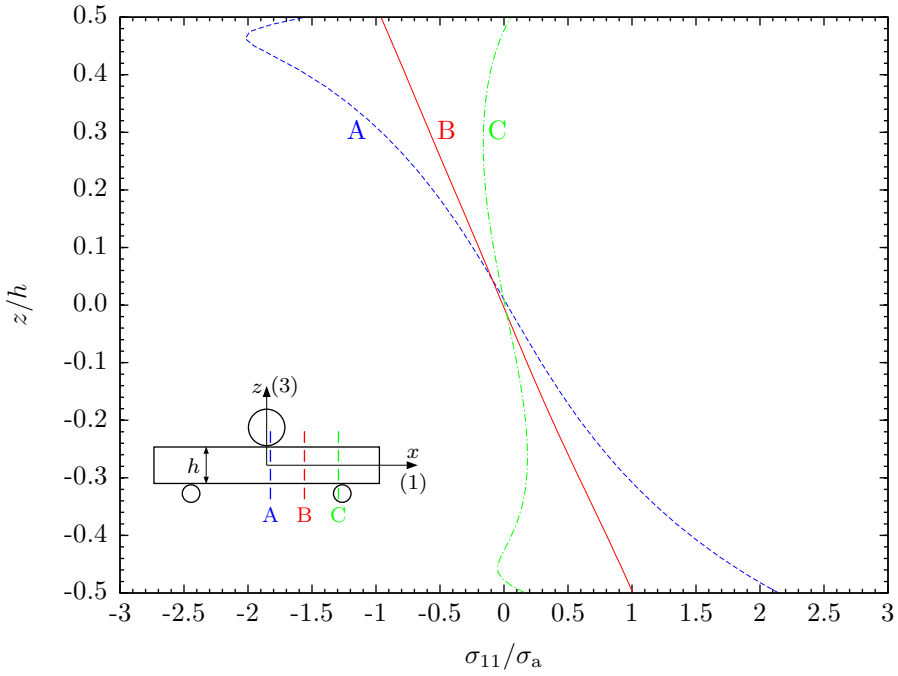

(a)

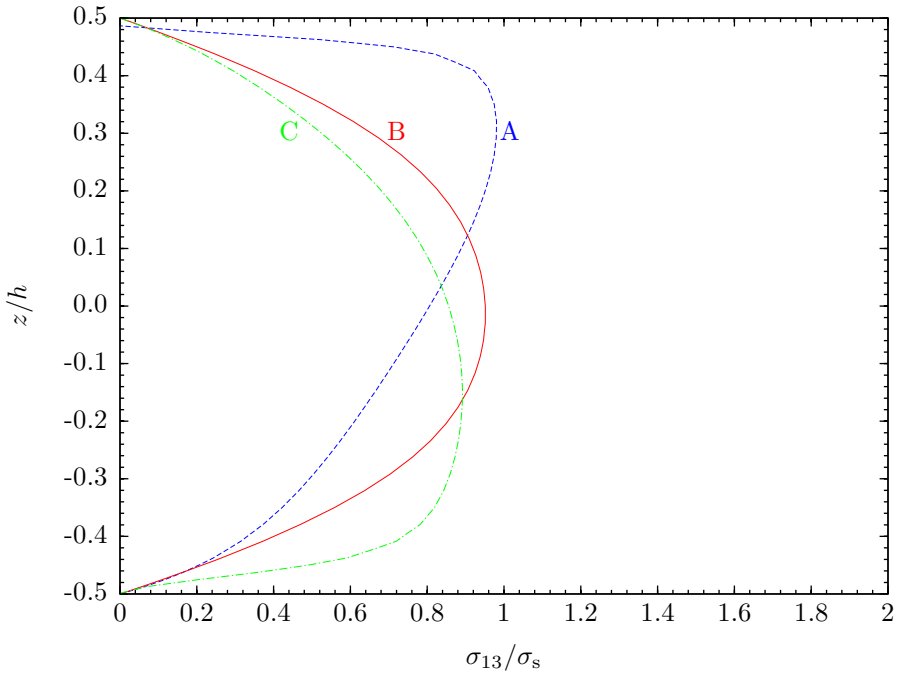

(b)

Figure 5.3: Through thickness stress distributions across several sections for a S2-glass/E773-epoxy tape SBS specimen at load 3501 N (787 lbs) 95% failure load in the 1-3 material plane (Specimen S3). (a) Axial stress; (b) Shear stress.

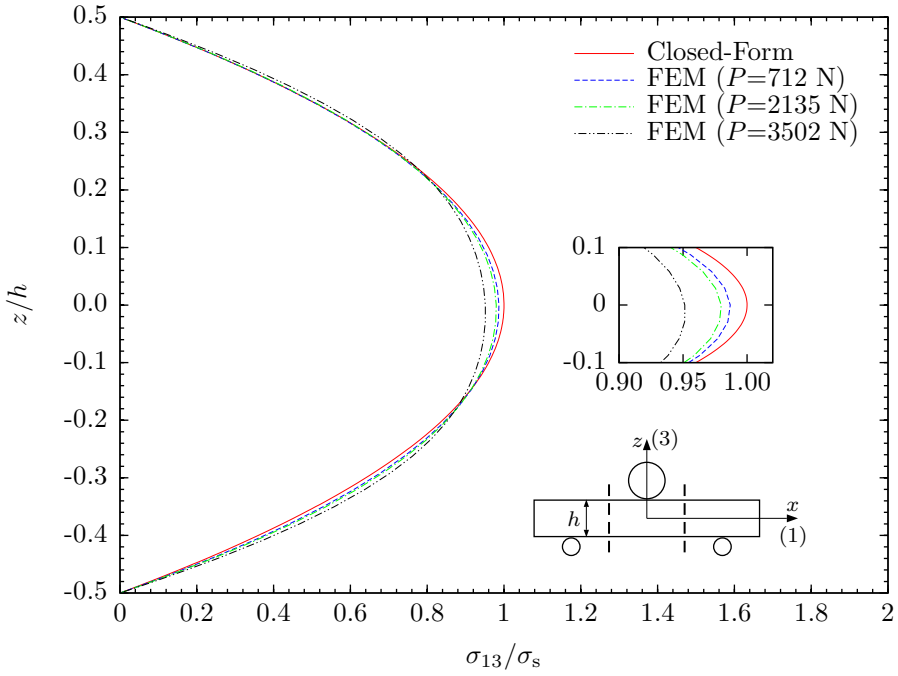

(a)

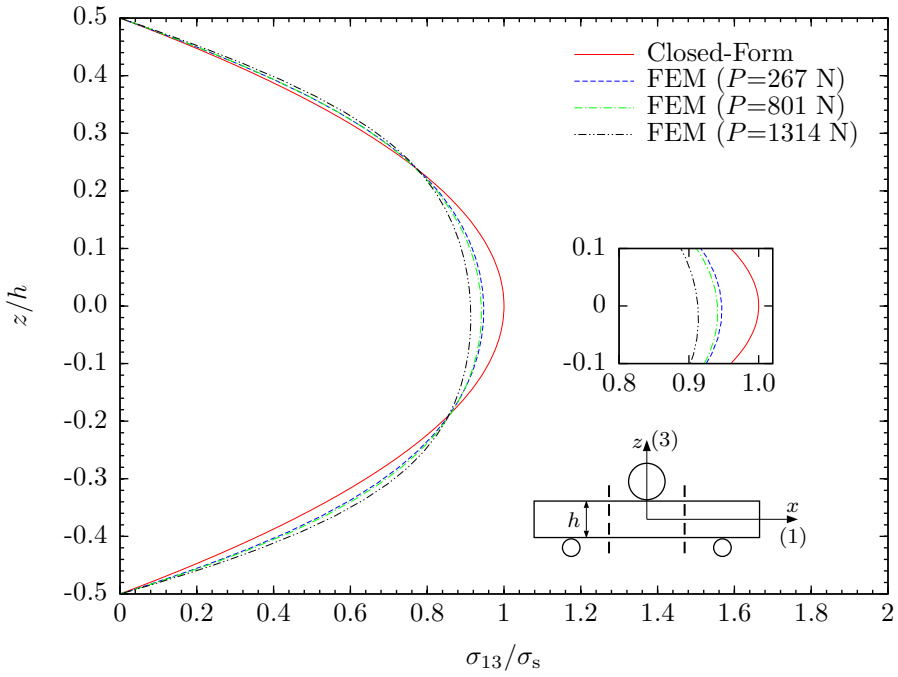

(b)

Figure 5.4: Through thickness stress distributions at several load levels. (a) S2-glass/E773-epoxy tape SBS specimen (Specimen S3); (b) IM7-carbon/8552-epoxy tape SBS specimen (Specimen S16).

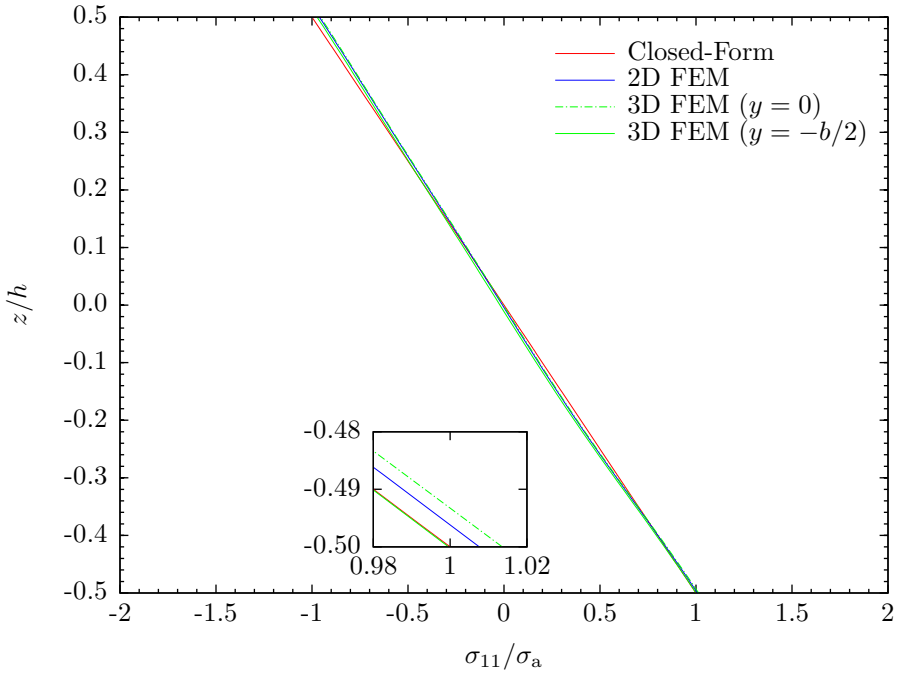

(a)

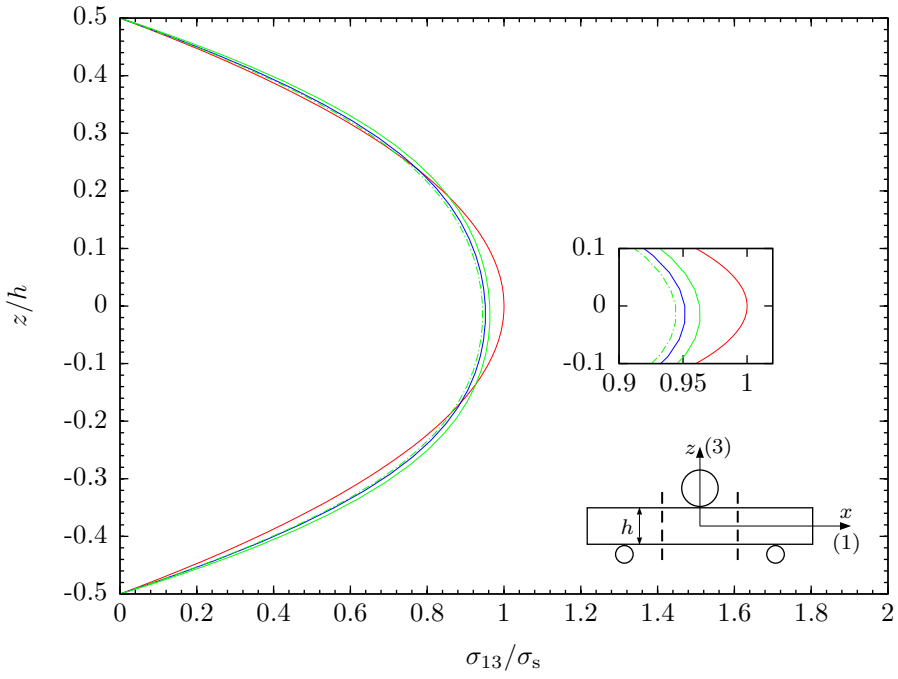

(b)

Figure 5.5: Through thickness stress distributions for a S2-glass/E773-epoxy tape SBS specimen at load 3501 N (787 lbs) 95% failure load in the 1-3 material plane (Specimen S3). (a) Axial stress; (b) Shear stress.

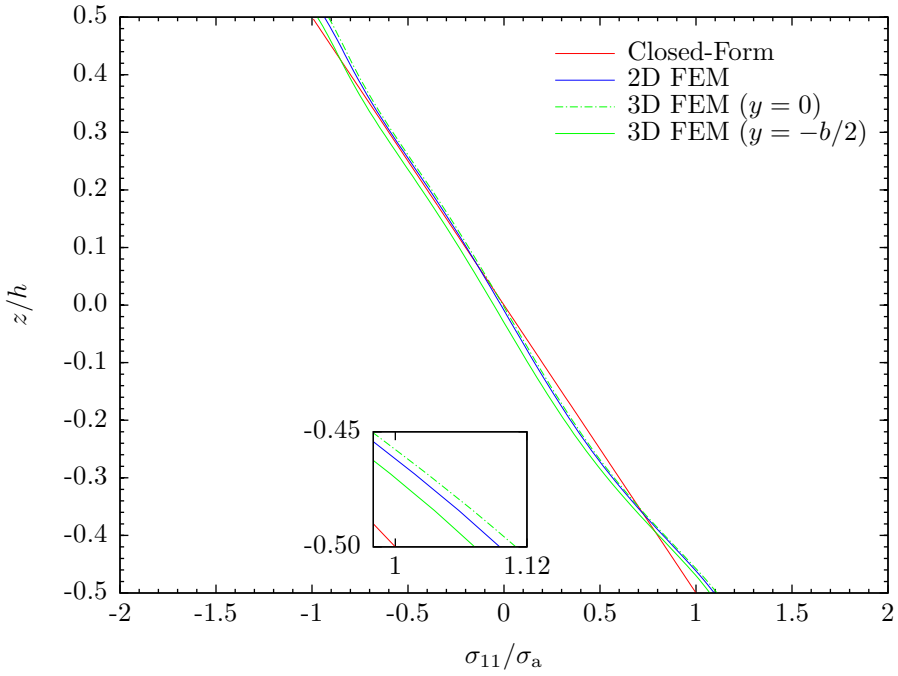

(a)

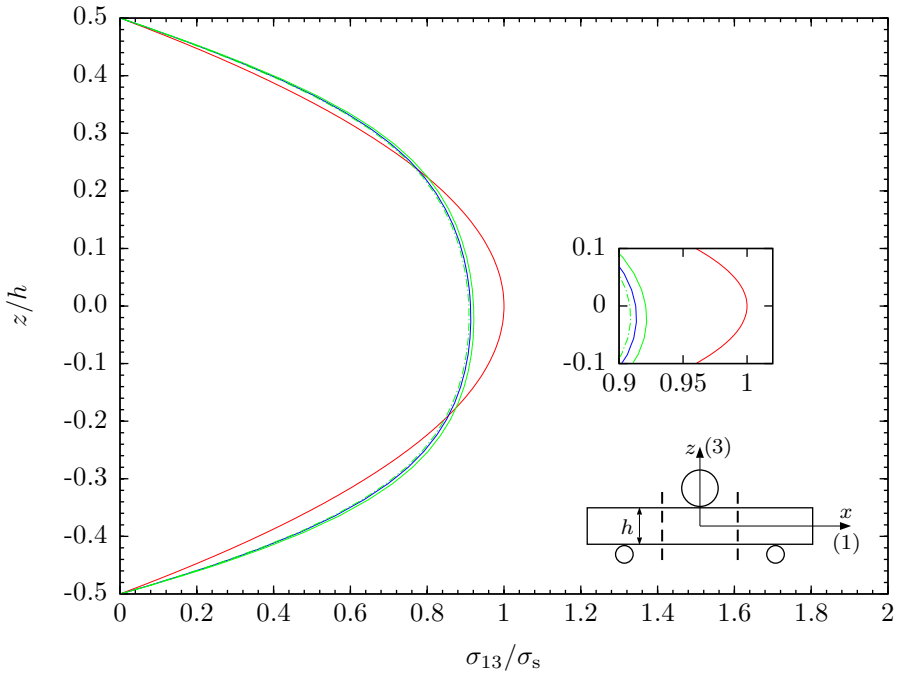

(b)

Figure 5.6: Through thickness stress distributions for an IM7-carbon/8552-epoxy tape SBS specimen at load 1312 N (295 lbs) 82% failure load in the 1-3 material plane (Specimen S16). (a) Axial stress; (b) Shear stress.

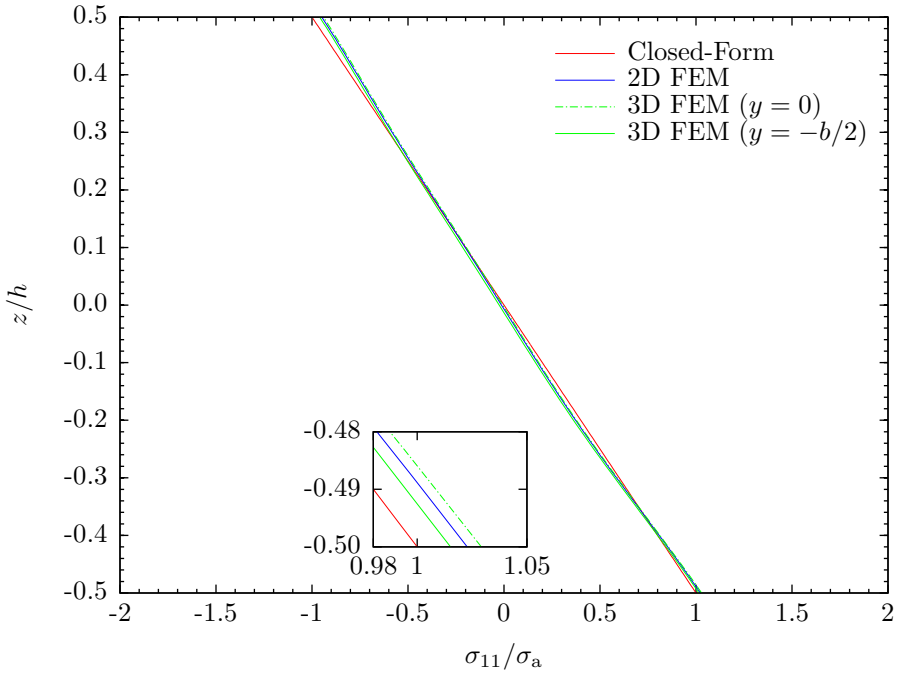

(a)

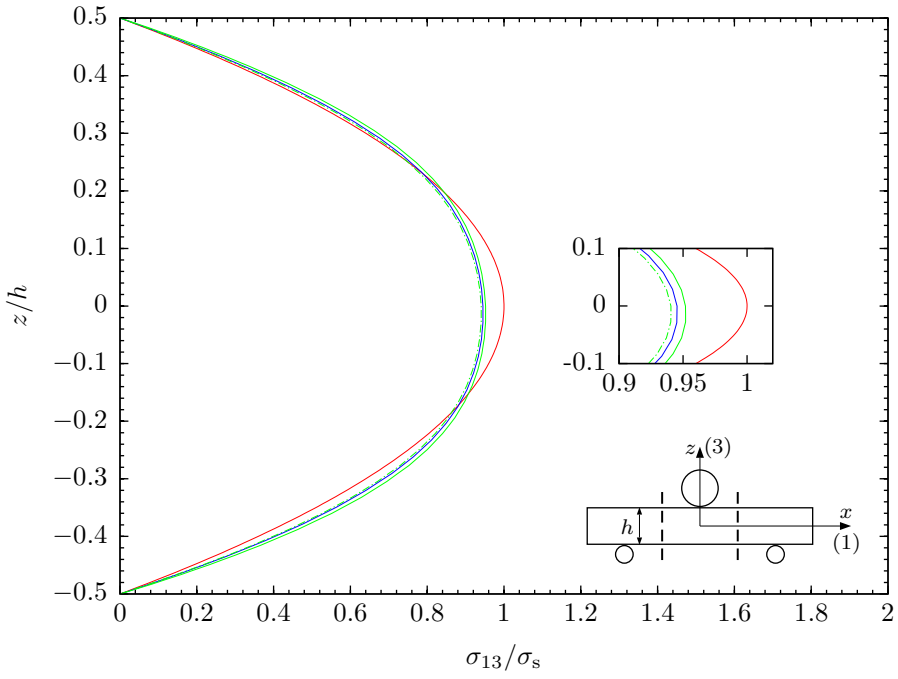

(b)

Figure 5.7: Through thickness stress distributions for an E-glass/5216-epoxy tape SBS specimen at load 2153 N (484 lbs) 92% failure load in the 1-3 material plane (Specimen S28). (a) Axial stress; (b) Shear stress.

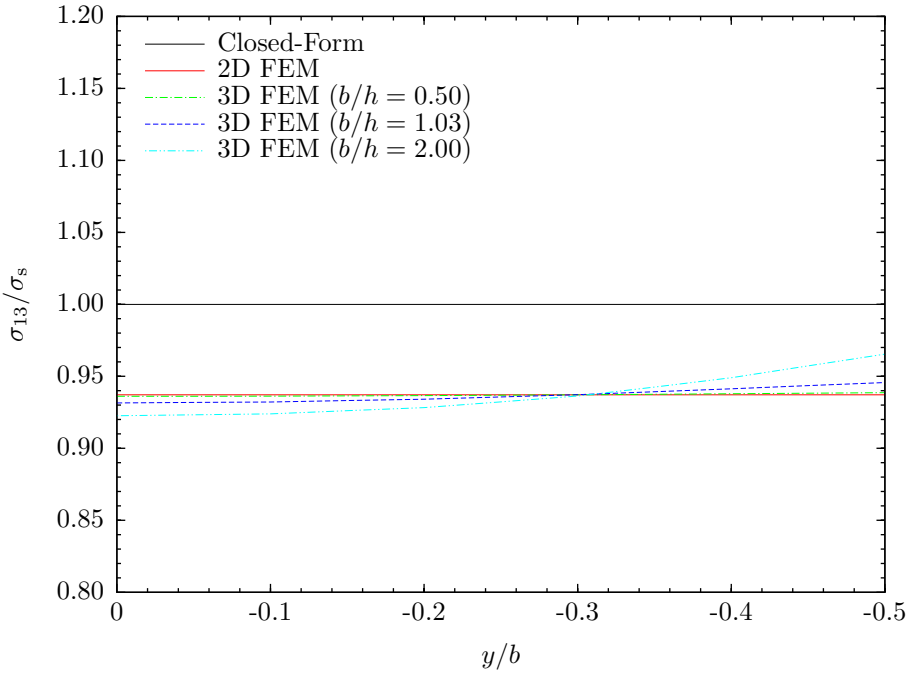

Figure 5.8: Through width shear stress distribution for a S2-glass/E773-epoxy SBS specimen with various width-to-thickness ratios (Specimen S3).

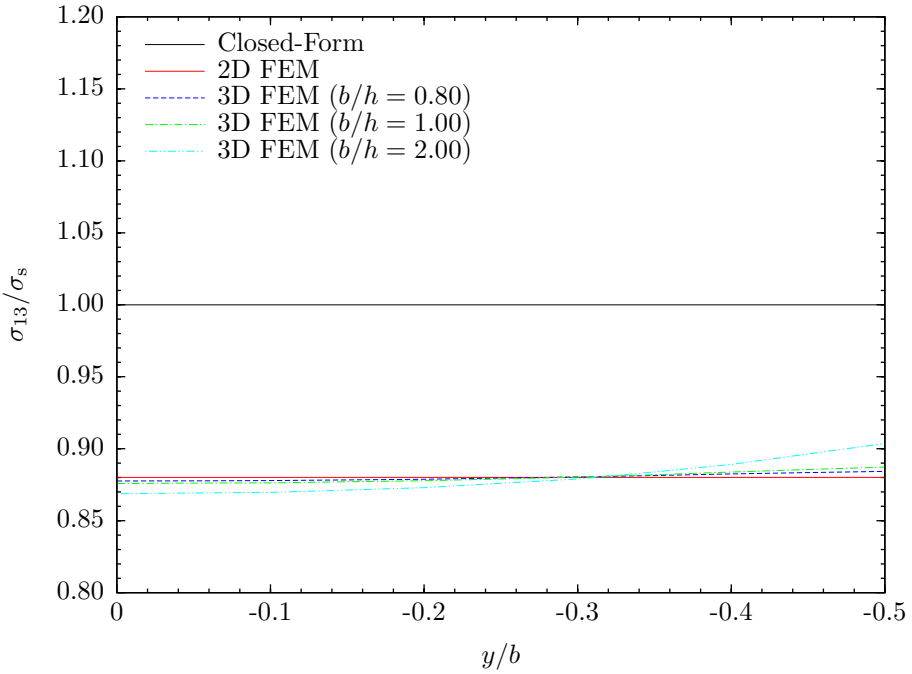

Figure 5.9: Through width shear stress distribution for an IM7-carbon/8552-epoxy SBS specimen with various width-to-thickness ratios (Specimen S16).

5.3 Iterative Procedure for Stress Updating

The inadequacy of classical beam theory in describing the stress state in the SBS specimen, observed in a number of studies and indicated in the ASTM Standard D 2344 [11], was again demonstrated in the stress analyses presented in the previous section. The nonlinear shear properties obtained in Chapter 3 were based on the closed-form approximation (3.9). As a result, the discrepancy may induce additional experimental error in the material characterization and in most cases may lead to overestimated shear modulus. Therefore more accurate stress analysis is needed to minimize the induced error. Either elasticity analysis [52,59] or finite element analysis can be used. However, finite element analysis is preferred due to its flexibilities to incorporate nonlinear constitutive model and realistic contact condition.

An iterative procedure is developed to characterize the shear properties using the stress state obtained from finite element analysis. The flow chart of the iterative procedure is shown in Figure 5.7. The first step of the iterative procedure is to assess the shear properties using the test method developed in Chapter 3. The shear properties obtained by closed-form based stress are used as initial approximation and implemented in the first finite element simulation. The maximum shear stress $(\sigma_{xz}^{\max})_{\mathrm{FE}}$ on gage section (i.e., $x = L/4$ or $x = -L/4$) is extracted from finite element simulation and compared with the closed-form approximation σ_{s} calculated from equation (3.9). If the difference is within a tolerance, the accuracy of closed-from approximation is verified and no update on the shear properties is needed. Otherwise, the FE-based stresses are used in conjugation with strain data from DIC measurement to obtain new shear properties. The material properties are then updated in the finite element model and a new simulation is performed. Again, maximum shear stress on gage section is extracted and shear properties are updated. The iterative procedure continues until the amount of update is within a tolerance.

It is noted that the number of iterations dependent on the variation of the maximum shear stress $(\sigma_{xz}^{\max})_{\mathrm{FE}}$ in consecutive simulations. The modification of shear properties affects the contact interaction and consequently the local stress concentration. Thus, the stress state in the nonlinear analysis is material dependent. The update on material properties may change the maximum shear stress on the gage section due to the effects of stress concentration. However, as will be demonstrated in next chapter, the maximum shear stress converges rapidly and thus only a few simulations are needed in the iterative procedure.

The load increments in a finite element simulation might not exactly follow the load readings in a test. Nevertheless, the load readings can be converted to FE-based stresses according to equation (5.1) as long as the correction factor α is characterized by finite element simulation as a function of incremental load. An interpolation procedure is described in the following.

At each iteration, the maximum shear stress $(\sigma_{xz}^{\max})_{\mathrm{FE}}$ on the gage section is extracted from finite element analysis at every load increment P_{FE}. The discrepancy with respect to the corresponding closed-form approximation (σ_{s}) at load P_{FE} is quantified by

$$\alpha = \frac{(\sigma_{xz}^{\max})_{\mathrm{FE}}}{\sigma_{\mathrm{s}}} = \frac{(\sigma_{xz}^{\max})_{\mathrm{FE}}}{\frac{3P_{\mathrm{FE}}}{4A}} \tag{5.4}$$

Third-order polynomial equation

$$\alpha = A_3 \left(\frac{P_{\mathrm{FE}}}{b}\right)^3 + A_2 \left(\frac{P_{\mathrm{FE}}}{b}\right)^2 + A_1 \left(\frac{P_{\mathrm{FE}}}{b}\right) + A_0 \tag{5.5}$$

or four-order polynomial equation

$$\alpha = A_4 \left(\frac{P_{\mathrm{FE}}}{b}\right)^4 + A_3 \left(\frac{P_{\mathrm{FE}}}{b}\right)^3 + A_2 \left(\frac{P_{\mathrm{FE}}}{b}\right)^2 + A_1 \left(\frac{P_{\mathrm{FE}}}{b}\right) + A_0 \tag{5.6}$$

is applied to fit the relationship between the discrepancy (α_{FE}) and load per unit width (P_{FE}/b) using a least squares procedure. Therefore, the FE-based stress for each load reading P can be calculated from equation (5.1) using equation (5.5) or

(5.6) for load per unit width (P/b):

$$\alpha = \alpha\left(\frac{P}{b}\right) \tag{5.7}$$

It is worth noting that the interpolation procedure is not needed if the load readings are defined as the load steps in solution control of a finite element simulation.

It is also noted that some approaches in the finite element model updating technique used in structural dynamics also utilize an iterative procedure with consecutive finite element simulations. The finite element model updating technique has emerged in the 1990s to predict the dynamic characteristics of engineering structures and is still an active research area [42]. Due to inaccuracy in the model and imprecision and lack of information in measurements, the finite element simulations often give dynamic responses that differ from the measured results and therefore need to be updated to match the measured data. In the model updating, some of the parameters (e.g., material properties) are adjusted to reduce a penalty function based on residuals between a measurement set and corresponding model predictions. Typical measurements include modal parameters (natural frequencies and mode shapes) and the frequency response function [27]. An optimization procedure can be used to update the parameters by minimizing the penalty function.

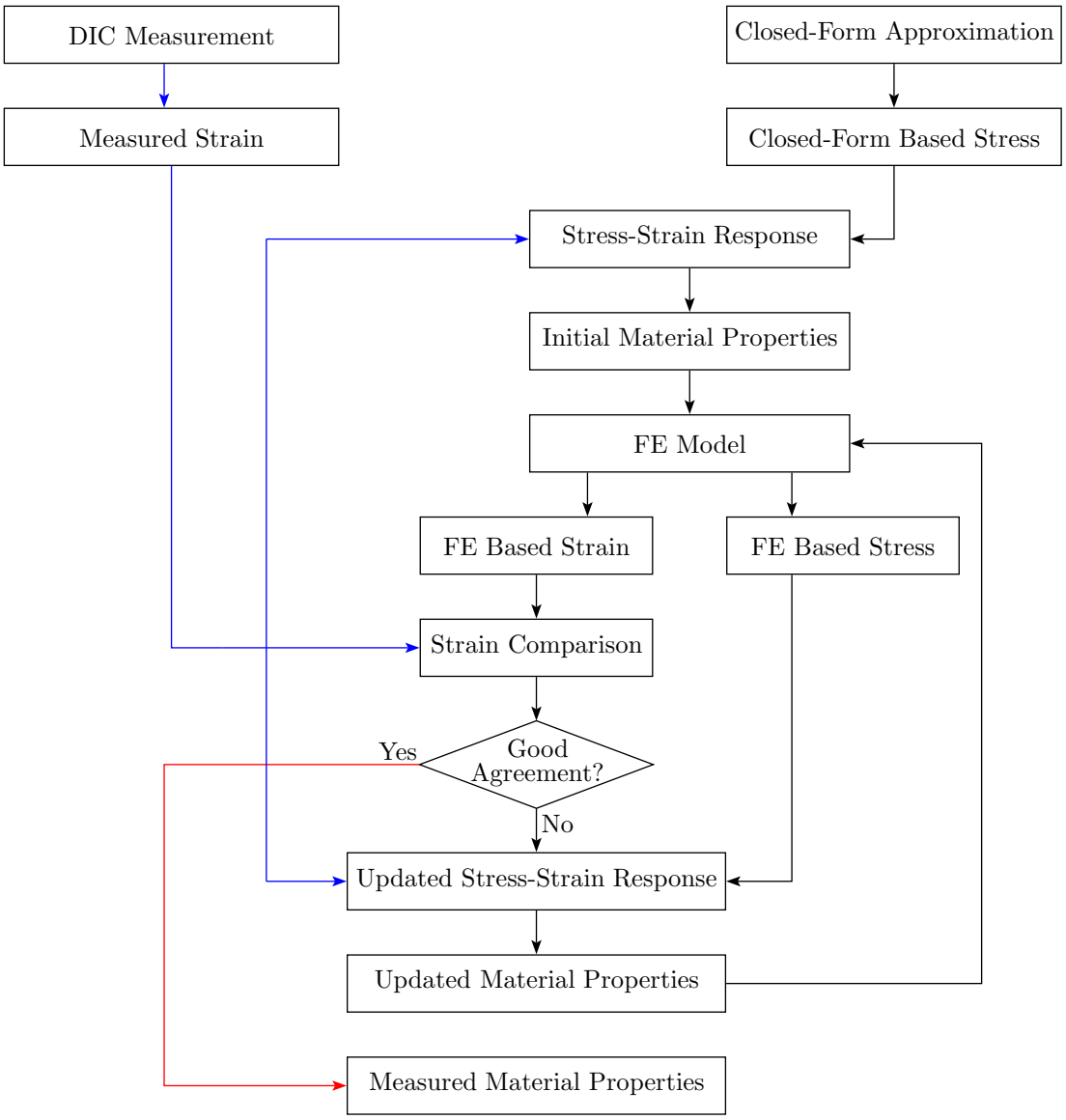

Figure 5.10: Flow chart of the iterative procedure for material properties assessment.

CHAPTER VI

NUMERICAL RESULTS FOR UPDATED SHEAR PROPERTIES

6.1 S2-Glass/E773-Epoxy SBS Specimens

6.1.1 Specimens Loaded in 1-3 Material Plane

The iterative procedure was applied to update the shear properties for the unidirectional S2-glass/E773-epoxy tape composite. Numerical results for the specimens loaded in the 1-3 material plane are summarized in Table 6.1. The initial values, that is, the properties used in the first finite element simulation of the iterative procedure, were obtained using closed-form based stresses as described in Chapter 3. These properties are listed in Table 3.2 (on Page 33) and repeated here for comparison purpose. The iterative procedure converged rapidly and only four iterations were used for each specimen.

Two important observations are made from Table 6.1. First, the update on linear shear stiffness G_{13} is negligible due to the small discrepancy of the closed-form solution in small strain region (e.g., $\gamma_{13} < 5000\mu\epsilon$). As illustrated in Figure 5.4(a), for the S2-glass composite specimen (S3), the closed-form approximation is indeed very close to the finite element prediction at lower load level. Second, the iterative procedure does not significantly exaggerate the experimental scatter. The values of coefficient of variance for the updated values are consistent with their counterparts for the initial values.

To demonstrate the iterative procedure, detailed numerical results for the Specimen S3 are presented. Table 6.2 summarizes the iterative results for the nonlinear shear properties. The third-order polynomial (5.5) was used to fit the coefficient

factor using the finite element results and the iterative values are listed in Table 6.3.

The iterative procedure for the correction factor (α) is plotted in Figure 6.1(a) as a function of load per unit width (P/b), and the iterative procedure for the nonlinear shear stress-strain response is shown in Figure 6.1(b). It can be clearly observed from both figures that the iterative procedure converges rapidly and a major update occurs at the first iteration.

Table 6.1: Updated shear properties for the unidirectional S2-glass/E773-epoxy tape SBS specimens in the 1-3 material plane.

Specimen	Initial Values			Updated Values		
	G_{13} GPa (msi)	K_{13} MPa (ksi)	n_{13}	G_{13} GPa (msi)	K_{13} MPa (ksi)	n_{13}
S1	4.23 (0.614)	194 (28.1)	0.223	4.23 (0.613)	167 (24.2)	0.210
S2	4.11 (0.596)	191 (27.6)	0.219	4.04 (0.587)	159 (23.1)	0.200
S3	4.09 (0.594)	192 (27.9)	0.218	4.09 (0.593)	169 (24.6)	0.211
S4	4.23 (0.613)	186 (27.0)	0.212	4.17 (0.605)	165 (23.9)	0.202
S5	4.15 (0.602)	192 (27.8)	0.222	4.11 (0.596)	170 (24.6)	0.213
AVE	4.16 (0.604)	191 (27.7)	0.219	4.13 (0.599)	166 (24.1)	0.207
COV	1.56%	1.47%	1.93%	1.72%	2.58%	2.69%

Table 6.2: Iterative results of shear properties for a S2-glass/E773-epoxy tape SBS specimen in the 1-3 material plane (Specimen S3).

	Initial Values	Iteration 1	Iteration 2	Iteration 3	Iteration 4
G_{13} GPa (msi)	4.09 (0.594)	4.09 (0.593)	4.09 (0.593)	4.09 (0.593)	4.09 (0.593)
K_{13} MPa (ksi)	192 (27.9)	177 (25.7)	172 (24.9)	170 (24.6)	169 (24.6)
n_{13}	0.218	0.216	0.213	0.211	0.211

Table 6.3: Iterative results of correction factor coefficients for a S2-glass/E773-epoxy tape SBS specimen in the 1-3 material plane (Specimen S3).

	Iteration 1	Iteration 2	Iteration 3	Iteration 4
A_4, $(\text{in./lbs})^4$	2.75774E-13	4.94725E-13	5.56226E-13	5.73527E-13
$(\text{mm/N})^4$	(2.59396E-16)	(4.65344E-16)	(5.23192E-16)	(5.39466E-16)
A_3, $(\text{in./lbs})^3$	-5.21083E-10	-7.91278E-10	-8.82590E-10	-9.11322E-10
$(\text{mm/N})^3$	(-2.79875E-12)	(-4.24998E-12)	(-4.74042E-12)	(-4.89474E-12)
A_2, $(\text{in./lbs})^2$	1.01644E-07	1.57790E-07	1.84962E-07	1.94770E-07
$(\text{mm/N})^2$	(3.11735E-09)	(4.83933E-09)	(5.67266E-09)	(5.97348E-09)
A_1, (in./lbs)	-6.77270E-06	-1.11658E-05	-1.34805E-05	-1.43605E-05
(mm/N)	(-1.18608E-06)	(-1.95543E-06)	(-2.36080E-06)	(-2.51491E-06)
A_0	9.86989E-01	9.87022E-01	9.87040E-01	9.87056E-01

Figure 6.2 shows the iterative results for the interlaminar shear strain from finite element simulations, the DIC measurements on the left gage section ($x = -L/4$) and the right gage section ($x = L/4$) are also shown for comparison. The strain distribution from the first finite element simulation is significantly deviated from the DIC data. However, after the first correction on shear properties, the strain distributions from consequent finite element simulations agree well with the DIC data. Thus good agreement on shear strain comparison can be achieved even only a single iteration is used. Figure 6.2(b) shows the iterative results for the shear stress distributions through the thickness and the closed-from approximation (3.14) is plotted as a baseline. Again, significant modification occurs only at the first iteration and the variations of stress distributions from consequent finite element simulations are negligible. This explains why the numerical procedure may converge. The iterative procedure is essentially controlled by the stress updating in consecutive finite element simulations.

Figures 6.3(a) and 6.3(b) show shear stress-strain response generated using closed-form and FE-based solution on the left gage section and the right gage section for all five SBS specimens tested. It is worth mentioning that the initial and updated shear

properties listed in Table 6.1 were indeed obtained by fitting these shear stress-strain relations using a least squares approximation.

Figure 6.4 shows the comparisons of DIC measurements with finite element results for the axial strain (ϵ_{11}), transverse strain (ϵ_{33}), and shear strain (γ_{13}) on the beam surface ($y = -b/2$). It is noted in the figure that the compressive stress concentration are reasonably well localized in the bending, confirmed by experimental and numerical results. It is seen that the overall agreement is excellent between the finite element results and DIC data. Locally in the stress concentration regions, some differences between the finite element results and DIC data are evident, and the finite element models predicted larger deformation than the DIC measurements. This is attributed mainly to the inadequacies of the nonlinear shear model in very large strain regime (e.g., $\gamma_{13} > 5\%$). The cylinders/specimen contact uncertainties also account for these departures.

Figure 6.5(a) shows the comparison of DIC measurements with finite element results for the axial strain across the gage sections. The axial strain distributions are linearly distributed through the thickness and excellent agreement is clearly indicated. The comparison for shear strain distributions are shown in Figure 6.5(b). The shear strains are parabolically distributed across the gage section and good agreement can be observed.

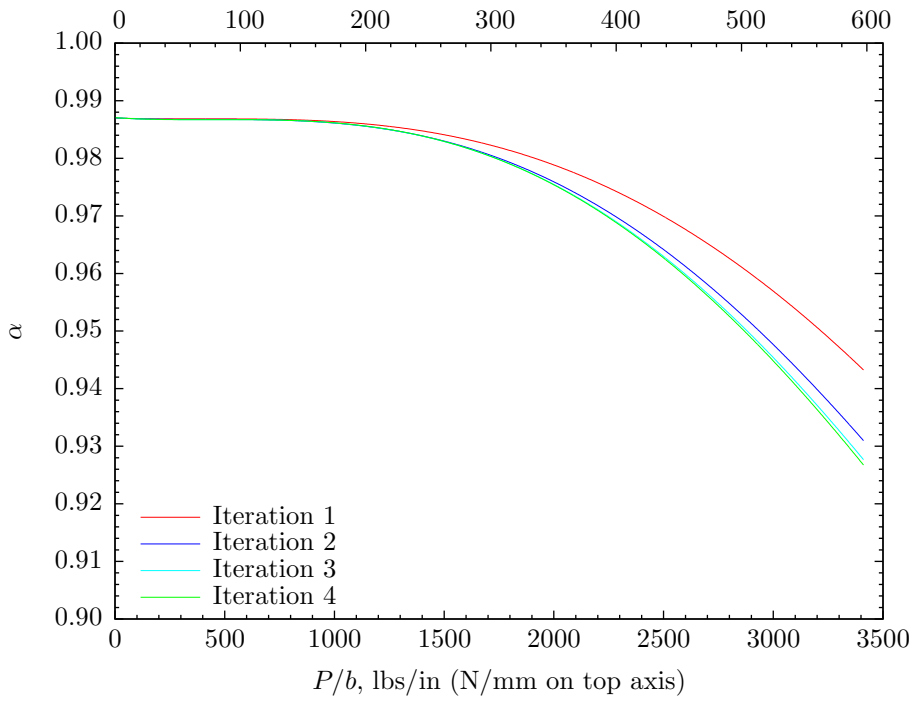

(a)

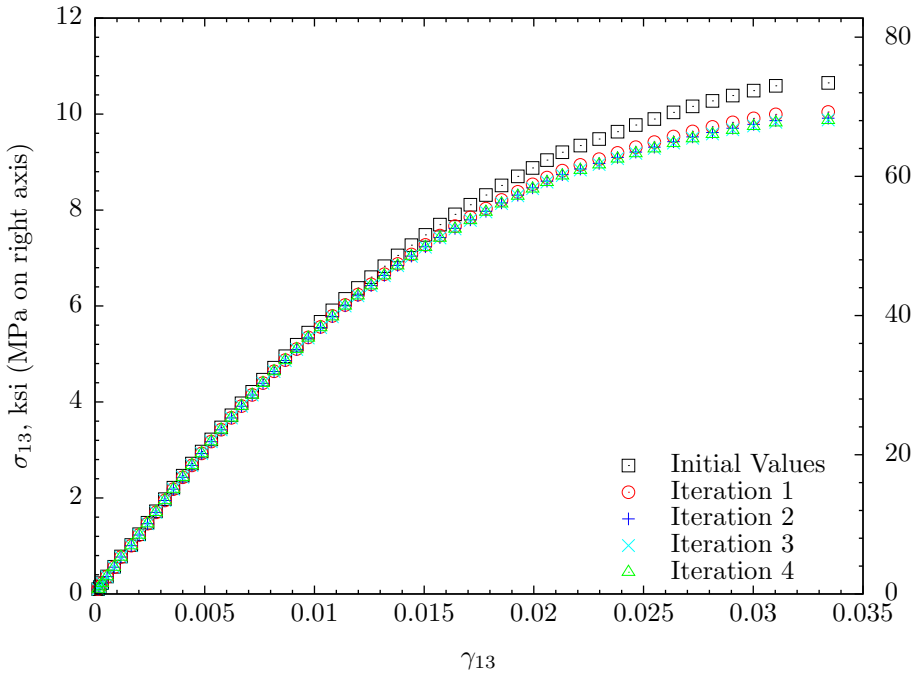

(b)

Figure 6.1: Iterative results for a S2-glass/E773-epoxy tape SBS specimen in the 1-3 material plane (Specimen S3). (a) Correction factor; (b) Shear stress-strain response.

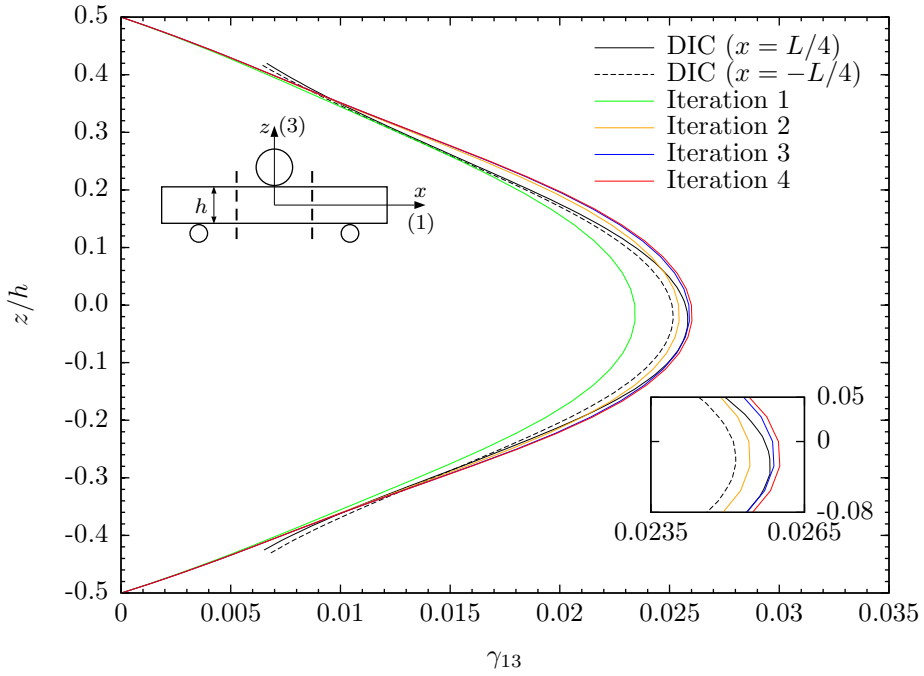

(a)

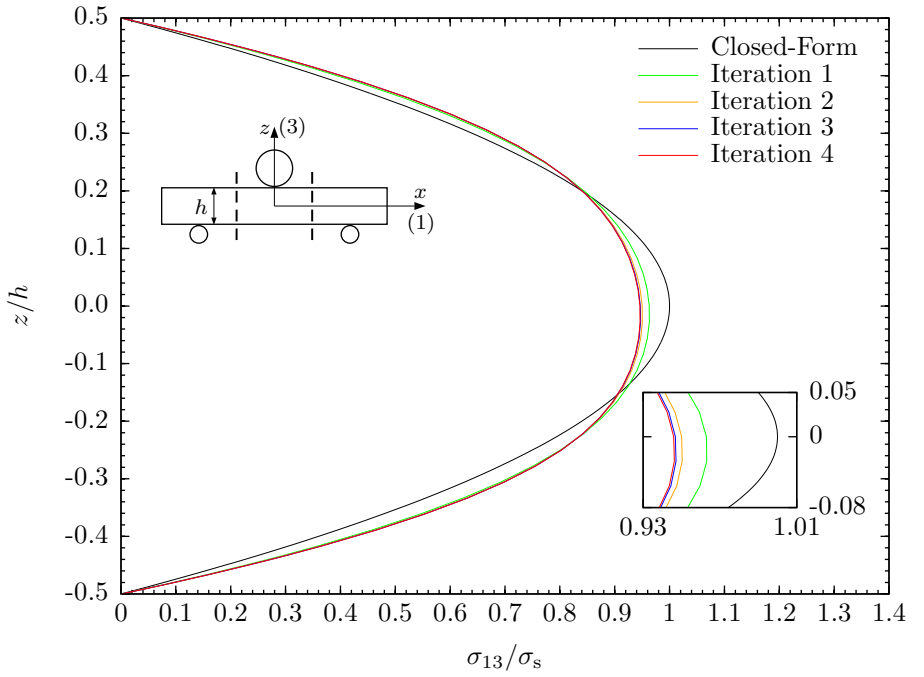

(b)

Figure 6.2: Iterative results of through thickness shear stress and strain distributions for a S2-glass/E773-epoxy tape SBS specimen at 3501 N (787 lbs) 95% failure load in 1-3 material plane (Specimen S3). (a) Shear strain; (b) Shear stress.

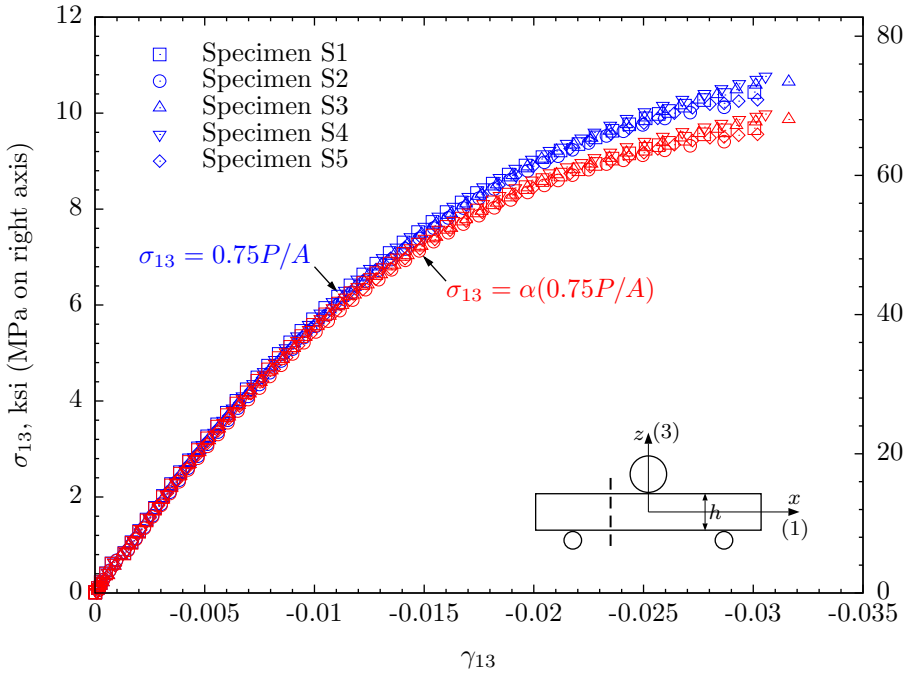

(a)

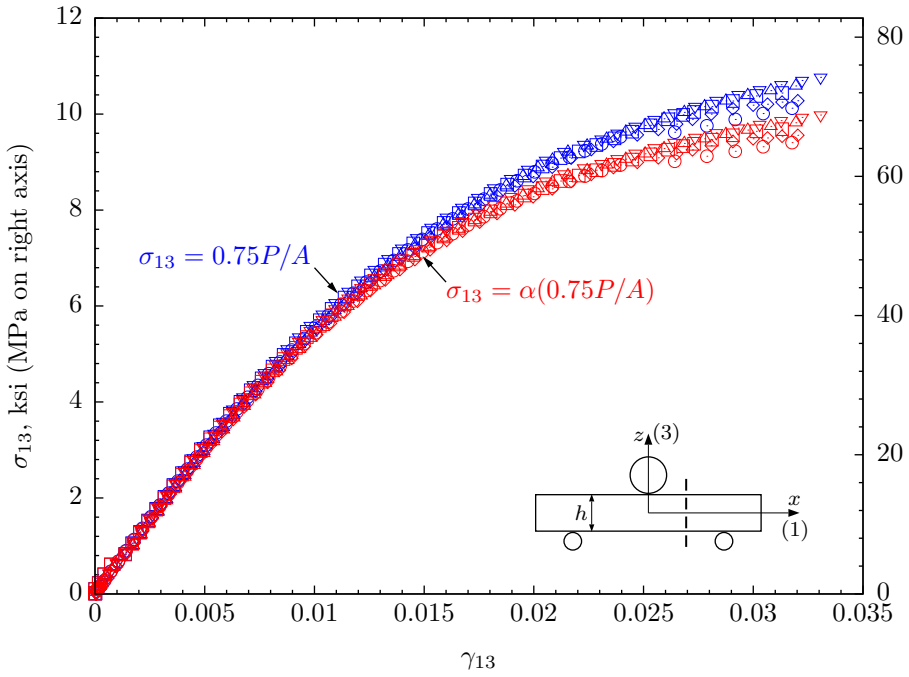

(b)

Figure 6.3: Shear stress-strain response for the S2-glass/E773-epoxy tape SBS specimens in 1-3 material plane. (a) Left section ($x = -L/4$); (b) Right section ($x = L/4$).

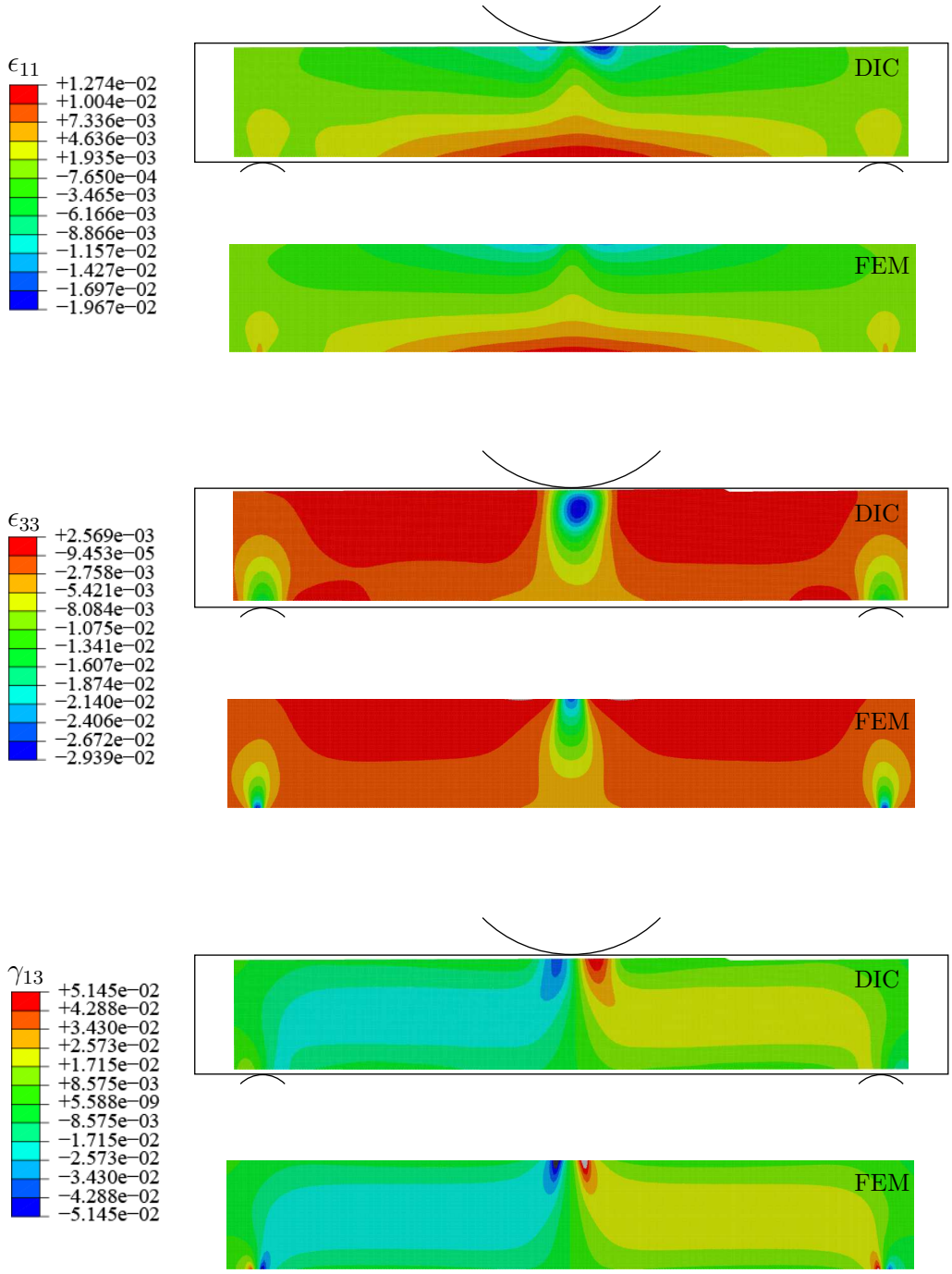

Figure 6.4: Measurement (DIC) and FEM data for surface strain components for a unidirectional S2-glass/E773-epoxy tape SBS specimen at 3501 N (787 lbs) 95% failure load in the 1-3 material plane (Specimen S3).

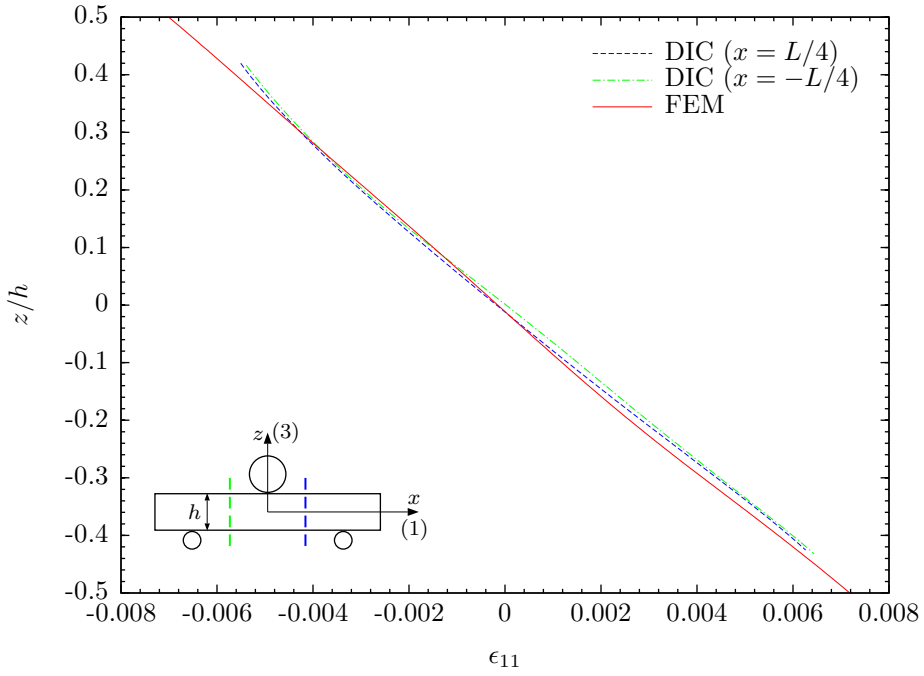

(a)

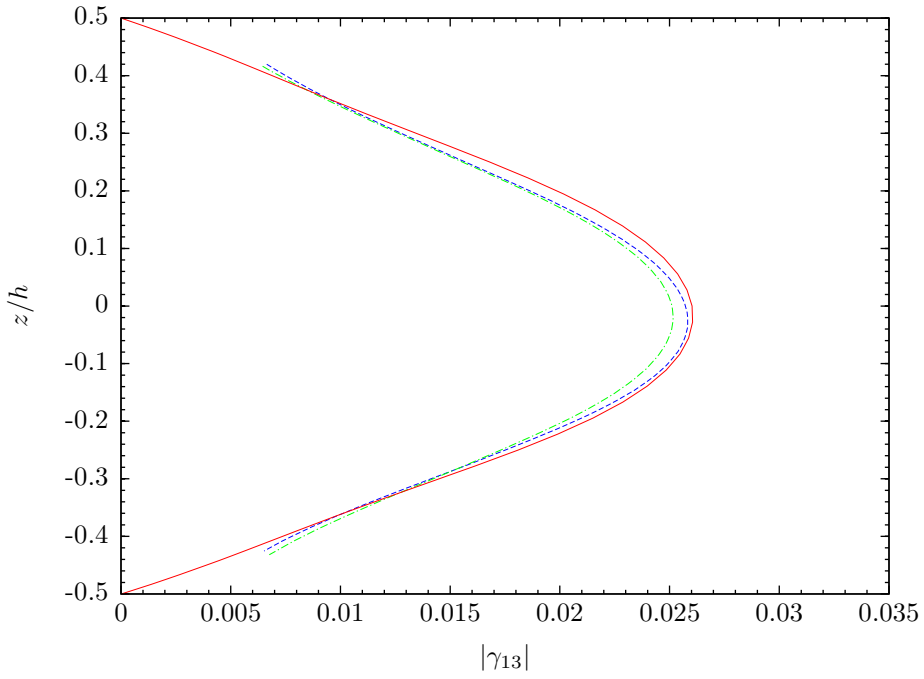

(b)

Figure 6.5: Through thickness strain distributions for a S2-glass/E773-epoxy tape SBS specimen at load 3501 N (787 lbs) 95% failure load in the 1-3 material plane (Specimen S3). (a) Axial strain; (b) Shear strain.

6.1.2 Specimens Loaded in 1-2 and 2-3 Material Planes

The five SBS specimens loaded in the 1-2 material plane were applied by the iterative procedure to update the shear properties listed in Table 3.4 (on Page 36). The numerical results are summarized in Table 6.4.

The iterative results for the Specimen S7 are presented for demonstration purpose. Table 6.5 lists the shear properties updated by the FE-based stresses at each iteration. Figures 6.6(a) and 6.6(b) show the iterative results for the correction factor and the shear stress-strain response respectively. Compared to Figures 6.2(a) and 6.2(b), one can conclude that the iterative procedure follows the the same trend as that in the 1-3 material plane case.

Figures 6.7(a) and 6.7(b) show the updated shear stress-strain response together with the closed-from based response on the left gage section and the right gage section for the five SBS specimens. As shown in Figure 6.8, the finite element predictions for surface components using the updated shear properties are again in good agreement with the experimental results away from the cylinders. The axial and shear distributions through the gage sections are plotted in Figure 6.9. Similar to Figure 6.5, the close agreement between finite element results and DIC measurements is clearly noticed.

As indicated in Table 3.5 (on Page 39), the five specimens loaded in the 2-3 material plane failed early in small strain regime (e.g., $\gamma_{23} < 3000\mu\epsilon$). Therefore only linear shear modulus G_{23} was obtained. As an example of typical results obtained, comparisons of finite element results with DIC measurements for the Specimen S14 were made. The results are shown in Figure 6.10 for surface strain contours and in Figure 6.11 for the strain distributions across the gage sections. It is also seen in these figures that overall there is very good agreement between finite element results and DIC measurements.

Table 6.4: Updated shear properties for the unidirectional S2-glass/E773-epoxy tape SBS specimens in the 1-2 material plane.

Specimen	Initial Values			Updated Values		
	G_{12} GPa (msi)	K_{12} MPa (ksi)	n_{12}	G_{12} GPa (msi)	K_{13} MPa (ksi)	n_{13}
S6	4.07 (0.590)	204 (29.6)	0.230	4.02 (0.583)	178 (25.8)	0.219
S7	4.36 (0.633)	218 (31.6)	0.247	4.39 (0.636)	186 (27.0)	0.235
S8	4.14 (0.600)	216 (31.3)	0.239	4.15 (0.602)	196 (28.5)	0.237
S9	4.33 (0.629)	223 (32.3)	0.250	4.27 (0.619)	186 (26.9)	0.229
S10	4.35 (0.631)	196 (28.5)	0.221	4.34 (0.630)	169 (24.6)	0.209
AVE	4.25 (0.617)	211 (30.7)	0.237	4.23 (0.614)	183 (26.6)	0.226
COV	3.22%	5.13%	5.01%	3.50%	5.50%	5.23%

Table 6.5: Iterative results of shear properties a S2-glass/E773-epoxy tape SBS specimen in the 1-2 material plane (Specimen S7).

	Initial Values	Iteration 1	Iteration 2	Iteration 3	Iteration 4
G_{12} GPa (msi)	4.36 (0.633)	4.39 (0.636)	4.39 (0.636)	4.39 (0.636)	4.39 (0.636)
K_{12} MPa (ksi)	218 (31.6)	193 (27.9)	189 (27.4)	187 (27.1)	186 (27.0)
n_{12}	0.247	0.237	0.237	0.236	0.235

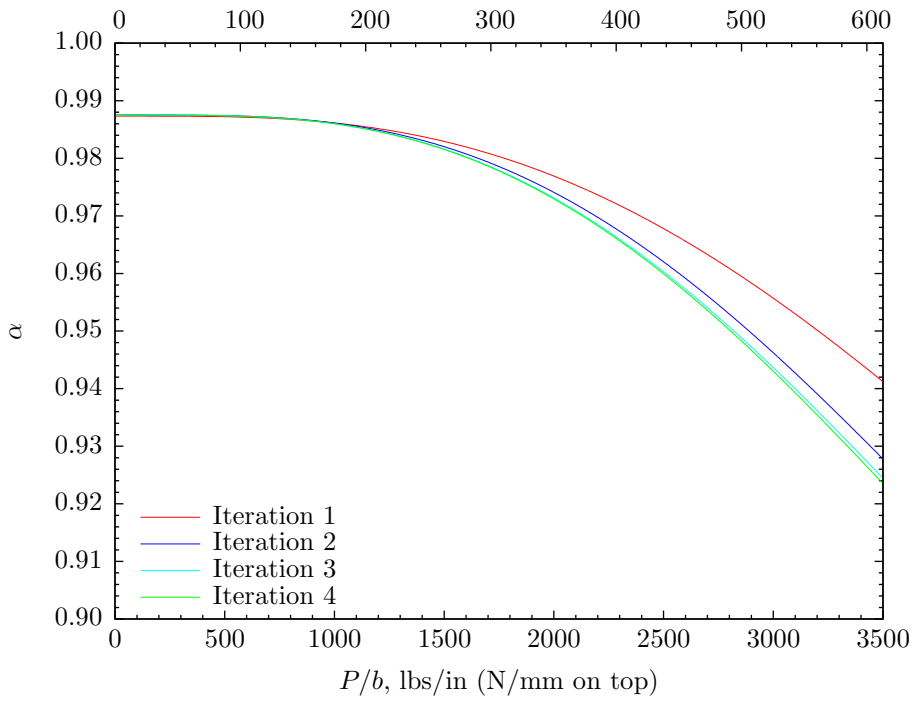

(a)

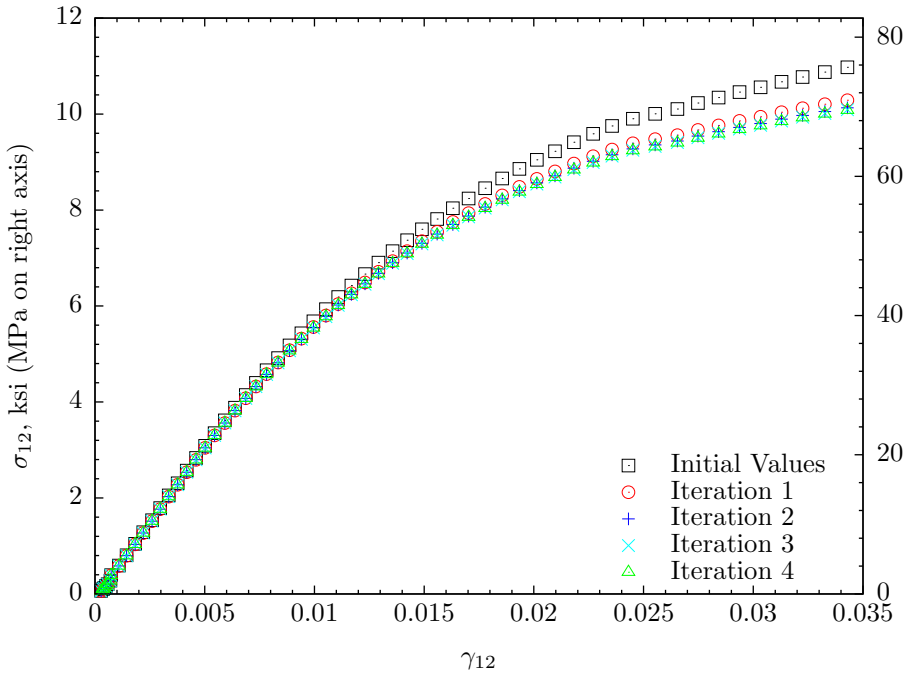

(b)

Figure 6.6: Iterative results for a S2-glass/E773-epoxy tape SBS specimen in the 1-2 material plane (Specimen S7). (a) Correction factor; (b) Shear stress-strain relation.

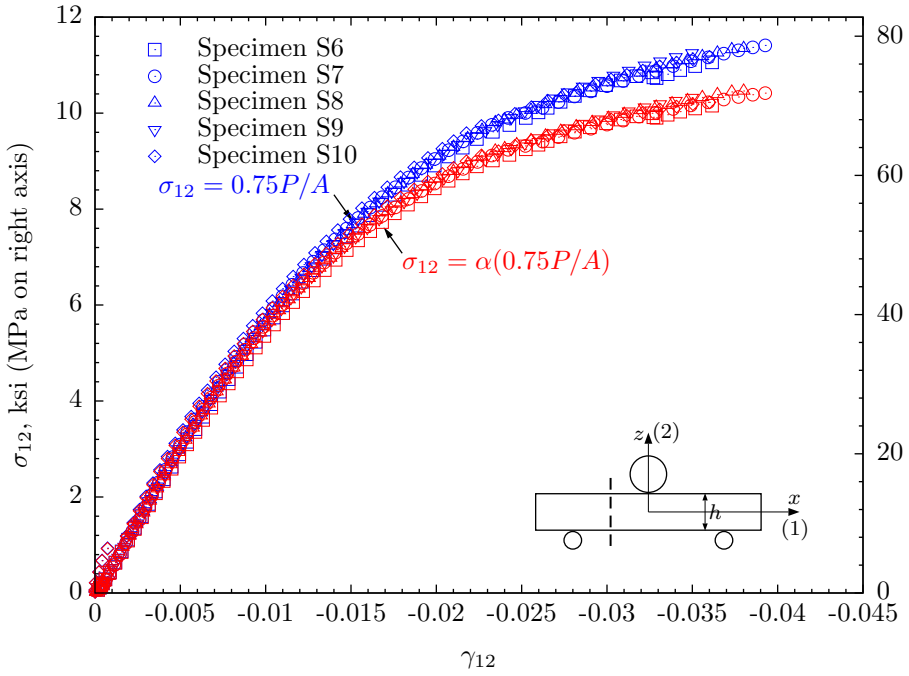

(a)

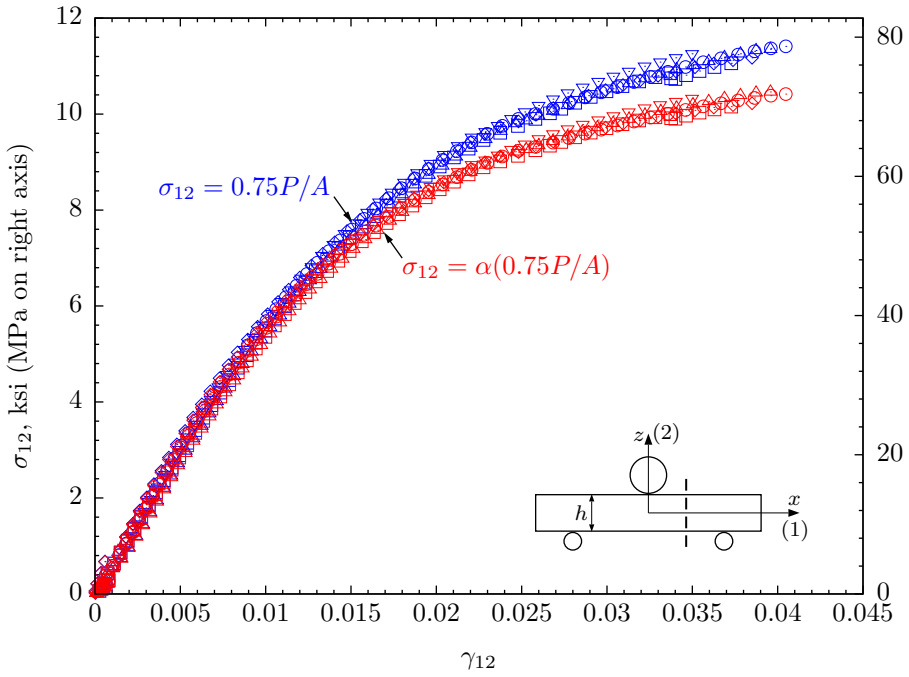

(b)

Figure 6.7: Shear stress-strain response for the S2-glass/E773-epoxy tape SBS specimens in the 1-2 material plane. (a) Left section ($x = -L/4$); (b) Right section ($x = L/4$).

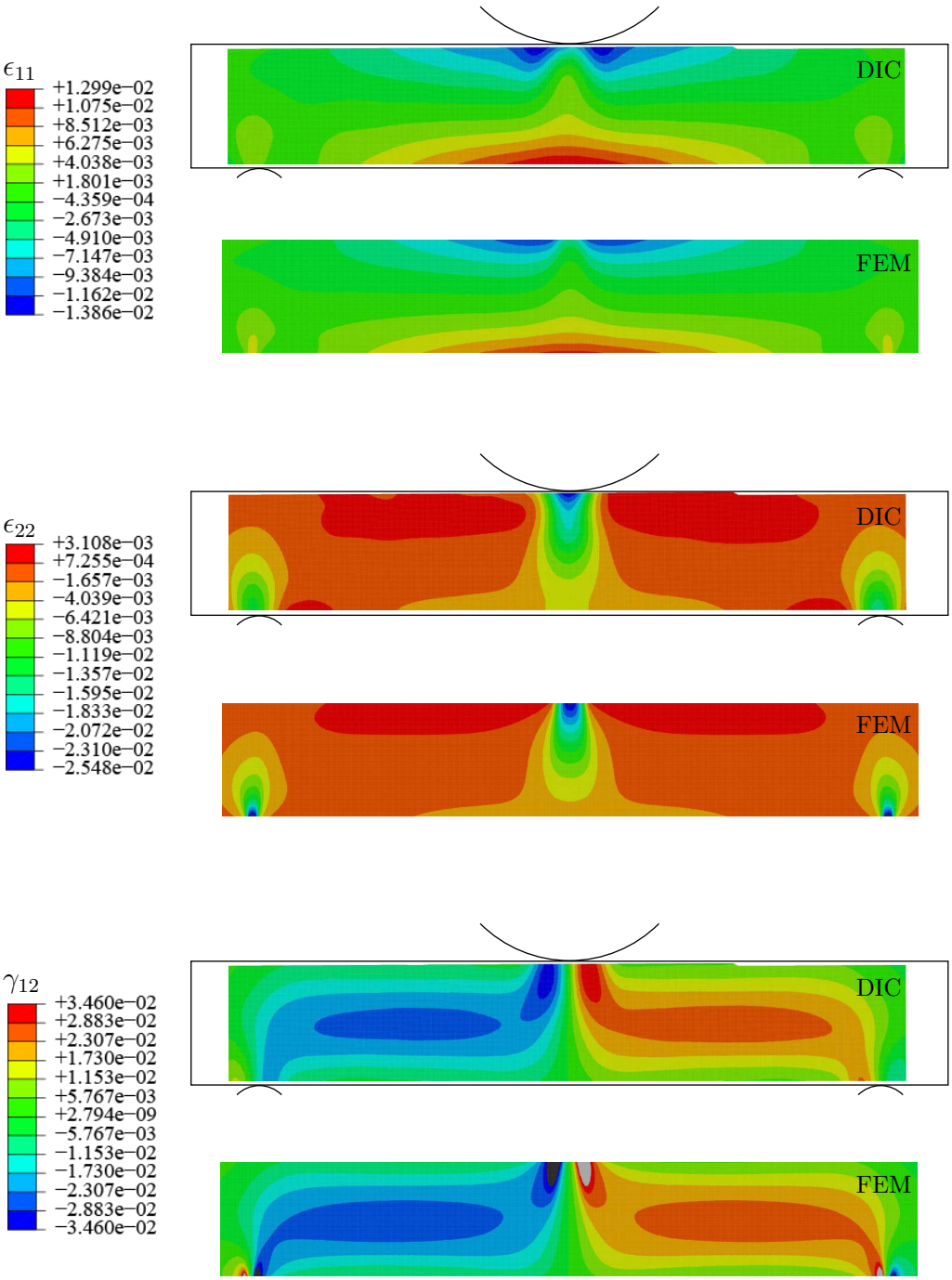

Figure 6.8: Measurement (DIC) and FEM data for surface strain components for a S2-glass/E773-epoxy tape SBS specimen at 3532 N (794 lbs) 90% failure load in the 1-2 material plane (Specimen S7).

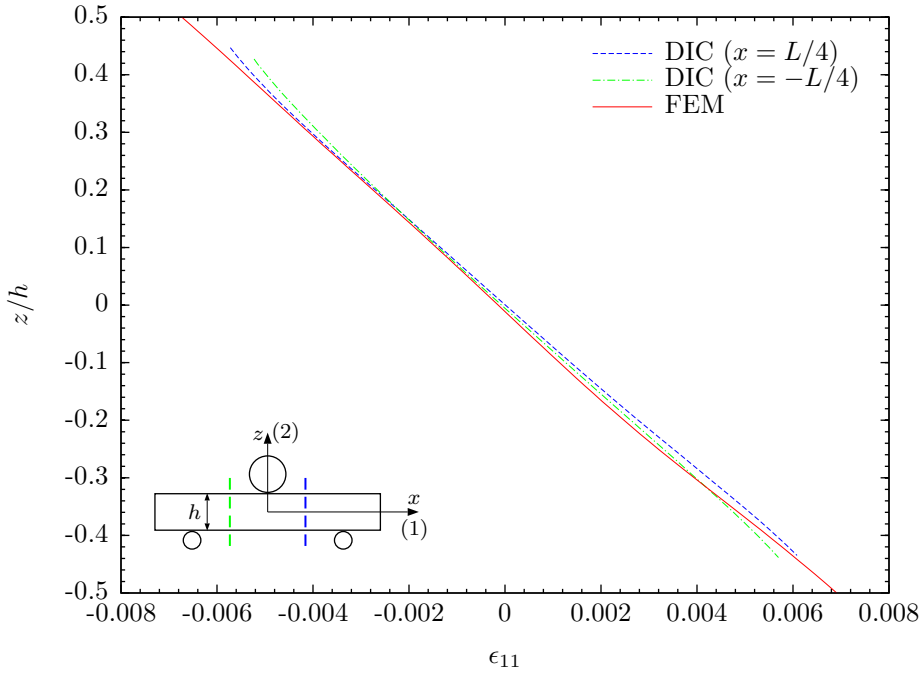

(a)

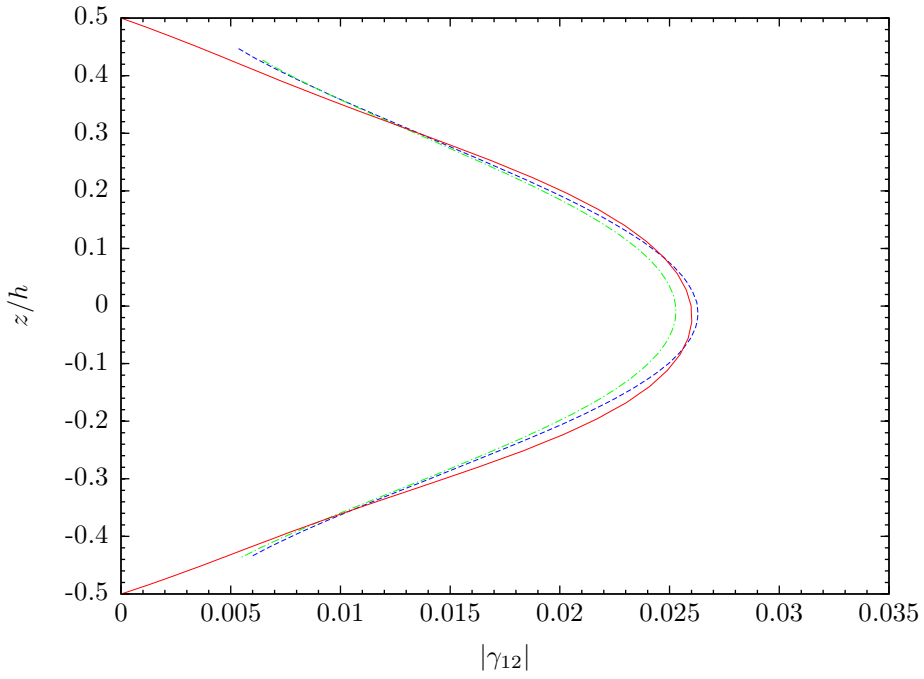

(b)

Figure 6.9: Through thickness strain distributions for a S2-glass/E773-epoxy tape SBS specimen at load 3532 N (794 lbs) 90% failure load in the 1-2 material plane (Specimen S7). (a) Axial strain; (b) Shear strain.

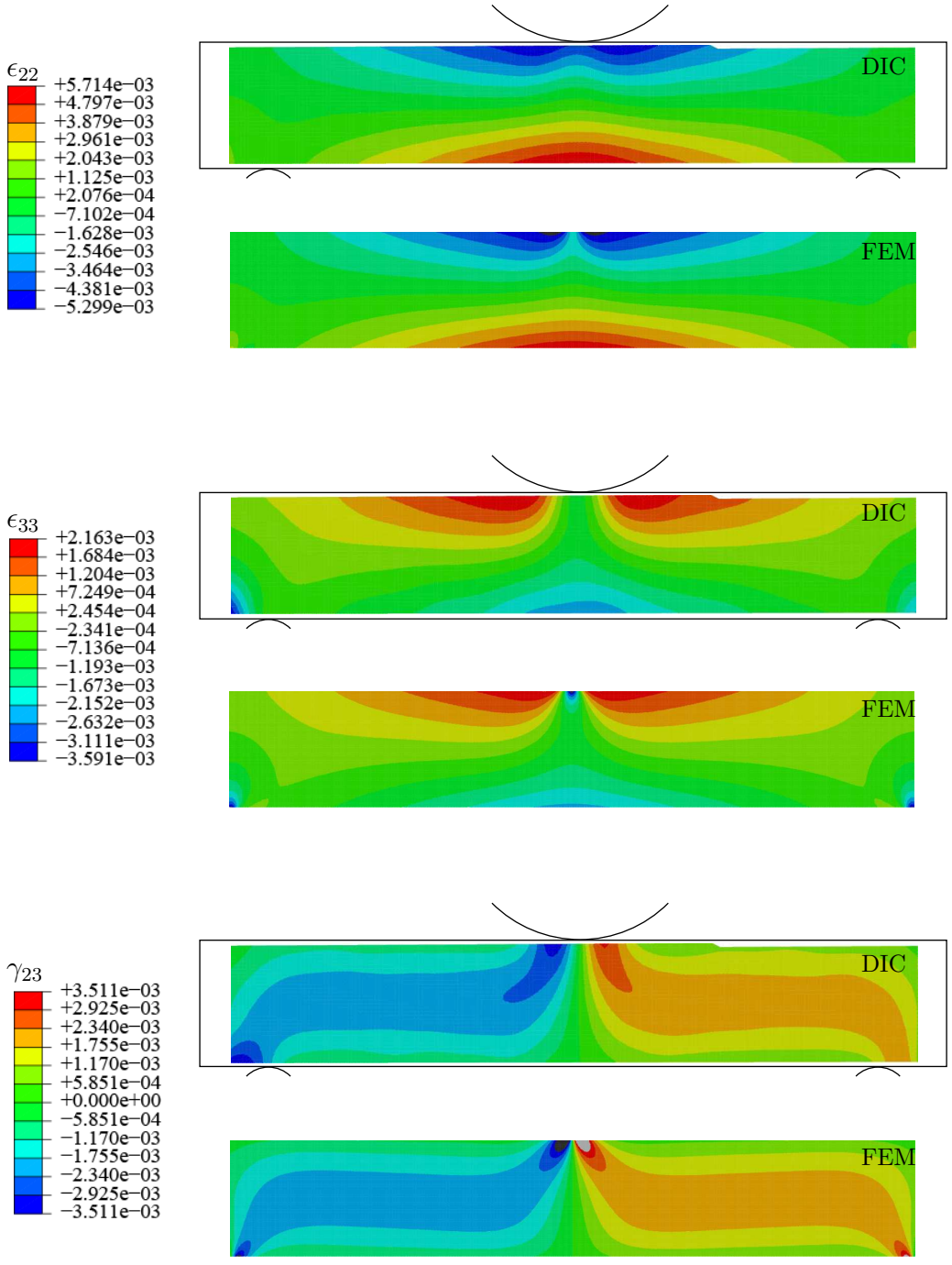

Figure 6.10: Measurement (DIC) and FEM data for surface strain components for a 90° S2-glass/E773-epoxy tape SBS specimen at 458 N (103 lbs) 95% failure load in the 2-3 material plane (Specimen S14).

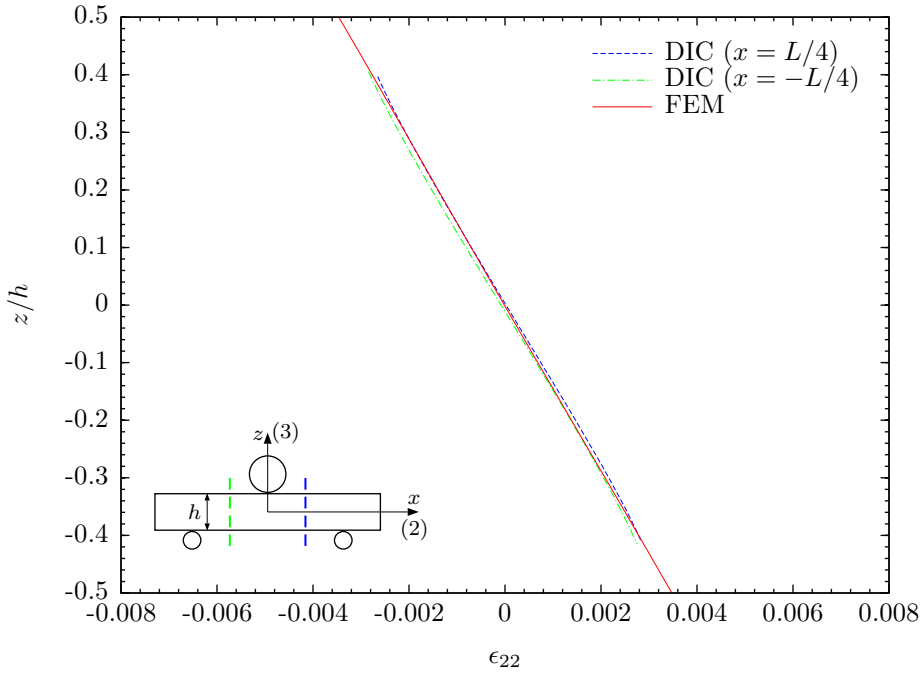

(a)

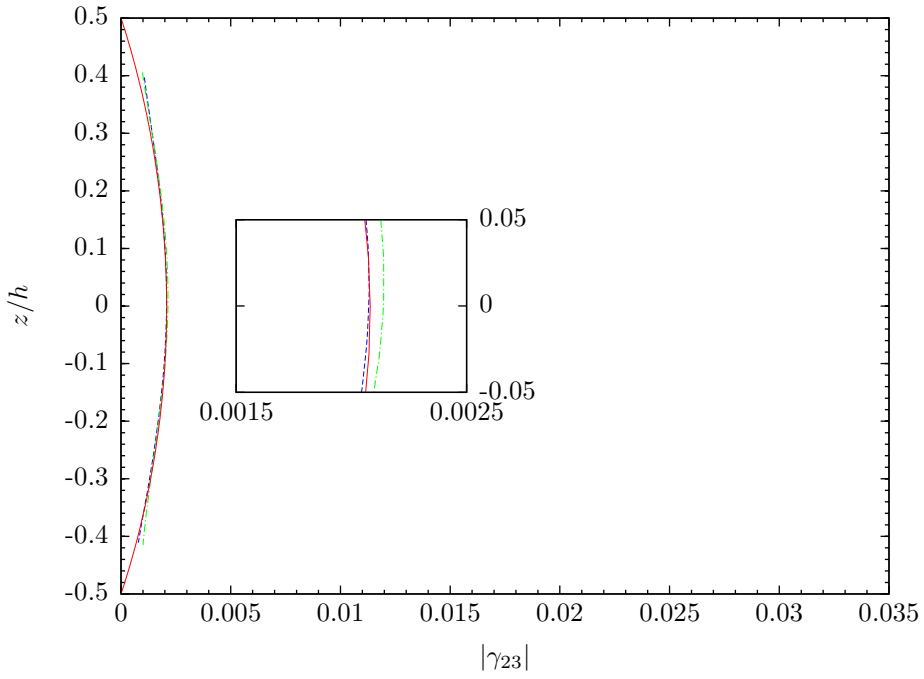

(b)

Figure 6.11: Through thickness strain distributions for a 90° S2-glass/E773-epoxy tape SBS specimen at load 458 N (103 lbs) 95% failure load in the 2-3 material plane (Specimen S14). (a) Axial strain; (b) Shear strain.

6.2 IM7-Carbon/8552-Epoxy SBS Specimens

The iterative procedure was applied to obtain the updated shear properties for the five IM7-carbon/8552-epoxy SBS specimens loaded in the 1-3 material plane. The shear properties summarized in Table 3.8 (on Page 42) were used as initial values in the iterative procedure and the updated properties are presented in Table 6.6. Compared to the results for S2-glass specimens in Tables 6.1 and 6.3, more corrections on the nonlinear parameters (K_{13} and n_{13}) were made due to the large discrepancy of the closed-form approximation (3.9) for the carbon composite specimens. Moreover, slight update on the linear shear stiffness G_{13} was made to account for the discrepancy in small strain region (e.g., $\gamma_{13} < 5000\mu\epsilon$). As a consequence, convergence is slower than the S2-glass case. Five iterations were used in the iterative procedure for each specimen. The fourth-order polynomial (5.6) was applied to fit the correction factor using finite element results.

Detailed numerical results for the Specimen S16 are presented. Table 6.7 summarizes the iterative results of the nonlinear shear properties. Figures 6.12(a) and 6.12(b) show the iterative results for the correction factor and the shear stress-strain relation respectively. In addition to a major update at the first iteration, minor correction can be noticed at the second iteration. Nevertheless, the overall procedure follows the the same trend as that in the S2-glass case.

Figures 6.13(a) and 6.13(b) show the updated shear stress-strain responses together with the closed-from based responses on the left gage section and the right gage section for all the five SBS specimens. The shear stress-strain relations were fitted using a least squares approximation to obtain the initial and updated properties in Table 6.6.

Three-dimensional finite element simulation was conducted using the updated shear properties. The finite element predictions for surface components on beam surface are shown in Figure 6.14 and the strain profiles through the thickness are

shown in Figure 6.15. Good agreement has been achieved between the finite element results and the DIC measurements.

To validate the iterative procedure, the SBS tests are compared with the V-notched beam tests presented in Section 4.3 (on Page 53). Figure 6.16(a) shows the comparison of the V-notched beam shear stress-strain response from all the twelve specimens with the SBS shear stress-strain response generated using the closed-form based stress. Significant deviation can be observed. The SBS shear stress-strain response generated using the FE-based stress are shown in Figure 6.16(b). Excellent agreement is clearly noticed.

Table 6.6: Updated shear properties for the unidirectional IM7-carbon/8552-epoxy tape SBS specimens in the 1-3 material plane.

Specimen	Initial Values			Updated Values		
	G_{13} GPa (msi)	K_{13} MPa (ksi)	n_{13}	G_{13} GPa (msi)	K_{13} MPa (ksi)	n_{13}
S16	5.34 (0.774)	250 (36.2)	0.205	5.11 (0.741)	191 (27.7)	0.189
S17	5.34 (0.774)	233 (33.8)	0.191	5.25 (0.762)	183 (26.6)	0.185
S18	5.51 (0.799)	260 (37.7)	0.215	5.40 (0.783)	188 (27.3)	0.190
S19	5.41 (0.785)	289 (42.0)	0.236	5.38 (0.780)	213 (30.9)	0.218
S20	5.47 (0.794)	258 (37.5)	0.212	5.40 (0.783)	208 (30.2)	0.198
AVE	5.41 (0.785)	258 (37.4)	0.212	5.31 (0.770)	197 (28.5)	0.196
COV	1.44%	7.94%	7.70%	2.38%	6.67%	6.78%

Table 6.7: Iterative results of shear properties for an IM7-carbon/8552-epoxy tape SBS specimen in the 1-3 material plane (Specimen S16).

	Initial Values	Iteration 1	Iteration 2	Iteration 3	Iteration 4	Iteration 5
G_{13} GPa (msi)	5.34 (0.774)	5.13 (0.744)	5.11 (0.741)	5.11 (0.741)	5.11 (0.741)	5.11 (0.741)
K_{13} MPa (ksi)	250 (36.2)	225 (32.6)	202 (29.4)	195 (28.3)	192 (27.9)	191 (27.7)
n_{13}	0.205	0.215	0.199	0.193	0.190	0.189

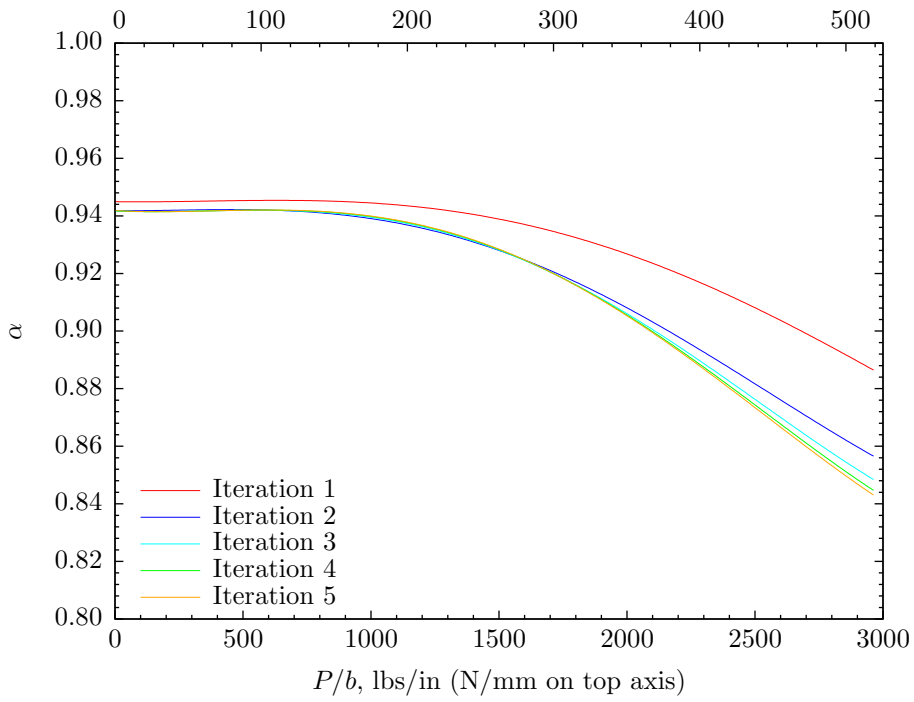

(a)

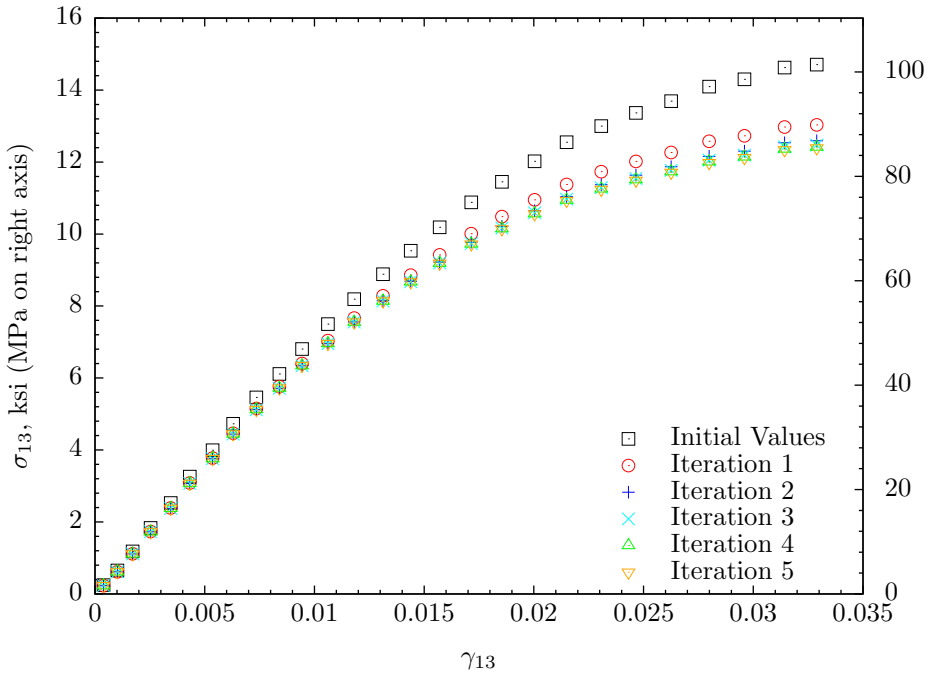

(b)

Figure 6.12: Iterative results for an IM7-carbon/8552-epoxy tape SBS specimen in the 1-3 material plane (Specimen S16). (a) Correction factor; (b) Shear stress-strain relation.

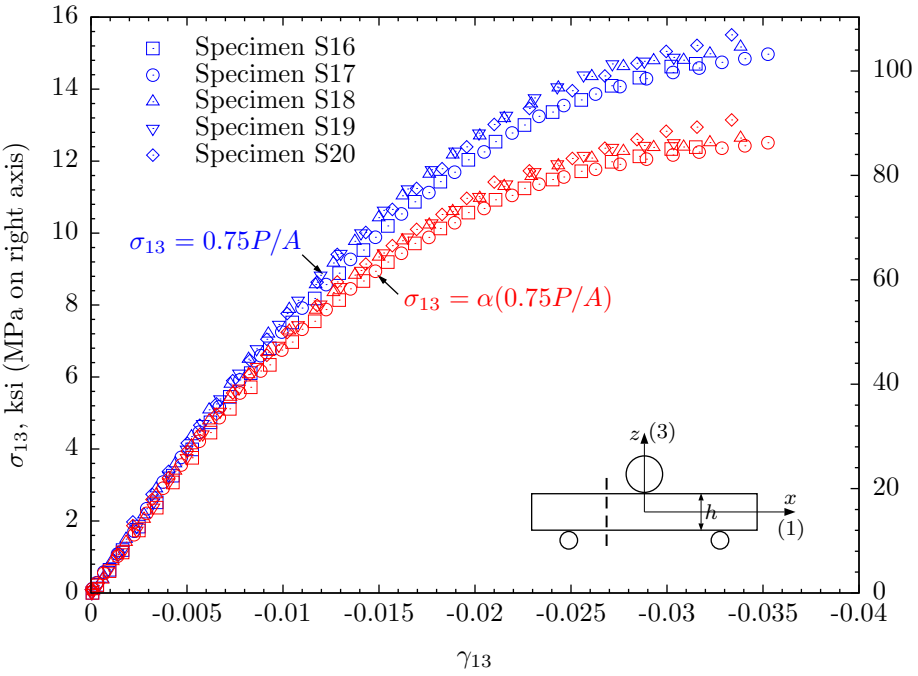

(a)

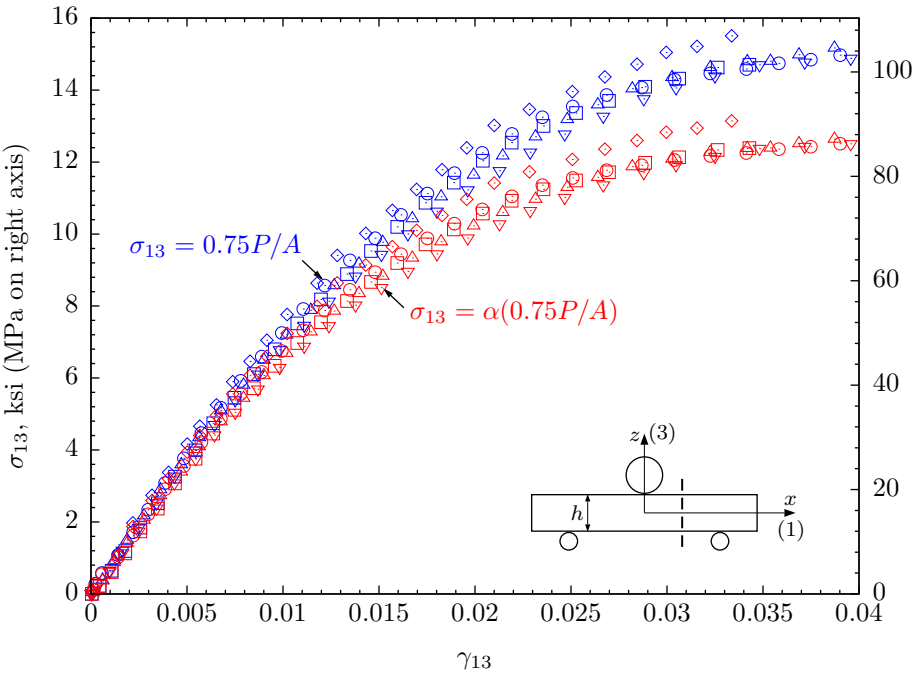

(b)

Figure 6.13: Shear stress-strain response for the IM7-carbon/8552-epoxy tape SBS specimens in the 1-3 material plane. (a) Left section ($x = -L/4$); (b) Right section ($x = L/4$).

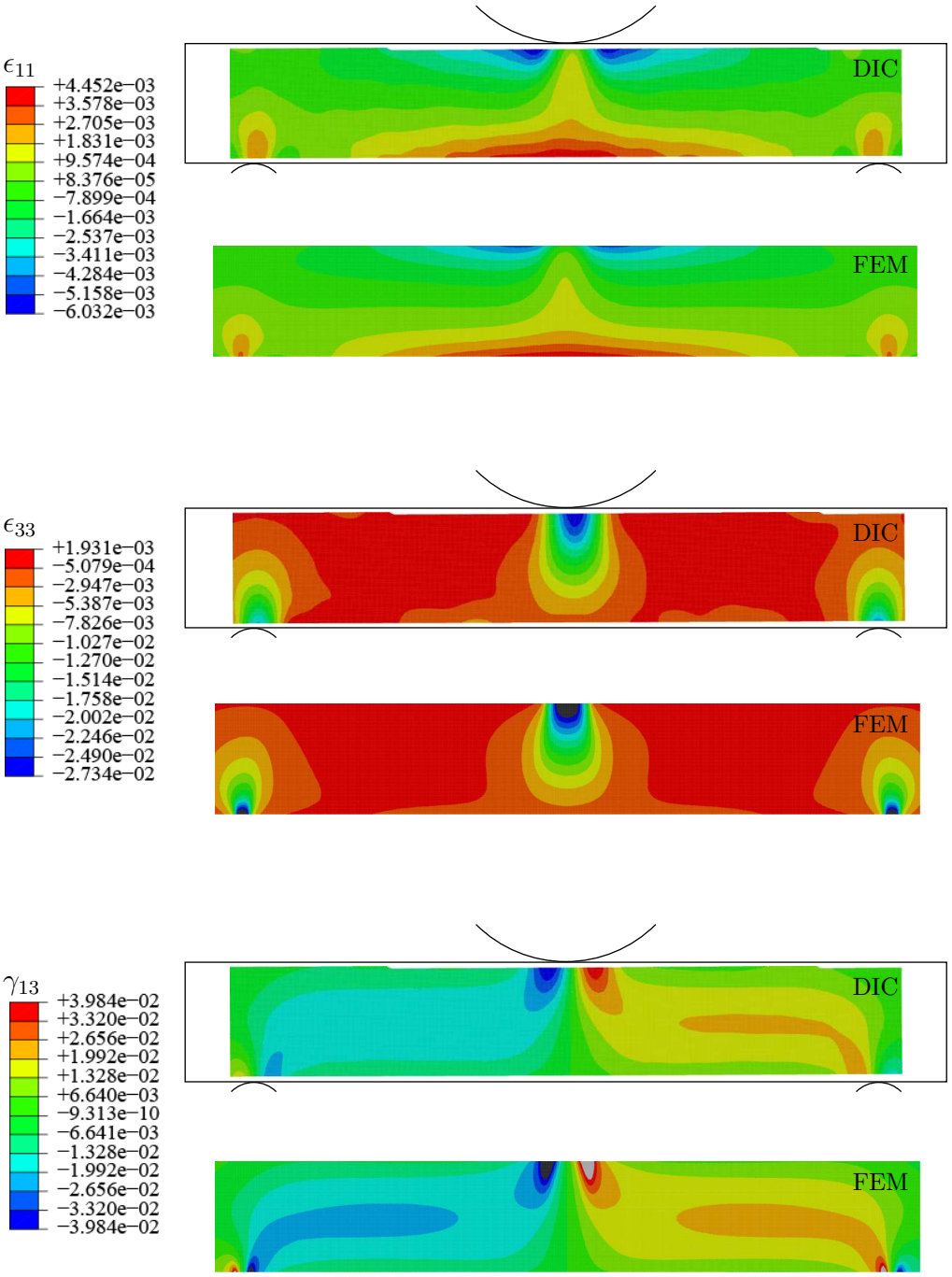

Figure 6.14: Measurement (DIC) and FEM data for surface strain components for an IM7-carbon/8552-epoxy tape SBS specimen at 1312 N (295 lbs) 82% failure load in the 1-3 material plane (Specimen S16).

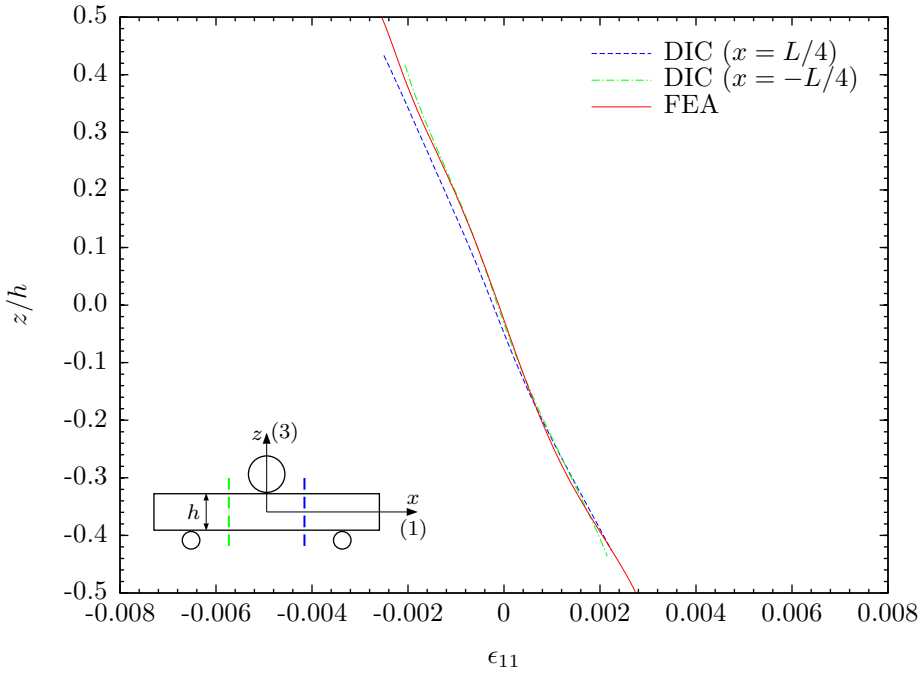

(a)

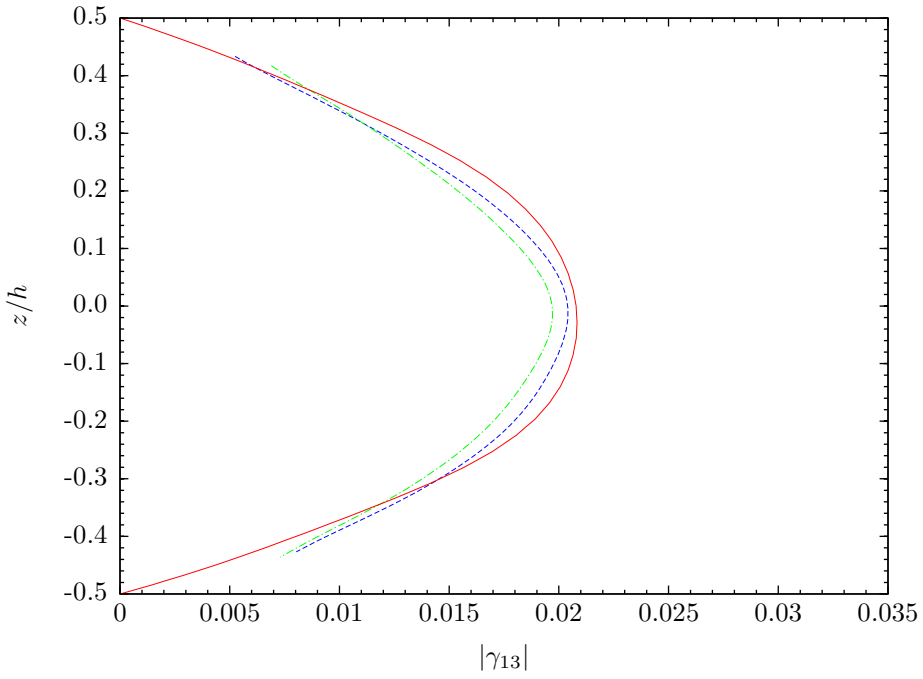

(b)

Figure 6.15: Through thickness strain distributions for an IM7-carbon/8552-epoxy tape SBS specimen at load 1312 N (295 lbs) 82% failure load in the 1-3 material plane (Specimen S16). (a) Axial strain; (b) Shear strain.

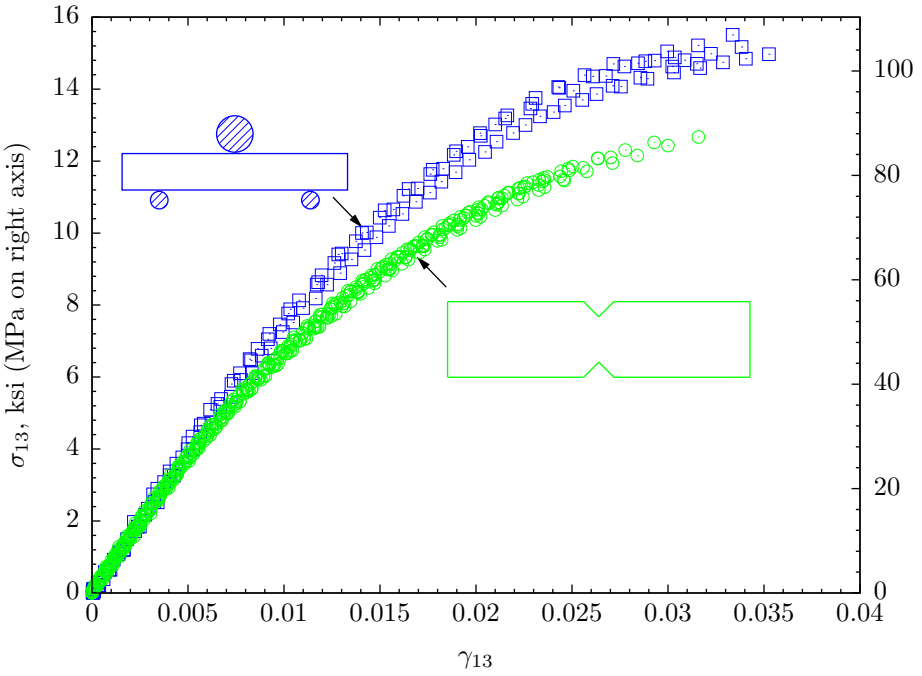

(a)

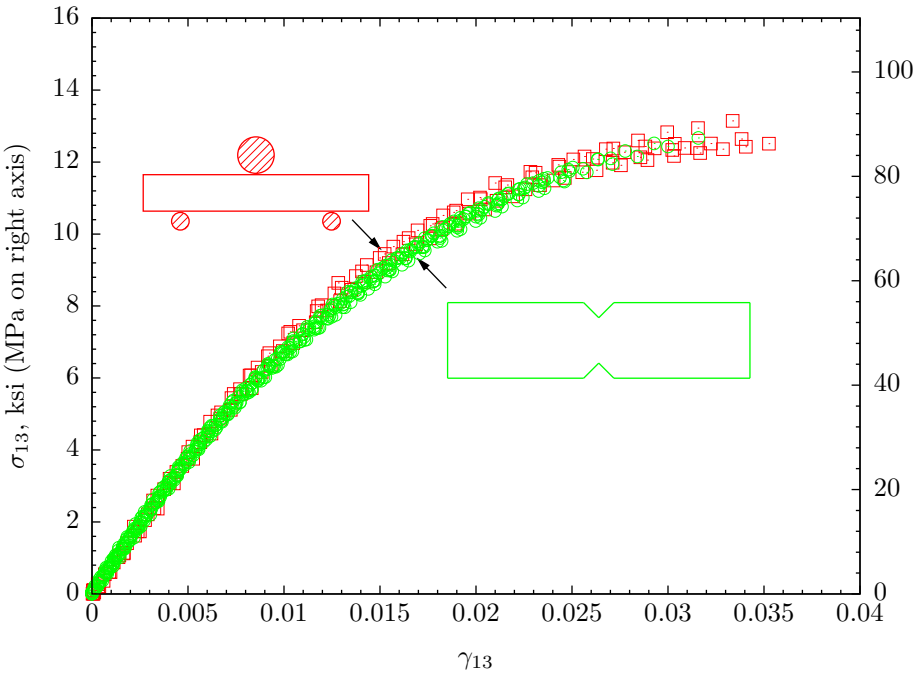

(b)

Figure 6.16: Shear stress-strain response for IM7-carbon/8552-epoxy tape SBS specimens in 1-3 material plane and V-notched beam specimens. (a) SBS shear response generated using closed-form based stress; (b) SBS shear response generated using FE-based stress.

6.3 E-Glass/5216-Epoxy SBS Specimens

The updated shear properties for E-glass/5216-epoxy can be obtained following the same manner as previous studies. The numerical results are tabulated below.

Table 6.8: Updated shear properties for the unidirectional E-glass/5216-epoxy tape SBS specimens in the 1-3 material plane.

Specimen	Initial Values			Updated Values		
	G_{13} GPa (msi)	K_{13} MPa (ksi)	n_{13}	G_{13} GPa (msi)	K_{13} MPa (ksi)	n_{13}
S26	4.51 (0.654)	128 (18.5)	0.147	4.46 (0.646)	97 (14.1)	0.112
S27	4.16 (0.603)	128 (18.6)	0.147	4.10 (0.594)	100 (14.5)	0.116
S28	4.10 (0.595)	130 (18.8)	0.152	4.03 (0.585)	99 (14.4)	0.119
S29	4.04 (0.585)	137 (19.9)	0.168	3.97 (0.576)	100 (14.5)	0.125
S30	4.29 (0.622)	124 (18.0)	0.142	4.23 (0.614)	97 (14.1)	0.111
AVE	4.22 (0.612)	130 (18.8)	0.151	4.16 (0.603)	99 (14.3)	0.117
COV	4.43%	3.74%	6.59%	4.65%	1.34%	4.83%

For demonstration purpose, the numerical results for the Specimen S28 are presented in details. Table 6.9 summarizes the iterative results for nonlinear shear properties at each iteration.

Figures 6.17(a) and 6.17(b) show the iterative results for the correction factor and the shear stress-strain relation respectively. Compared to the iterative results for S2-glass composite specimens shown Figures 6.2(a) and 6.2(b), similar trends in convergence can be observed.

The strain results from three-dimensional finite element simulation using the updated shear properties are compared with the DIC data. Figure 6.18 shows the comparisons for the axial strain (ϵ_{11}), transverse strain (ϵ_{33}), and shear strain (γ_{13})

Table 6.9: Iterative results of shear properties for an E-glass/5216-epoxy tape SBS specimen in the 1-3 material plane (Specimen S28).

	Initial Values	Iteration 1	Iteration 2	Iteration 3	Iteration 4	Iteration 5
G_{13}	4.10	4.04	4.03	4.03	4.03	4.03
GPa (msi)	(0.595)	(0.586)	(0.585)	(0.585)	(0.585)	(0.585)
K_{13}	130	116	108	104	97	99
MPa (ksi)	(18.8)	(16.8)	(15.6)	(15.1)	(14.1)	(14.4)
n_{13}	0.205	0.215	0.199	0.193	0.190	0.189

on the beam surface ($y = -b/2$). Similar to previous examples, the overall agreement is excellent between the finite element results and the DIC data away from supports.

Figure 6.19(a) shows the comparison for the axial strain across the left gage section ($x = -L/2$). The axial strain distribution from DIC measurements agree well with the finite element solution in the center portion of the section, however, deviation from the linear distribution are observed in the region close to the top and bottom edges. The comparison for shear strain distributions are shown in Figure 6.19(b). Satisfactory agreement has obtained between the finite element results and the DIC data. However, deviation from the parabolic distribution were observed in the top and bottom ends.

V-notched beam tests were conducted to verify accuracy of the shear properties for the unidirectional E-glass/5216-epoxy prepreg tape. The experimental procedure are presented in Section 4.3 (on Page 55). Figure 6.20 shows that the V-notched beam shear stress-strain response is similar to SBS stress-strain response generated using the FE-based shear stress approximation. Thus, consistency between SBS test results and V-notched beam test results has been achieved.

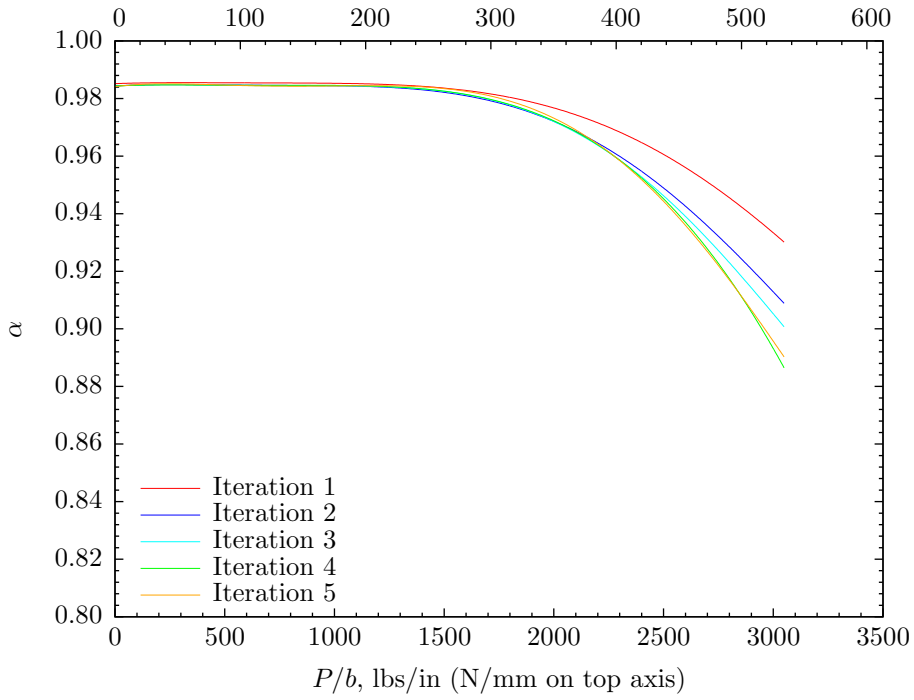

(a)

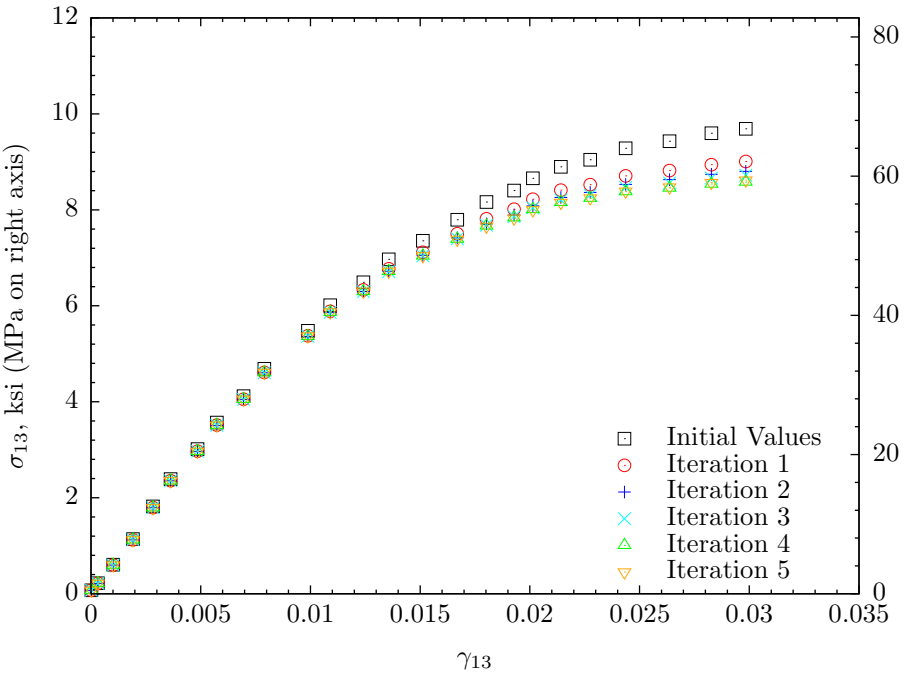

(b)

Figure 6.17: Convergence study for an E-glass/5216-epoxy tape SBS specimen in the 1-3 material plane. (a) Correction factor; (b) Shear stress-strain relation.

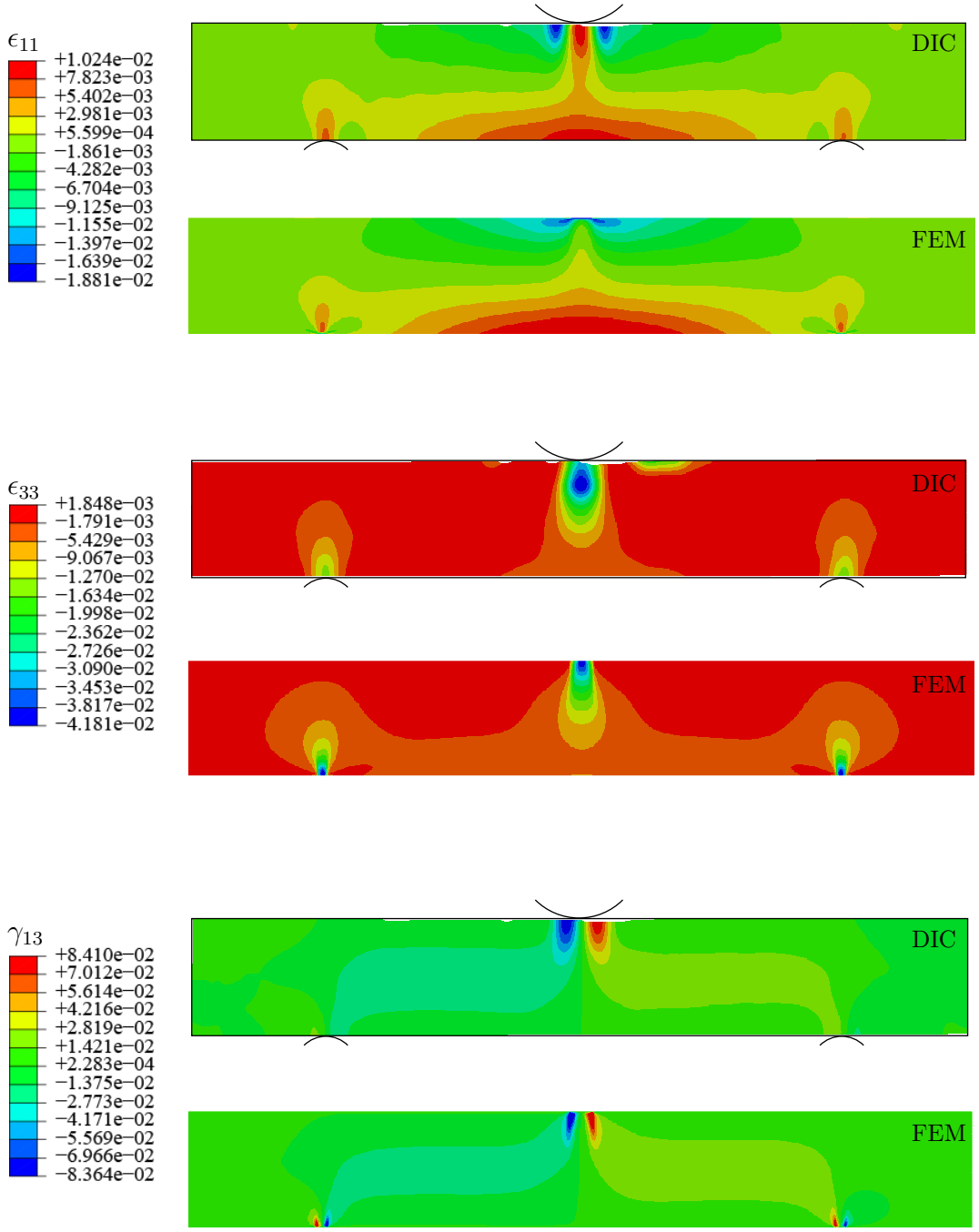

Figure 6.18: Measurement (DIC) and FEM data for surface strain components for an E-glass/5216-epoxy tape SBS specimen at 2153 N (484 lbs) 92% failure load in the 1-3 material plane (Specimen S28).

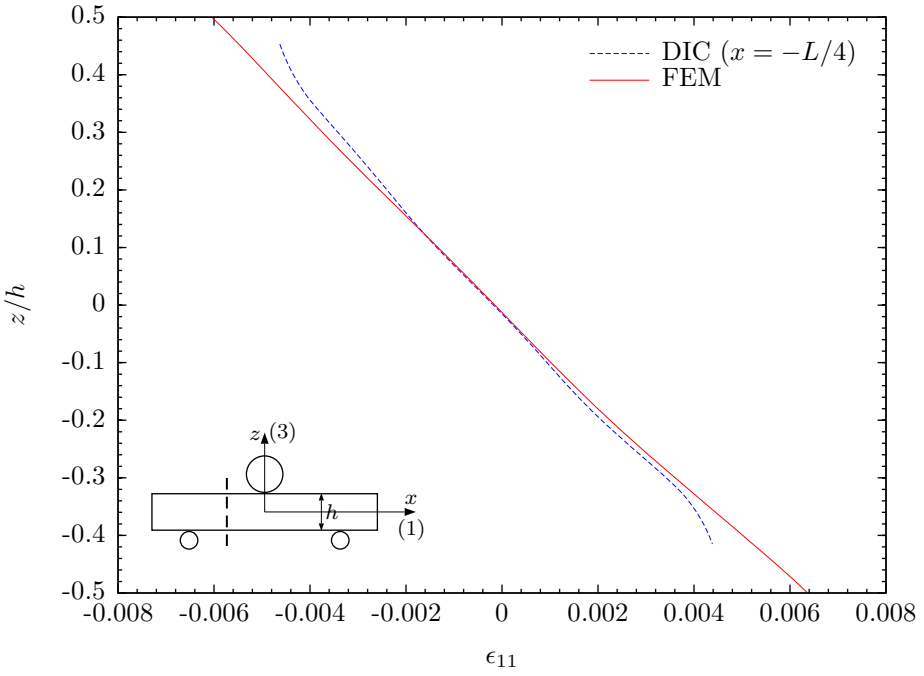

(a)

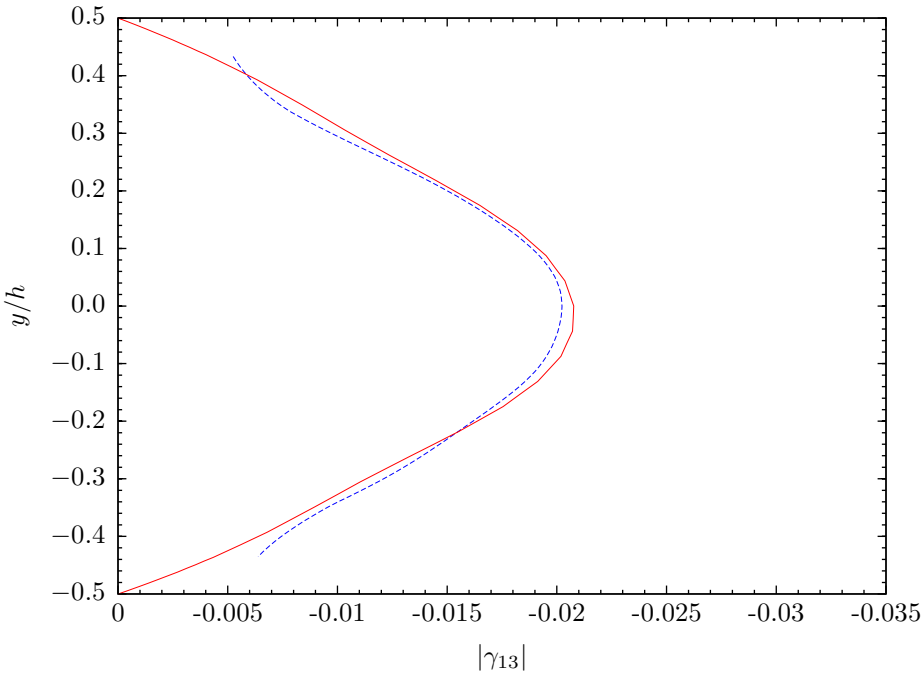

(b)

Figure 6.19: Through thickness strain distributions for an E-glass/5216-epoxy tape SBS specimen at load 2153 N (484 lbs) 92% failure load in the 1-3 material plane (Specimen S28). (a) Axial strain; (b) Shear strain.

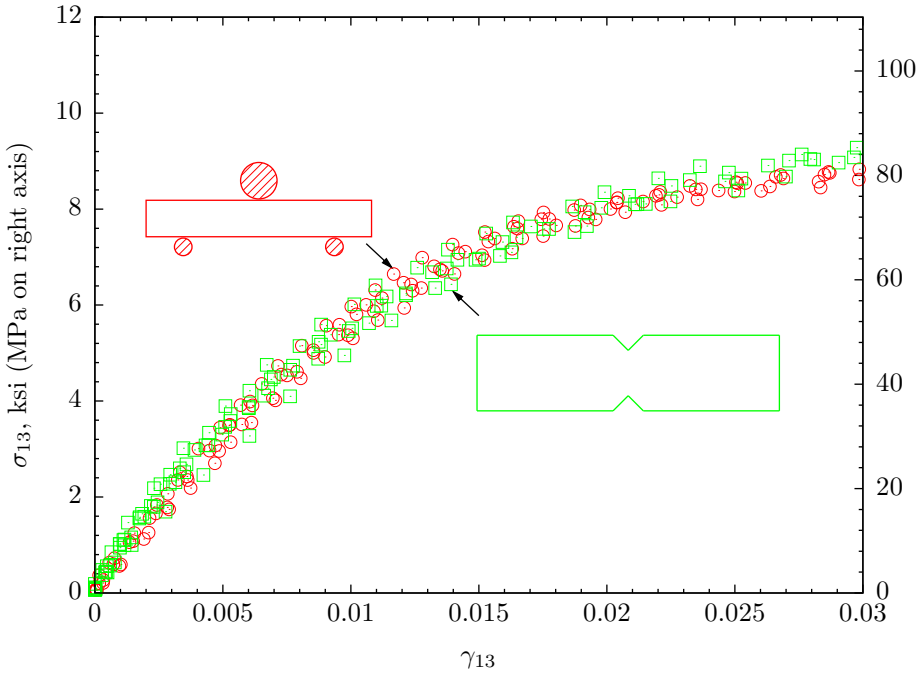

Figure 6.20: Interlaminar shear stress-strain response for unidirectional E-glass/5216-epoxy tape SBS specimens and V-notched beam specimens.

6.4 Laminated SBS Specimens

To further validate the accuracy of updated shear properties for the unidirectional S2-glass/E773-epoxy prepreg tape, two laminated SBS beams were machined from a 24-ply laminated panel with a $[0_4^\circ/(\pm 45^\circ)_4]_s$ layup. The specimens were subjected to three-point bending and loaded in the 1-3 material plane to failure. The specimen dimensions and ultimate failure loads are tabulated below.

Table 6.10: Dimensions and ultimate failure load for the S2-glass/E773-glass laminated beam specimens.

Specimen	L mm (in.)	b mm (in.)	h mm (in.)	F_u N (lbs)
L1	25.4 (1.00)	4.5085 (0.1775)	5.4102 (0.2130)	2415 (543)
L2	25.4 (1.00)	4.4958 (0.1770)	5.4864 (0.2160)	2281 (513)

A three-dimensional nonlinear finite element model was developed to study the axial and shear responses across the gage sections. To reduce the size of the problem and obtain results in realistic CPU time, symmetry conditions were implemented in both span and width directions. Therefore, only a quarter of the specimen was modeled. The second-order elements with reduced integration (i.e., the C3D20R elements in ABAQUS) were used in the model. The finite element mesh is illustrated in Figure 6.21. The mesh is similar to the one used by the homogeneous SBS specimens, except that uniform mesh seeds are employed in the thickness direction. To keep the modeling difficulties low, the model that was developed uses only two elements per ply through the thickness. Therefore, a total of five nodes were employed in a layer. The complete model consists of 20,364 elements and a total of 281,205 variables (degrees of freedoms plus Lagrange multiplier variables) were used in the nonlinear analysis.

The material properties obtained from unidirectional tapes were used in the finite

element model. The numerical results were extracted through the thickness of the gage section ($x = L/4$). The axial and interlaminar shear distributions are presented for Specimen L1.

A closed-form solution is presented in Appendix B for the bending analysis of laminated beam subjected to three-point bending. The derivation is based the classical beam theory and the classical lamination theory. Since the unidirectional S2-glass/E773-epoxy prepreg tape only exhibits slight difference in tensile and compressive Young's moduli, the closed-form solution is also applied here to study through-the-thickness axial and shear responses.

The axial stress distributions σ_x from finite element simulation and the closed-form solution for laminated beam are plotted through the gage section in Figure 6.22(a). The closed-form solution for homogeneous beam, i.e., equation (B.24), is also plotted as a baseline. The stresses displayed in this figure are normalized by the maximum stress σ_{a} from the homogeneous beam solution (B.24). Severe stacking sequence effects on σ_x are clearly evident in the figure. The agreement between finite element simulation and the closed-form solution for laminated beam is satisfactory.

The interlaminar shear stress distributions σ_{xz} from finite element simulation and the closed-form solution for laminated beam are shown in Figure 6.22(b). Again, the distribution of the closed-form solution for homogeneous beam (3.14) is plotted as a baseline. Good agreement between the finite element simulation and the closed-form solution for laminated beam is clearly observed. Consistent with the comparison of axial stress distributions, minor deviation occurs in the angle plies below the middle-surface.

The DIC technique was applied to obtain the full-field strain measurements for the laminated SBS specimens. The results were compared with finite element simulation and the closed-form solution for laminated beam. The axial strain and interlaminar shear strain distributions are plotted through-the-thickness in Figure 6.23(a) and

Figure 6.23(b) respectively. Excellent agreement is clearly indicated in the Figure 6.23(a) for the axial distributions. The strain distributions remain linearly through the thickness. As shown in Figure 6.23(b), good agreement has been achieved in the center portion of the thickness for the shear strain distributions.

Although not presented herein, similar observations were made from the L2 specimen. The good correlation between strain measurements and finite element results indicates that the material properties obtained from the unidirectional tapes can be used with confidence in the engineering practice. It is also noted that, due to the relatively coarse mesh in the width and thickness directions, no interlaminar singularity was observed in the finite element simulation. Furthermore, stress discontinuity may occur across the ply interfaces since the finite element analysis is displacement based.

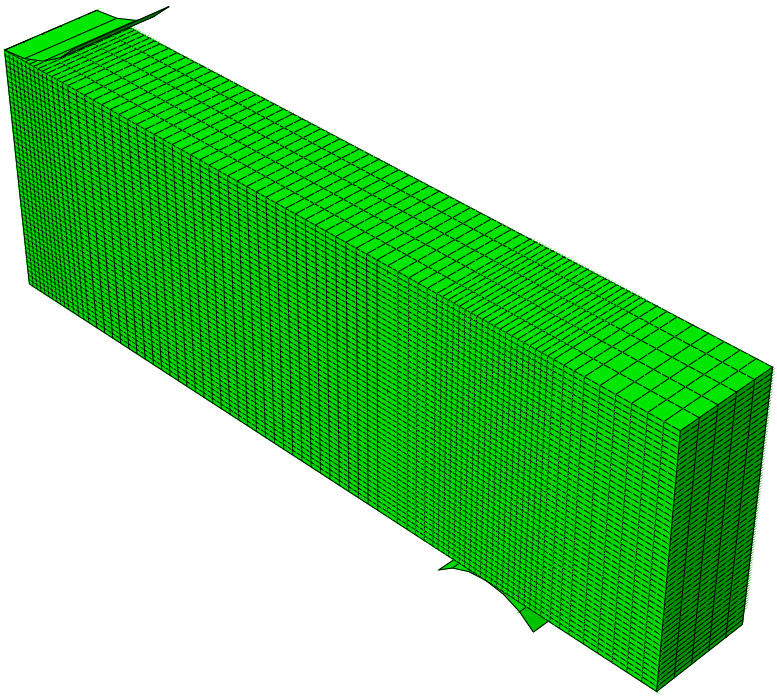

(a)

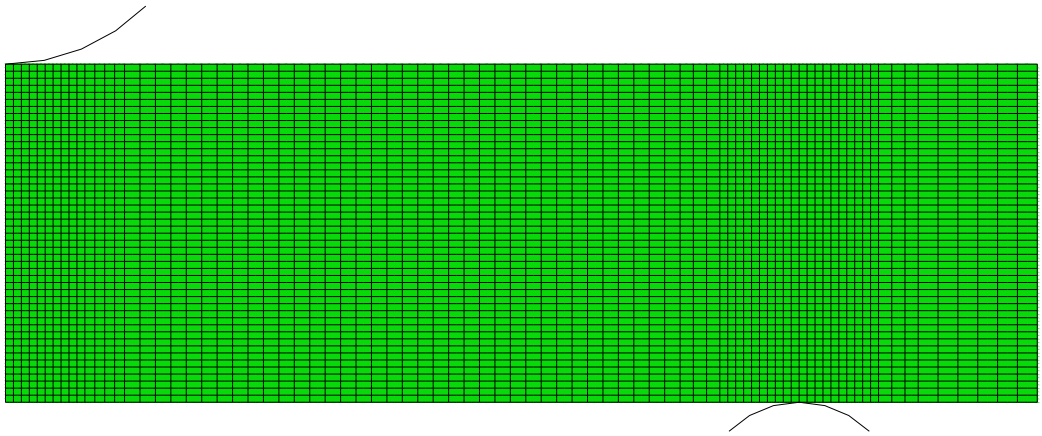

(b)

Figure 6.21: Finite element mesh of the laminated SBS specimens. (a) Three-dimensional view; (b) x-z plane view.

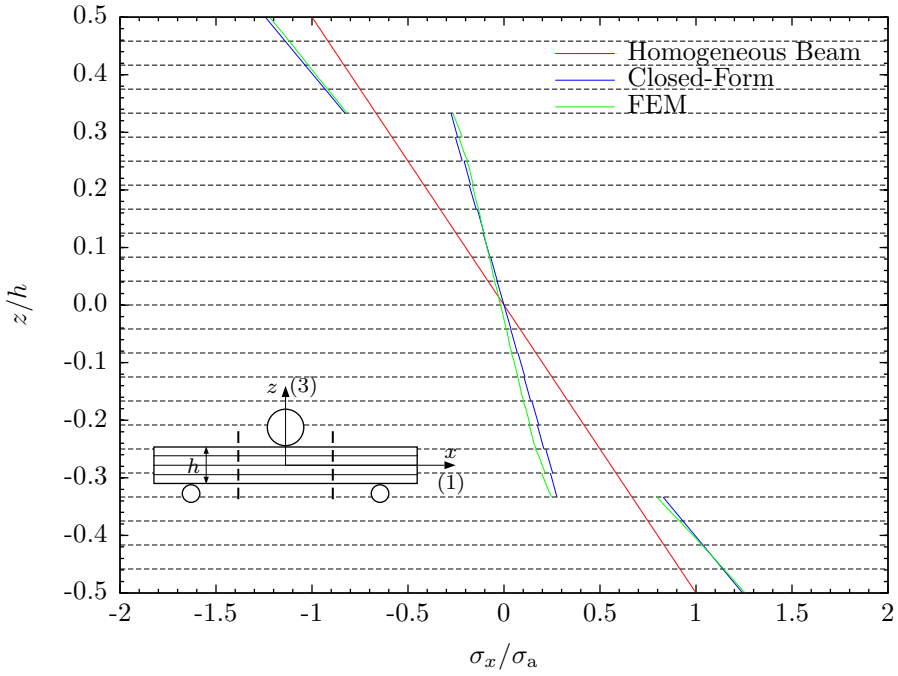

(a)

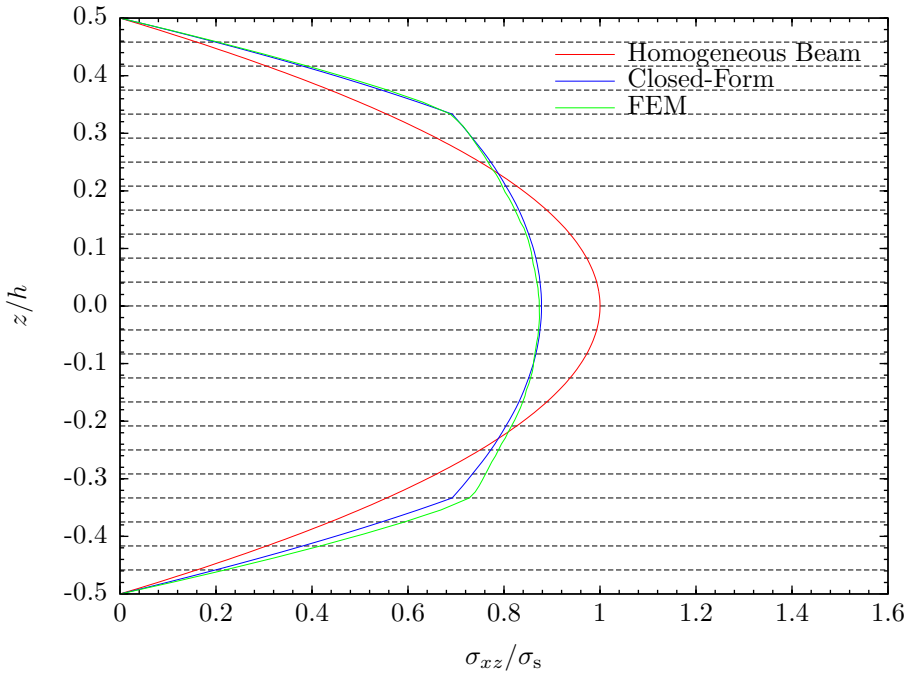

(b)

Figure 6.22: Through thickness stress distributions for a laminated S2-glass/E773-epoxy SBS specimen at 1690 N (380 lbs) 70% failure load (Specimen L1). (a) Axial stress; (b) Shear stress.

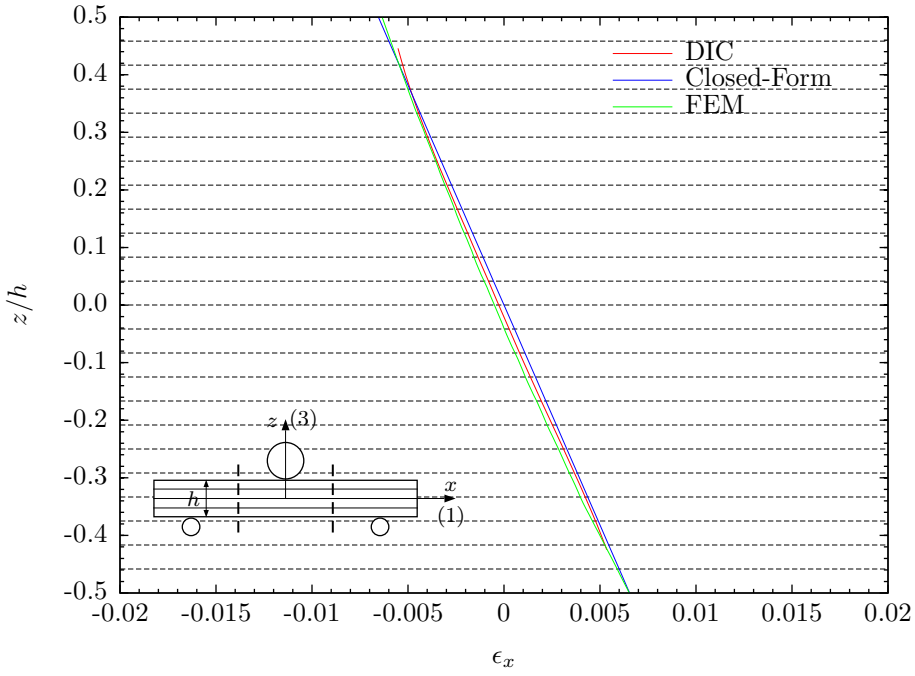

(a)

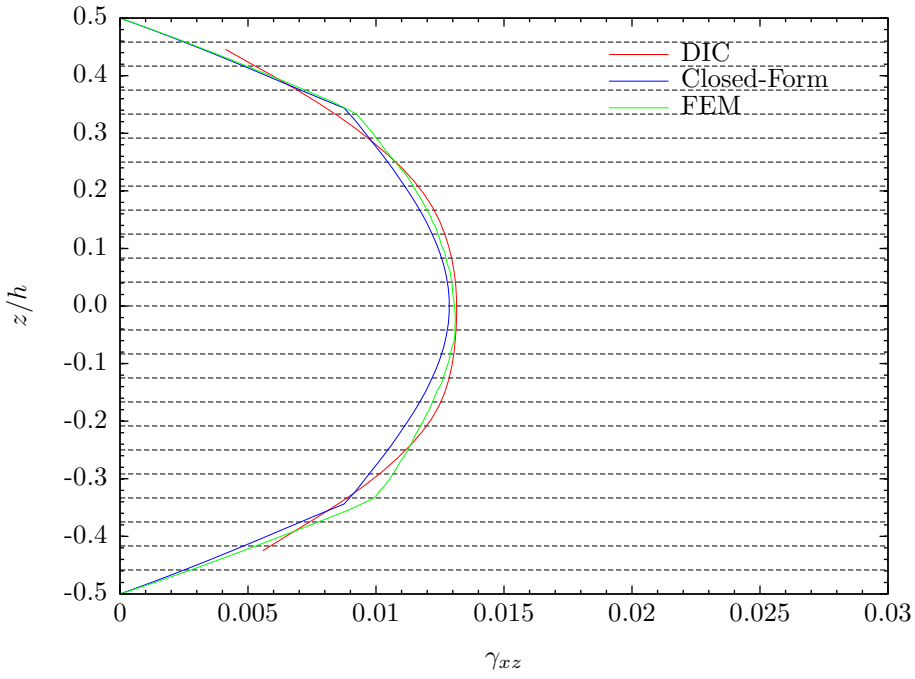

(b)

Figure 6.23: Through thickness strain distributions for a laminated S2-glass/E773-epoxy SBS specimen at 1690 N (380 lbs) 70% failure load (Specimen L1). (a) Axial strain; (b) Shear strain.

6.5 Specimens with Wavy Plies

Ply (or fiber) waviness is a major issue for thick composite applications [25]. Ply waviness has been demonstrated experimentally, numerically and analytically to significantly reduce the structural performance [6, 7]. Experimental studies also shown the ply waviness can significantly reduce fatigue life and change failure behavior [7,43]. The importance of shear material nonlinearity in wavy ply analysis has also been recognized. In addition, interlaminar shear has been identified as at least one dominate failure mechanism associated with ply waviness [6, 43].

6.5.1 Unidirectional E-Glass/5216-Epoxy Tape Wrinkle Specimens

The updated shear properties for unidirectional E-glass/5216-epoxy tape were implemented in finite element analysis to study the interlaminar shear stress-strain responses of unidirectional wrinkle specimens.

Figure 6.25 shows the procedure for wrinkle specimen development from the unidirectional E-glass/5216-epoxy tape. The wrinkle specimens were made by laying up and curing E-glass/5216-epoxy prepreg tape over "speed bump". As illustrated in the figure, two wrinkle laminates along with a straight laminate are combined and cast in EA9396 resin in order to bond the laminates together and to fill the space under the wrinkles. The tension specimens are made by wafering 1.90 mm (0.075 inches) thick slices from the edge of the laminate.

Following the ASTM standard test method for tensile properties [9], the wrinkle specimens were statically loaded to failure in the transverse (1-3) material direction. Interlaminar shear failure was observed.

As shown in Figure 6.27, a two-dimensional finite element model was built to perform stress analysis for a wrinkle specimen. The specimen thickness is 1.88 mm (0.074 inches); width is 34.95 mm (1.376 inches); and gage (untabbed) length is 152.4 mm (6.0 inches). Plane stress is assumed since the specimen thickness is much

smaller than other dimensions. The model has a total of 8,081 second-order plane stress elements (i.e., CPS8R elements) and a total of 49,273 degrees of freedom. The updated shear properties listed in Table 6.8 were implemented in the model. The specimen is loaded in tension in the length direction. The contour plots for three strain components (i.e., ϵ_{11}, ϵ_{33} and γ_{13}) are shown in Figure 6.26 in conjugation with the DIC data. Figure 6.27 shows the comparison of DIC and FEM data for shear strain component (γ_{13}) at various load magnitudes. Good agreement between finite element results and DIC data can be observed, especially for the shear strain component, which is particularly important for the shear failure mode.

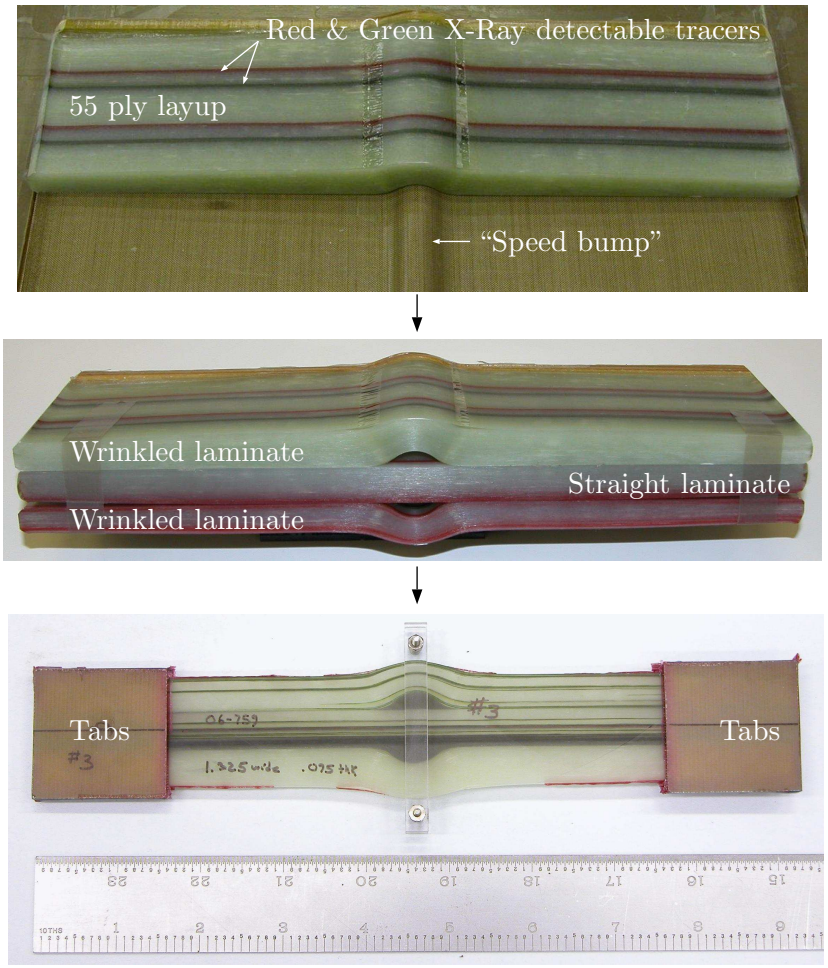

Figure 6.24: E-glass/5216-epoxy wrinkle specimen development.

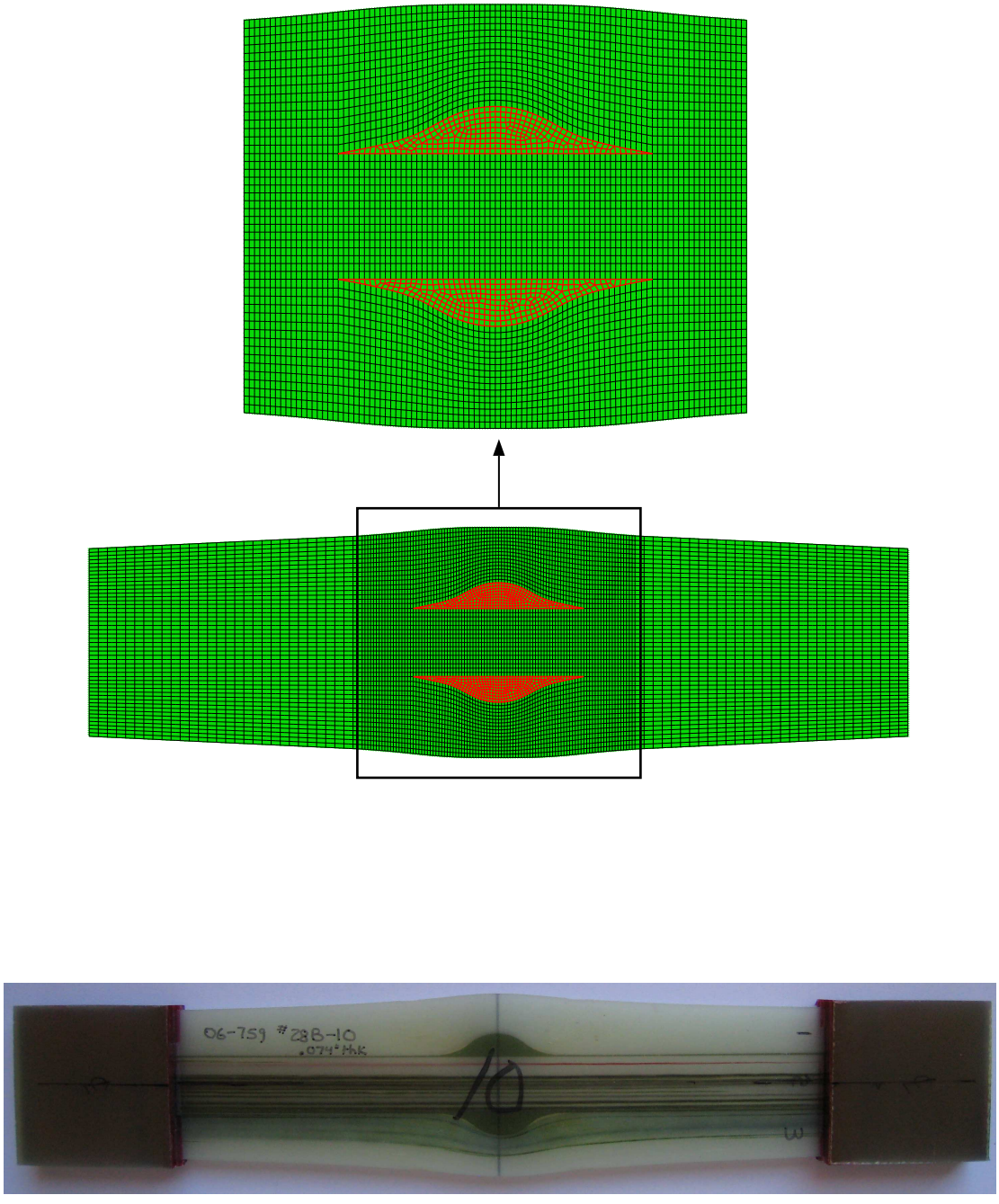

Figure 6.25: Finite element mesh of a unidirectional E-glass/8552-epoxy wrinkle specimen.

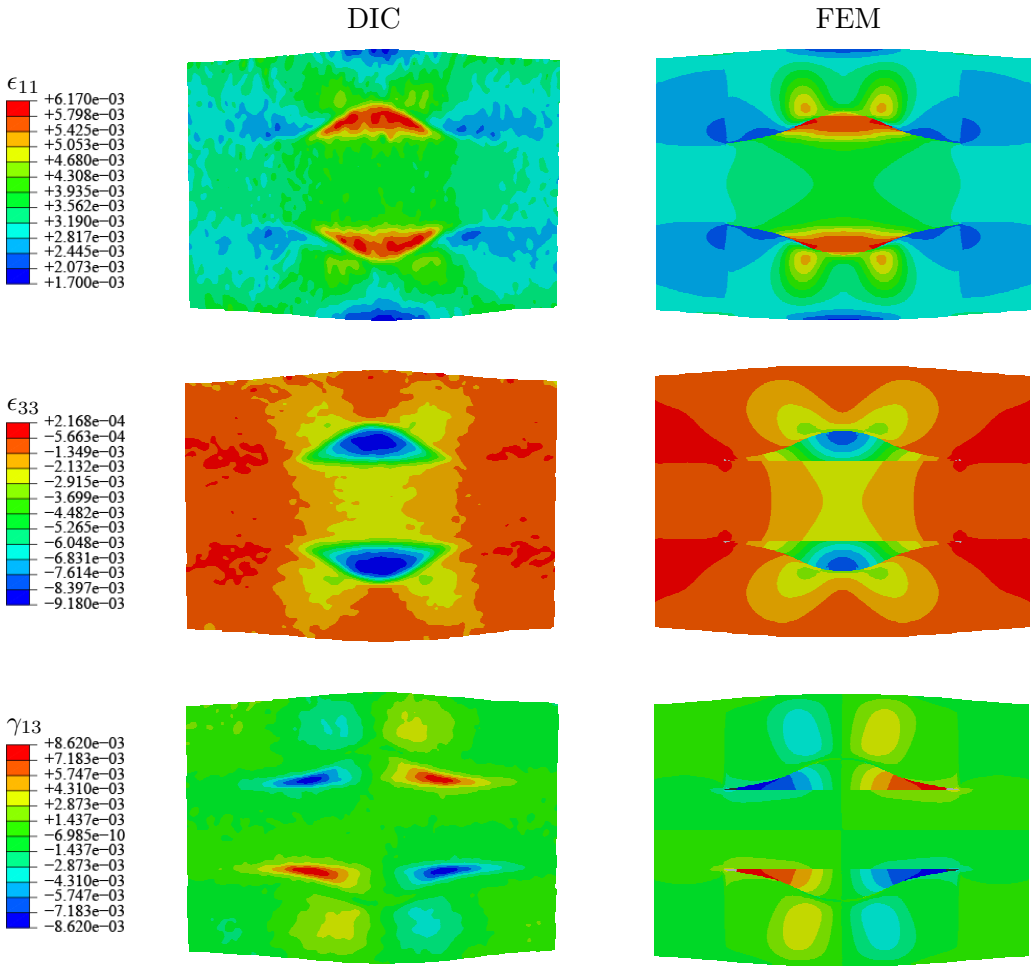

Figure 6.26: Measurement and FEM data for surface strain components for a unidirectional E-glass/8552-epoxy wrinkle specimen.

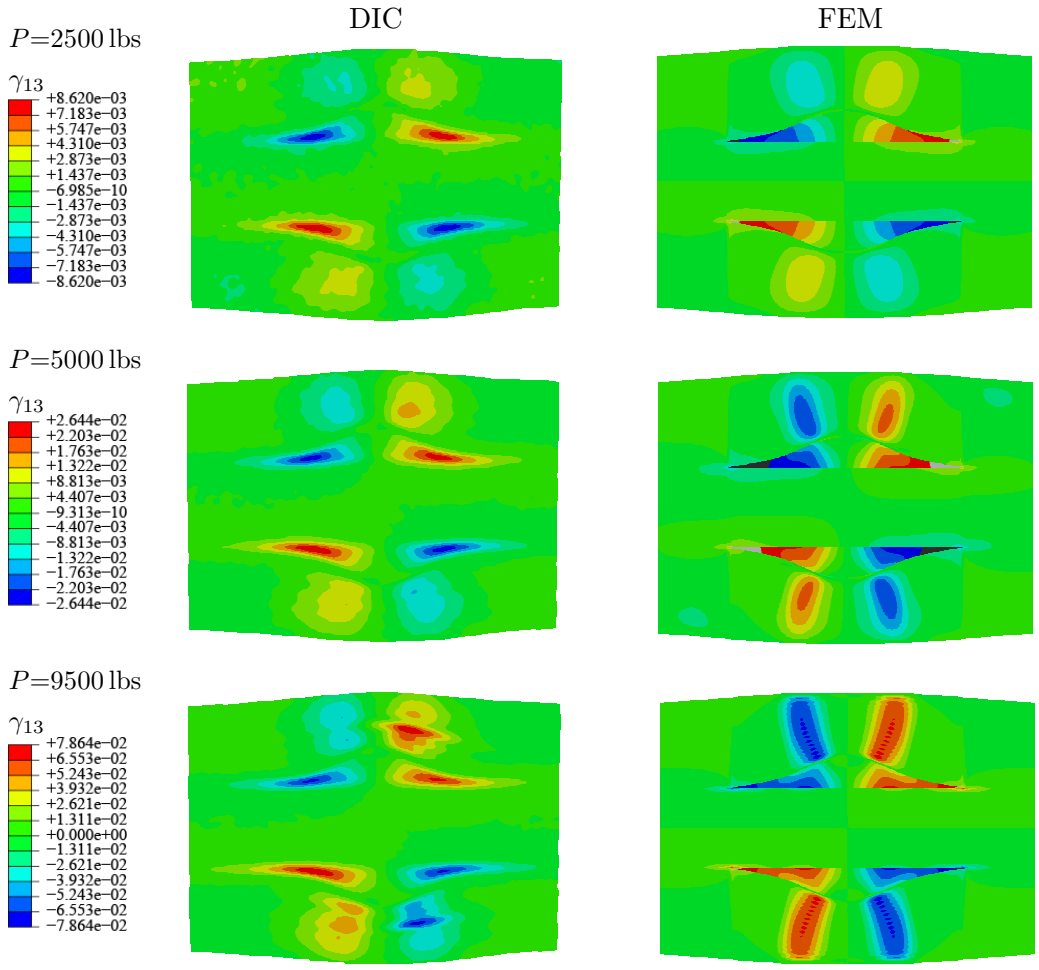

Figure 6.27: Measurement and FEM data for surface shear strain component for a unidirectional E-glass/8552-epoxy wrinkle specimen at various load magnitudes.

6.5.2 Laminated IM7-Carbon/8552-Epoxy Tape Wrinkle Specimens

A 88-ply $[(\pm 45_3/0_2)_3/(\pm 45_4/0_2)/(\pm 45_4/0_4/\pm 45_4)/(0_2/\pm 45_4)/(0_2/\pm 45_3)_3]_T$ IM7/8552 carbon/epoxy tape laminate with wavy plies was used in Reference [41] to study the interlaminar failure predictions. Finite element models were developed to implement the nonlinear shear stress-strain relations [41]. In this work, the updated shear properties obtained in Table 6.6 were applied in these finite element models to study the interlaminar shear responses. In particular, the finite element-based shear strain data were correlated with the DIC measurements for verification purpose.

Three 3.56 mm (0.14 inches) wide tensile specimens (W1, W2 and W3) were machined from a single 16.26 mm (0.64 inches) thick panel. The specimen thickness (laminate thickness) is 16.26 mm (0.64 inches); width is 3.56 mm (0.14 inches); length is 152.4 mm (6 inches) and gage (untabbed) length is 74.9 mm (2.95 inches). Figure 6.28 shows the wavy (wrinkle) regions in the specimens.

Three wrinkle specimens W1, W2, and W3 were statically loaded to failure. The DIC technique was used to monitor surface strains. Table 6.11 lists the cross-section dimensions. Delaminations for all specimens occur at the largest wrinkle between $[\pm 45]_4$ and $[0]_4$ ply-groups as expected and the failure loads are also listed in the same table.

Table 6.11: Cross-Section dimensions and failure loads for wrinkle specimens.

Specimen	Width mm (in.)	Thickness mm (in.)	Failure Loads N (lbs)
W1	16.289 (0.6413)	3.160 (0.1244)	18801 to 18895 (4227 to 4248)
W2	16.256 (0.6400)	3.203 (0.1261)	15764 to 15790 (3544 to 3550)
W3	16.261 (0.6402)	3.208 (0.1263)	18223 to 18241 (4097 to 4101)

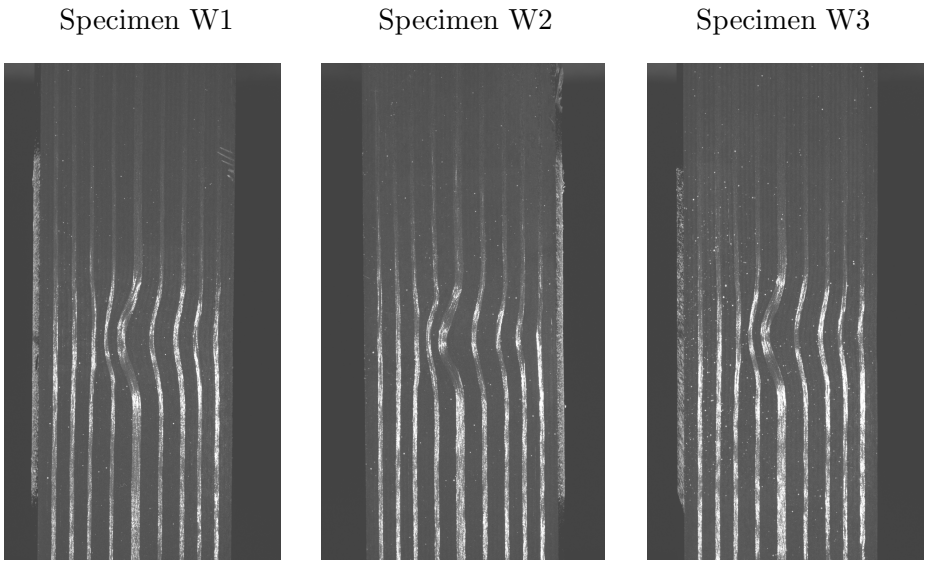

Figure 6.28: IM7-carbon/8552-epoxy tape wrinkle specimens.

Plane stress finite element models were built for the W1, W2, and W3 wrinkle specimens in ABAQUS software. The wavy-ply geometry for the finite element models was generated using digital images of the specimens. Series of points along the ply-group interfaces were imported into ABAQUS CAE and splinelines were used for interpolation. Figure 6.29 shows a typical finite element mesh for the W2 wrinkle specimen, where the 0° plies are shown in green color and the ±45° plies are shown in red. Extremely fine mesh is required to capture the complicated waviness geometry. Therefore, the problem was analyzed with plane stress elements to reduce the model size. The four-node plane stress elements with reduced integration (i.e., CPS4R elements in ABAQUS) were used. The model consists of about 100,000 elements and 200,000 degrees of freedom. The ±45° ply-groups are represented in the plane-stress finite element model through effective plane-stress stiffness properties in the wavy-ply local axial and transverse coordinates. A coordinate transformation for 3D stiffness tensor components [38] is used to obtain the linear stiffness constants for the ±45° plies.

Figure 6.30 shows the DIC measurements and finite element results for the inter-laminar shear strain (γ_{13}). For comparison purpose, the finite element results using initial shear properties are also shown. The predictions and measurements are in agreement. The DIC data are somewhat between the finite element results using initial shear properties and the finite element results using updated shear properties.

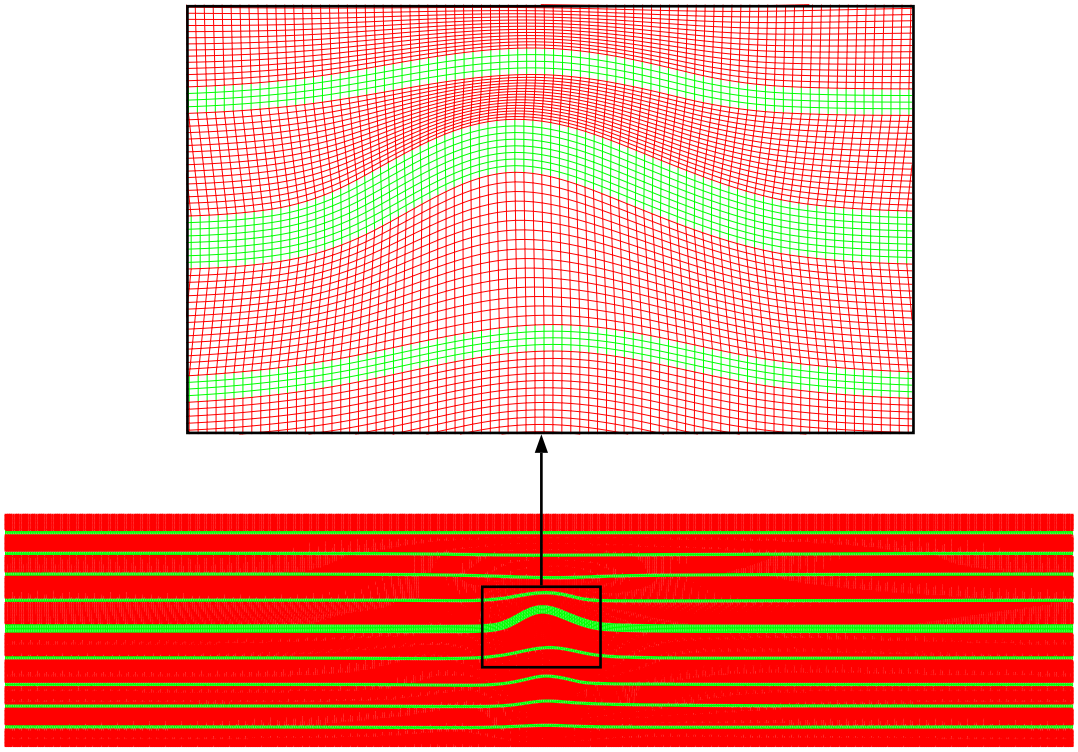

Figure 6.29: A typical finite element mesh for the W2 wrinkle specimen.

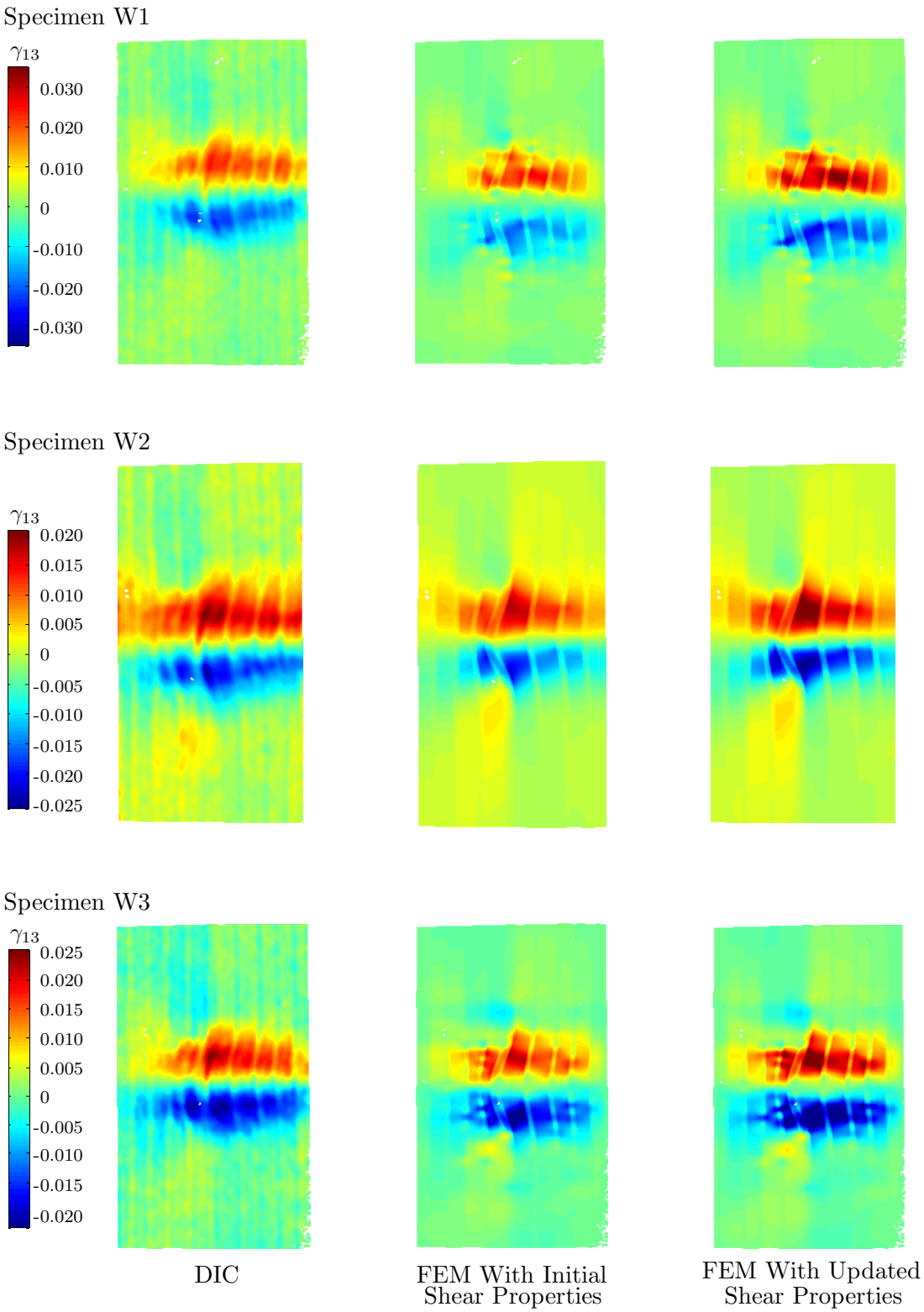

Figure 6.30: Measurement and FEM data for surface shear strain component for the laminated IM7-carbon/8552-epoxy wrinkle specimens.

CHAPTER VII

CONCLUSIONS AND FUTURE WORK

A method to improve the accuracy of stress-strain constitutive relation for composites is developed in this work. This method is based on short beam specimens subjected to three-point bend load, and the digital image correlation full-field surface deformation measurement technique. The finite element analysis is applied to obtain the stress values in the material characterization.

0° and 90° short-beam shear specimens can be machined from a single unidirectional panel and loaded in various principal material planes. Tensile and compressive moduli, Poisson's ratios, and shear stress-strain curves in the plane of loading are measured in one short beam experiment. The complete set of three-dimensional material properties can be generated. The concept is demonstrated on the unidirectional S2-glass/E773-epoxy, IM7-carbon/8552-epoxy and E-glass/5216-epoxy tape material systems.

Linear axial strain distributions through the specimen thickness were observed in measurements and verified by nonlinear finite element simulations. Such observation allows for simple closed-form approximations of the tensile and compressive moduli as well as shear stresses. A small difference between tensile and compressive modulus values for the glass/epoxy composite prompted another demonstration for IM7-carbon/8552-epoxy tape composite with a known lower compressive modulus compared to the tensile modulus in the fiber direction.

The nonlinear finite element simulations revealed the errors in the closed-form approximation (3.9) in material characterization. In particular, the discrepancy for the IM7-carbon composite specimens are more significant than the glass composite

specimens. An iterative procedure was developed in this work to obtain accurate stress state using finite element analysis. The shear properties obtained from the closed-form based stresses were used as an initial approximation in the finite element model. Consecutive finite element simulations were performed in an iterative manner in which the shear properties were updated iteratively using the FE-based stresses obtained at each iteration. The iterative procedure converges rapidly and only a few iterations are needed. Moreover, convergence has been achieved for all the twenty specimens under study. The accuracy of the numerical procedure is verified by comparing the finite element strain results with full-field measurements. The procedure is further verified using the V-notched beam test results. Excellent agreement has been achieved in the verification.

The nonlinear constitutive model was implemented in the finite element code via a user material subroutine. Moreover, the classical laminate theory can be modified in a incremental manner to account for the shear nonlinearity. The procedure was extended to the bending analysis of laminated beam subjected to three-point bending. It is noted that, although only the Ramberg-Osgood equation was considered in this work, the implementation of shear nonlinearity can be easily extended to other nonlinear elasticity models, e.g., the third-order polynomial model [30].

The nonlinear shear properties obtained from the unidirectional prepreg tapes were used to study the axial and interlaminar shear responses of laminated beam specimens under three-point bending. Nonlinear finite element analysis was applied to perform detailed numerical study. The strain measurements are in good agreement with the results obtained from nonlinear finite element simulation, which again verifies the accuracy of the material characterization.

This method demonstrates a combination of full-field strain measurement and nonlinear finite element stress analysis in material characterization. Simplicity of the short-beam specimens and accuracy of the stress solution make the present method

attractive for measurement of three-dimensional stress-strain relations for anisotropic materials at various load rates.

Several recommendations for future work are given below.

The shear responses in the 2-3 material plane were obtained using 90° SBS specimens loaded in the corresponding material plane. However, in this work the specimens failed early in small strain regime. Thus, the nonlinear shear behavior exhibiting in relative large strain regime was not measured. An important task in future study is to design a test method to characterize the full shear stress-strain response in the 2-3 material plane.

A challenge in composite material shear tests is that the results from different test methods are oftentimes inconsistent. This work has demonstrated that good consistency can be achieved between the SBS test and V-notched beam test. Further experimental work is needed to examine the consistency of the SBS test with other popular test methods, for example, the $[\pm 45^\circ]_{ns}$ tensile test.

The Ramberg-Osgood equation was used in this work as a mathematical simplification of the shear response under monotonic loading. No assumption of permanent deformation upon unloading is made. However, this mathematical representation may include damage and viscoplasticity effects. A damage model is therefore required for general loading conditions. Loading-unloading response under quasi-static and fatigue loading conditions must be characterized.

APPENDIX A

IMPLEMENTATION OF NONLINEAR CONSTITUTIVE LAWS IN CLASSICAL LAMINATION THEORY

This appendix presents an example to implement the nonlinear shear model in the closed-form solutions of laminated composites. The classical laminate theory can be utilized in an incremental manner to account for the nonlinear behavior in a lamina. Typical approaches are based explicit formulations by assuming piecewise nonlinear behavior in the incremental loading procedure [14, 45]. Most equations in the following derivation are the incremental forms of their counterparts in the classical laminate theory [34]. The coordinate and sign conventions illustrated in Figure A.1 are adopted.

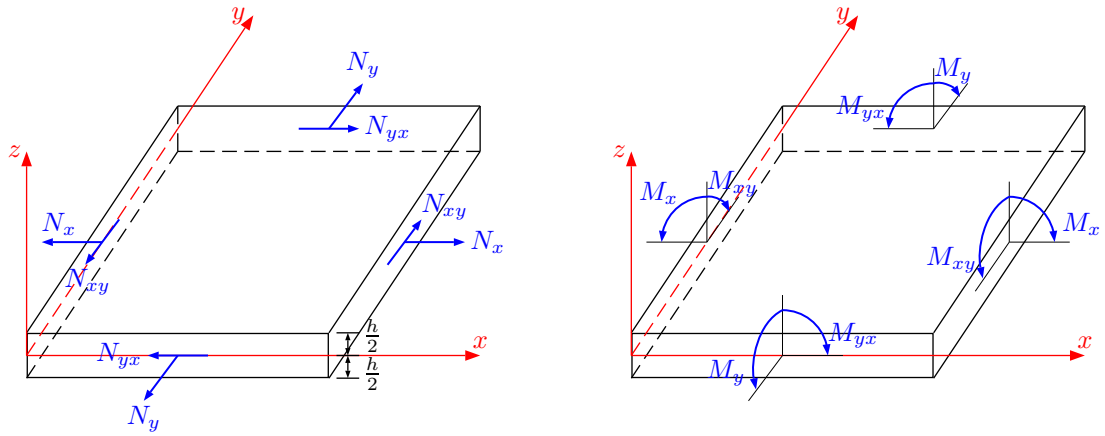

Figure A.1: In-plane forces and moments on a flat laminate.

The incremental procedure is based on a force-controlled scheme in which the applied force is divided into multiple increments. A stress component $(\sigma_{ij}^{(k)})_n$ in the

kth layer at the end of the current increment n is updated by the sum of the stress component $(\sigma_{ij}^{(k)})_{n-1}$ obtained from the previous increment and the current stress increment $(\Delta\sigma_{ij}^{(k)})_n$:

$$\begin{Bmatrix} \sigma_{11}^{(k)} \\ \sigma_{22}^{(k)} \\ \sigma_{12}^{(k)} \end{Bmatrix}_n = \begin{Bmatrix} \sigma_{11}^{(k)} \\ \sigma_{22}^{(k)} \\ \sigma_{12}^{(k)} \end{Bmatrix}_{n-1} + \begin{Bmatrix} \Delta\sigma_{11}^{(k)} \\ \Delta\sigma_{22}^{(k)} \\ \Delta\sigma_{12}^{(k)} \end{Bmatrix}_n \tag{A.1}$$

According to equation (2.12), the strain increments are related to the stress increments through the tangential stiffness matrix:

$$\begin{Bmatrix} \Delta\sigma_{11}^{(k)} \\ \Delta\sigma_{22}^{(k)} \\ \Delta\sigma_{12}^{(k)} \end{Bmatrix}_n = \begin{bmatrix} Q_{11} & Q_{12} & 0 \\ Q_{12} & Q_{22} & 0 \\ 0 & 0 & \left(Q_{66}^{(k)}\right)_n \end{bmatrix} \begin{Bmatrix} \Delta\epsilon_{11}^{(k)} \\ \Delta\epsilon_{22}^{(k)} \\ \Delta\gamma_{12}^{(k)} \end{Bmatrix}_n \tag{A.2}$$

where

$$\left(Q_{66}^{(k)}\right)_n = \frac{1}{\frac{1}{G_{12}} + \frac{1}{K_{12}}\frac{1}{n_{12}}\left[\frac{\left(\sigma_{12}^{(k)}\right)_{n-1}}{K_{12}}\right]^{\frac{1}{n_{12}}-1}} \tag{A.3}$$

It is noted that $\left(Q_{66}^{(k)}\right)_n$ is calculated based on the shear stress at the beginning of the current increment.

In the $x-y$ coordinates, the stress update for the layer k is given by

$$\begin{Bmatrix} \sigma_x^{(k)} \\ \sigma_y^{(k)} \\ \sigma_{xy}^{(k)} \end{Bmatrix}_n = \begin{Bmatrix} \sigma_x^{(k)} \\ \sigma_y^{(k)} \\ \sigma_{xy}^{(k)} \end{Bmatrix}_{n-1} + \begin{Bmatrix} \Delta\sigma_x^{(k)} \\ \Delta\sigma_y^{(k)} \\ \Delta\sigma_{xy}^{(k)} \end{Bmatrix}_n \tag{A.4}$$

and the incremental stress-strain relations in the $x-y$ coordinates are obtained by transforming the local relations (A.2) according to fiber orientation of the kth layer:

$$\begin{Bmatrix} \Delta\sigma_x^{(k)} \\ \Delta\sigma_y^{(k)} \\ \Delta\sigma_{xy}^{(k)} \end{Bmatrix}_n = \begin{bmatrix} \bar{Q}_{11}^{(k)} & \bar{Q}_{12}^{(k)} & \bar{Q}_{16}^{(k)} \\ \bar{Q}_{12}^{(k)} & \bar{Q}_{22}^{(k)} & \bar{Q}_{26}^{(k)} \\ \bar{Q}_{16}^{(k)} & \bar{Q}_{26}^{(k)} & \bar{Q}_{66}^{(k)} \end{bmatrix}_n \begin{Bmatrix} \Delta\epsilon_x \\ \Delta\epsilon_y \\ \Delta\gamma_{xy} \end{Bmatrix}_n \tag{A.5}$$

The individual $\bar{Q}_{ij}^{(k)}$ terms of the transformed reduced stiffness matrix are

$$\begin{aligned}
\left(\bar{Q}_{11}^{(k)}\right)_n &= Q_{11}c^4 + 2\left[Q_{12} + 2\left(Q_{66}^{(k)}\right)_n\right]c^2s^2 + Q_{22}s^4 \\
\left(\bar{Q}_{12}^{(k)}\right)_n &= \left[Q_{11} + Q_{22} - 4\left(Q_{66}^{(k)}\right)_n\right]c^2s^2 + Q_{12}\left(c^4 + s^4\right) \\
\left(\bar{Q}_{22}^{(k)}\right)_n &= Q_{11}s^4 + 2\left[Q_{12} + 2\left(Q_{66}^{(k)}\right)_n\right]c^2s^2 + Q_{22}c^4 \\
\left(\bar{Q}_{16}^{(k)}\right)_n &= \left[Q_{11} - Q_{12} - 2\left(Q_{66}^{(k)}\right)_n\right]c^3s + \left[Q_{12} - Q_{22} + 2\left(Q_{66}^{(k)}\right)_n\right]s^3c \\
\left(\bar{Q}_{26}^{(k)}\right)_n &= \left[Q_{11} - Q_{12} - 2\left(Q_{66}^{(k)}\right)_n\right]cs^3 + \left[Q_{12} - Q_{22} + 2\left(Q_{66}^{(k)}\right)_n\right]sc^3 \\
\left(\bar{Q}_{66}^{(k)}\right)_n &= \left[Q_{11} + Q_{22} - 2Q_{12} - 2\left(Q_{66}^{(k)}\right)_n\right]c^2s^2 + \left(Q_{66}^{(k)}\right)_n\left(c^4 + s^4\right)
\end{aligned} \tag{A.6}$$

where c and s are the cosine and sine functions of $\theta^{(k)}$, i.e., fiber orientation of the kth layer:

$$c = \cos\left(\theta^{(k)}\right) \qquad \text{and} \qquad s = \sin\left(\theta^{(k)}\right) \tag{A.7}$$

Analogous to equation (A.1), the incremental form of laminate strains is written as

$$\begin{Bmatrix} \epsilon_x \\ \epsilon_y \\ \gamma_{xy} \end{Bmatrix}_n = \begin{Bmatrix} \epsilon_x \\ \epsilon_y \\ \gamma_{xy} \end{Bmatrix}_{n-1} + \begin{Bmatrix} \Delta\epsilon_x \\ \Delta\epsilon_y \\ \Delta\gamma_{xy} \end{Bmatrix}_n \tag{A.8}$$

The laminate strains at the end of the current increment n are given by

$$\begin{Bmatrix} \epsilon_x \\ \epsilon_y \\ \gamma_{xy} \end{Bmatrix}_n = \begin{Bmatrix} \epsilon_x^0 \\ \epsilon_y^0 \\ \gamma_{xy}^0 \end{Bmatrix}_n + z\begin{Bmatrix} \kappa_x \\ \kappa_y \\ \kappa_{xy} \end{Bmatrix}_n \tag{A.9}$$

The current strain increments are the summation of middle-surface strain increments and curvature increments:

$$\begin{Bmatrix} \Delta\epsilon_x \\ \Delta\epsilon_y \\ \Delta\gamma_{xy} \end{Bmatrix}_n = \begin{Bmatrix} \Delta\epsilon_x^0 \\ \Delta\epsilon_y^0 \\ \Delta\gamma_{xy}^0 \end{Bmatrix}_n + z\begin{Bmatrix} \Delta\kappa_x \\ \Delta\kappa_y \\ \Delta\kappa_{xy} \end{Bmatrix}_n \tag{A.10}$$

The resultant forces and moments acting on a laminate are obtained by integration of stresses in each layer through the laminate thickness. The entire collection of force

and moment resultants for a N-layered laminate is illustrated in Figure A.1. The incremental form of resultant forces and moments are written as

$$\begin{Bmatrix} N_x \\ N_y \\ N_{xy} \end{Bmatrix}_n = \begin{Bmatrix} N_x \\ N_y \\ N_{xy} \end{Bmatrix}_{n-1} + \begin{Bmatrix} \Delta N_x \\ \Delta N_y \\ \Delta N_{xy} \end{Bmatrix}_n \tag{A.11}$$

and

$$\begin{Bmatrix} M_x \\ M_y \\ M_{xy} \end{Bmatrix}_n = \begin{Bmatrix} M_x \\ M_y \\ M_{xy} \end{Bmatrix}_{n-1} + \begin{Bmatrix} \Delta M_x \\ \Delta M_y \\ \Delta M_{xy} \end{Bmatrix}_n \tag{A.12}$$

At the end of the current increment n, the in-plane forces per unit length $\{N_x, N_y, N_{xy}\}_n$ are given by

$$\{N\}_n = \begin{Bmatrix} N_x \\ N_y \\ N_{xy} \end{Bmatrix}_n = \sum_{k=1}^{N} \int_{z_{k-1}}^{z_k} \begin{Bmatrix} \sigma_{xx}^{(k)} \\ \sigma_{yy}^{(k)} \\ \sigma_{xy}^{(k)} \end{Bmatrix}_n dz \tag{A.13}$$

and the moment per unit length $\{M_x, M_y, M_{xy}\}_n$ are given by

$$\{M\}_n = \begin{Bmatrix} M_x \\ M_y \\ M_{xy} \end{Bmatrix}_n = \sum_{k=1}^{N} \int_{z_{k-1}}^{z_k} \begin{Bmatrix} \sigma_{xx}^{(k)} \\ \sigma_{yy}^{(k)} \\ \sigma_{xy}^{(k)} \end{Bmatrix}_n z dz \tag{A.14}$$

where z_k is the directed distance to the outer surface of the kth layer and z_{k-1} is the directed distance to the inner surface of the kth layer.

The increments of in-plane forces per unit length $\{\Delta N_x, \Delta N_y, \Delta N_{xy}\}_n$ is obtained by substituting equation (A.4) into equation (A.13)

$$\{\Delta N\}_n = \begin{Bmatrix} \Delta N_x \\ \Delta N_y \\ \Delta N_{xy} \end{Bmatrix}_n = \sum_{k=1}^{N} \int_{z_{k-1}}^{z_k} \begin{Bmatrix} \Delta\sigma_{xx}^{(k)} \\ \Delta\sigma_{yy}^{(k)} \\ \Delta\sigma_{xy}^{(k)} \end{Bmatrix}_n dz \tag{A.15}$$

Similarly, the increments of moment per unit length $\{\Delta M_x, \Delta M_y, \Delta M_{xy}\}_n$ is obtained by substituting equation (A.4) into equation (A.14)

$$\{\Delta M\}_n = \begin{Bmatrix} \Delta M_x \\ \Delta M_y \\ \Delta M_{xy} \end{Bmatrix}_n = \sum_{k=1}^{N} \int_{z_{k-1}}^{z_k} \begin{Bmatrix} \Delta\sigma_{xx}^{(k)} \\ \Delta\sigma_{yy}^{(k)} \\ \Delta\sigma_{xy}^{(k)} \end{Bmatrix}_n z dz \tag{A.16}$$

Combining equations (A.5), (A.10) and (A.15) yields

$$\begin{Bmatrix} \Delta N_x \\ \Delta N_y \\ \Delta N_{xy} \end{Bmatrix}_n = \sum_{k=1}^{N} \int_{z_{k-1}}^{z_k} \begin{bmatrix} \bar{Q}_{11}^{(k)} & \bar{Q}_{12}^{(k)} & \bar{Q}_{16}^{(k)} \\ \bar{Q}_{12}^{(k)} & \bar{Q}_{22}^{(k)} & \bar{Q}_{26}^{(k)} \\ \bar{Q}_{16}^{(k)} & \bar{Q}_{26}^{(k)} & \bar{Q}_{66}^{(k)} \end{bmatrix}_n \left[\begin{Bmatrix} \Delta\epsilon_x^0 \\ \Delta\epsilon_y^0 \\ \Delta\gamma_{xy}^0 \end{Bmatrix}_n dz + \begin{Bmatrix} \Delta\kappa_x \\ \Delta\kappa_y \\ \Delta\kappa_{xy} \end{Bmatrix}_n z dz \right] \tag{A.17}$$

Similarly, combining equations (A.5), (A.10) and (A.16) yields

$$\begin{Bmatrix} \Delta M_x \\ \Delta M_y \\ \Delta M_{xy} \end{Bmatrix}_n = \sum_{k=1}^{N} \int_{z_{k-1}}^{z_k} \begin{bmatrix} \bar{Q}_{11}^{(k)} & \bar{Q}_{12}^{(k)} & \bar{Q}_{16}^{(k)} \\ \bar{Q}_{12}^{(k)} & \bar{Q}_{22}^{(k)} & \bar{Q}_{26}^{(k)} \\ \bar{Q}_{16}^{(k)} & \bar{Q}_{26}^{(k)} & \bar{Q}_{66}^{(k)} \end{bmatrix}_n \left[\begin{Bmatrix} \Delta\epsilon_x^0 \\ \Delta\epsilon_y^0 \\ \Delta\gamma_{xy}^0 \end{Bmatrix}_n z dz + \begin{Bmatrix} \Delta\kappa_x \\ \Delta\kappa_y \\ \Delta\kappa_{xy} \end{Bmatrix}_n z^2 dz \right] \tag{A.18}$$

Recalling that $\left\{\Delta\epsilon_x^0, \Delta\epsilon_y^0, \Delta\gamma_{xy}^0\right\}_n$ and $\left\{\Delta\kappa_x, \Delta\kappa_y, \Delta\kappa_{xy}^0\right\}_n$ are middle-surface values so that they can be removed from within the summation signs. Equations (A.17) and (A.18) can be written as

$$\begin{Bmatrix} \Delta N_x \\ \Delta N_y \\ \Delta N_{xy} \end{Bmatrix}_n = \begin{bmatrix} A_{11} & A_{12} & A_{16} \\ A_{12} & A_{22} & A_{26} \\ A_{16} & A_{26} & A_{66} \end{bmatrix}_n \begin{Bmatrix} \Delta\epsilon_x^0 \\ \Delta\epsilon_y^0 \\ \Delta\gamma_{xy}^0 \end{Bmatrix}_n + \begin{bmatrix} B_{11} & B_{12} & B_{16} \\ B_{12} & B_{22} & A_{26} \\ B_{16} & B_{26} & B_{66} \end{bmatrix}_n \begin{Bmatrix} \Delta\kappa_x \\ \Delta\kappa_y \\ \Delta\kappa_{xy} \end{Bmatrix}_n \tag{A.19}$$

and

$$\begin{Bmatrix} \Delta M_x \\ \Delta M_y \\ \Delta M_{xy} \end{Bmatrix}_n = \begin{bmatrix} B_{11} & B_{12} & B_{16} \\ B_{12} & B_{22} & B_{26} \\ B_{16} & B_{26} & B_{66} \end{bmatrix}_n \begin{Bmatrix} \Delta\epsilon_x^0 \\ \Delta\epsilon_y^0 \\ \Delta\gamma_{xy}^0 \end{Bmatrix}_n + \begin{bmatrix} D_{11} & D_{12} & D_{16} \\ D_{12} & D_{22} & D_{26} \\ D_{16} & D_{26} & D_{66} \end{bmatrix}_n \begin{Bmatrix} \Delta\kappa_x \\ \Delta\kappa_y \\ \Delta\kappa_{xy} \end{Bmatrix}_n \tag{A.20}$$

where the extensional stiffnesses $(A_{ij})_n$, bending-extension coupling stiffnesses $(B_{ij})_n$ and bending stiffnesses $(D_{ij})_n$ are given by

$$\begin{aligned}
(A_{ij})_n &= \sum_{k=1}^{N} \left(\bar{Q}_{ij}^{(k)}\right)_n \left(z_k^2 - z_{k-1}^2\right), \quad i,j = 1,2,6 \\
(B_{ij})_n &= \frac{1}{2}\sum_{k=1}^{N} \left(\bar{Q}_{ij}^{(k)}\right)_n \left(z_k^2 - z_{k-1}^2\right), \quad i,j = 1,2,6 \\
(D_{ij})_n &= \frac{1}{3}\sum_{k=1}^{N} \left(\bar{Q}_{ij}^{(k)}\right)_n \left(z_k^3 - z_{k-1}^3\right), \quad i,j = 1,2,6
\end{aligned} \tag{A.21}$$

It should be note that the stiffnesses given above are the tangential stiffnesses at the end of current increment n.

The solution procedure is essentially an explicit formulation since the incremental shear stiffness $\left(Q_{66}^{(k)}\right)_n$ in equation (2.14) is linearized at the beginning of the current increment. Caution should be exercised to prevent deviation from the nonlinear shear model. Figure A.2(a) shows the obtained shear stress-strain response for a $[\pm 45^\circ]_{\mathrm{s}}$ symmetric angle-ply laminate consisting of 0.25-mm thick unidirectional glass/epoxy laminae. The material properties are listed in the numerical test in Chapter 2 (on Page 19). The laminate is subjected to unform extension in the x-direction. Thus, the individual layers exhibit pure shear responses in the principal material coordinates. An extensional force ($N_x = 3870\,\mathrm{N}$) is applied. The solution procedure is divided into 50 increments with a fixed load increment ($\Delta N_x = 77.4\,\mathrm{N}$). As one can observe from Figure A.2(a), numerical error induced by the stiffness linearization is accumulated and becomes significant as load increases. Reducing increment size by using more increments may reduce the numerical error. However, a more efficient approach is to adjust increment size automatically to minimize the induced error. In this approach, a tolerance value *tol* is chosen to check the convergence at the end of the current increment n:

$$error = \frac{(\gamma_{12})_n - (\gamma_{12})_{\mathrm{ext}}}{(\gamma_{12})_{\mathrm{ext}}} \tag{A.22}$$

where

$$(\gamma_{12})_{\text{ext}} = \frac{(\sigma_{12})_n}{G_{12}} + \left[\frac{(\sigma_{12})_n}{K_{12}}\right]^{\frac{1}{n_{12}}} \tag{A.23}$$

The solution is converged if $error \leqslant tol$ and the incremental procedure continues. Otherwise, the solution procedure abandons the increment and starts again with the increment size set to 50% of its previous value. It then attempts to find a converged solution with this smaller time increment. If the solution still fails to converge, the solution procedure reduces the increment size again. This process is continued until a solution is found for current load step. The solution procedure automatically increases the increment size by 25% if two consecutive increments converged without cutting back, which indicates that the solution is being found fairly easily. A control parameter is set to abandon the solution procedure if the increment is too small. Figure A.2(b) shows the solution procedure with adjustable increment size. A total of 96 increments were used. The obtained shear stress-strain response is in excellent agreement with the nonlinear shear model.

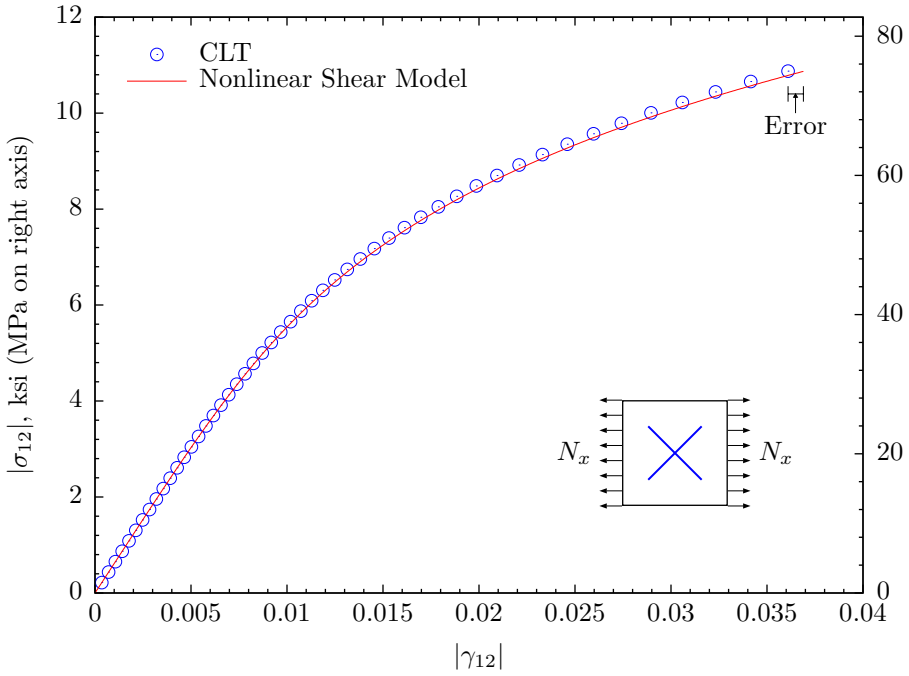

(a)

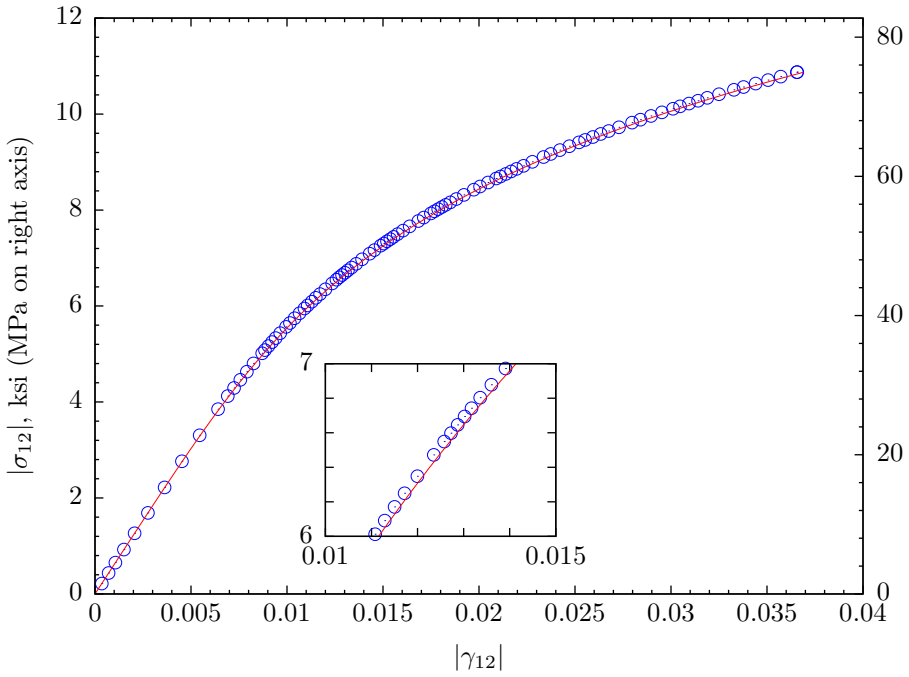

(b)

Figure A.2: Shear stress-strain response in principal material coordinates for a symmetric angle-ply laminate $[\pm 45^\circ]_s$ subjected to uniform axial stress. (a) Fixed increment size; (b) Adjustable increment size.

APPENDIX B

INCREMENTAL FORM FOR BENDING ANALYSIS OF LAMINATED BEAM WITH SHEAR NONLINEARITY

As presented in Appendix A, the nonlinear shear model is implemented in the classical lamination theory via an incremental approach. The mathematical simplicity of Ramberg-Osgood equation (2.3) also allows the implementation of nonlinear shear model in the closed-form solutions for bending analysis of laminated beam. Closed-form solution for symmetric laminated beam can be derived by considering a beam as a special cases of a laminated plate. The derivation based on classical beam theory can be found in early publications and textbooks [44,47,58,60]. Following the similar manner presented in Appendix A, the theory can be extended to the bending analysis of laminated beam with shear nonlinearity. Again, most of the equations in the following are simply the incremental forms of their counterparts in the linear shear case [60].

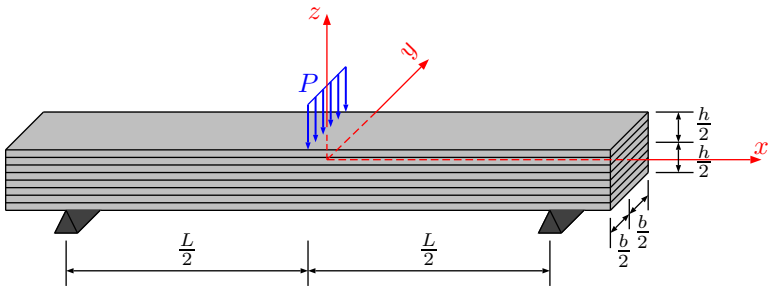

Figure B.1: Geometry of a laminated beam under three-point bending.

For pure bending of a symmetric laminate, the constitutive relations (A.20) reduce

to the form

$$\begin{Bmatrix} \Delta M_x \\ \Delta M_y \\ \Delta M_{xy} \end{Bmatrix}_n = \begin{bmatrix} D_{11} & D_{12} & D_{16} \\ D_{12} & D_{22} & D_{26} \\ D_{16} & D_{26} & D_{66} \end{bmatrix}_n \begin{Bmatrix} \Delta \kappa_x \\ \Delta \kappa_y \\ \Delta \kappa_{xy} \end{Bmatrix}_n \tag{B.1}$$

Equation (B.1) can be written in the following inverted form

$$\begin{Bmatrix} \Delta \kappa_x \\ \Delta \kappa_y \\ \Delta \kappa_{xy} \end{Bmatrix}_n = \begin{bmatrix} D^*_{11} & D^*_{12} & D^*_{16} \\ D^*_{12} & D^*_{22} & D^*_{26} \\ D^*_{16} & D^*_{26} & D^*_{66} \end{bmatrix}_n \begin{Bmatrix} \Delta M_x \\ \Delta M_y \\ \Delta M_{xy} \end{Bmatrix}_n \tag{B.2}$$

where D^*_{ij} are the elements of the inverse matrix of $[D_{ij}]$.

It is assumed that $M_y = M_{xy} = 0$, thus we have

$$(\Delta M_y)_n = (\Delta M_{xy})_n = 0 \tag{B.3}$$

at any increment n. The increment index n is dropped in the following derivation for notation simplicity.

Applying the assumption (B.3) in equation (B.2) leads to

$$\Delta \kappa_x = D^*_{11} \Delta M_x \tag{B.4}$$

$$\Delta \kappa_y = D^*_{12} \Delta M_x \tag{B.5}$$

$$\Delta \kappa_{xy} = D^*_{16} \Delta M_x \tag{B.6}$$

Under static loading in the absence of body forces, the equilibrium equations of laminated plates are written as the following incremental forms

$$\frac{\partial \Delta N_x}{\partial x} + \frac{\partial \Delta N_{xy}}{\partial y} = 0 \tag{B.7}$$

$$\frac{\partial \Delta N_{xy}}{\partial x} + \frac{\partial \Delta N_y}{\partial y} = 0 \tag{B.8}$$

$$\frac{\partial \Delta Q_x}{\partial x} + \frac{\partial \Delta Q_{xy}}{\partial y} + \Delta q = 0 \tag{B.9}$$

$$\frac{\partial \Delta M_x}{\partial x} + \frac{\partial \Delta M_{xy}}{\partial y} - \Delta Q_x = 0 \tag{B.10}$$

$$\frac{\partial \Delta M_{xy}}{\partial x} + \frac{\partial \Delta M_y}{\partial y} - \Delta Q_y = 0 \tag{B.11}$$

Combining equations (B.9), (B.10) and (B.11) to eliminate the transverse shear resultants leads to

$$\frac{\partial^2 \Delta M_x}{\partial x^2} + \frac{\partial^2 \Delta M_y}{\partial y^2} + 2\frac{\partial^2 \Delta M_{xy}}{\partial x \partial y} + \Delta q = 0 \tag{B.12}$$

Taking into account the assumption (B.3), equation (B.12) for the bending of plates reduces to

$$\frac{d^2 \Delta M_x}{dx^2} + \Delta q = 0 \tag{B.13}$$

Applying the assumption $\Delta M_{xy} = 0$ in equation (B.10) and multiplying the result by beam width b, we obtain the relationship in incremental form

$$\Delta Q = \frac{d\Delta M}{dx} \tag{B.14}$$

where

$$\Delta Q = b\Delta Q_x \tag{B.15}$$

For symmetric laminates under pure bending the strain at the end of the current increment n, equation (A.7) reduces to

$$\begin{Bmatrix} \Delta\epsilon_x \\ \Delta\epsilon_y \\ \Delta\gamma_{xy} \end{Bmatrix}_n = z \begin{Bmatrix} \Delta\kappa_x \\ \Delta\kappa_y \\ \Delta\kappa_{xy} \end{Bmatrix}_n \tag{B.16}$$

Consequently, equation (A.5) becomes

$$\begin{Bmatrix} \Delta\sigma_x^{(k)} \\ \Delta\sigma_y^{(k)} \\ \Delta\sigma_{xy}^{(k)} \end{Bmatrix}_n = z \begin{bmatrix} \bar{Q}_{11}^{(k)} & \bar{Q}_{12}^{(k)} & \bar{Q}_{16}^{(k)} \\ \bar{Q}_{12}^{(k)} & \bar{Q}_{22}^{(k)} & \bar{Q}_{26}^{(k)} \\ \bar{Q}_{16}^{(k)} & \bar{Q}_{26}^{(k)} & \bar{Q}_{66}^{(k)} \end{bmatrix}_n \begin{Bmatrix} \Delta\kappa_x \\ \Delta\kappa_y \\ \Delta\kappa_{xy} \end{Bmatrix}_n \tag{B.17}$$

Substituting equation (B.2) into equation (B.17) and multiplying the results by b, we obtain the current in-plane stress increments at the kth layer:

$$\left(\Delta\sigma_x^{(k)}\right)_n = z\left(f_1^{(k)}\right)_n \frac{\Delta M}{I} \tag{B.18}$$

$$\left(\Delta\sigma_y^{(k)}\right)_n = z\left(f_2^{(k)}\right)_n \frac{\Delta M}{I} \tag{B.19}$$

$$\left(\Delta\sigma_{xy}^{(k)}\right)_n = z\left(f_3^{(k)}\right)_n \frac{\Delta M}{I} \tag{B.20}$$

where

$$\left(f_1^{(k)}\right)_n = \left[\left(\bar{Q}_{11}^{(k)}\right)_n (D_{11}^*)_n + \left(\bar{Q}_{12}^{(k)}\right)_n (D_{12}^*)_n + \left(\bar{Q}_{16}^{(k)}\right)_n (D_{16}^*)_n\right] \frac{h^3}{12} \quad \text{(B.21)}$$

$$\left(f_2^{(k)}\right)_n = \left[\left(\bar{Q}_{12}^{(k)}\right)_n (D_{11}^*)_n + \left(\bar{Q}_{22}^{(k)}\right)_n (D_{12}^*)_n + \left(\bar{Q}_{16}^{(k)}\right)_n (D_{16}^*)_n\right] \frac{h^3}{12} \quad \text{(B.22)}$$

$$\left(f_3^{(k)}\right)_n = \left[\left(\bar{Q}_{16}^{(k)}\right)_n (D_{11}^*)_n + \left(\bar{Q}_{26}^{(k)}\right)_n (D_{12}^*)_n + \left(\bar{Q}_{66}^{(k)}\right)_n (D_{16}^*)_n\right] \frac{h^3}{12} \quad \text{(B.23)}$$

For homogeneous beams $f_1^{(k)} = 1$, $f_2^{(k)} = f_3^{(k)} = 0$. Equation (B.18) reduced to the form analogous to the classical beam theory:

$$\sigma_x = \frac{Mz}{I} \quad \text{(B.24)}$$

which has the same form as equation (5.2), while equations (B.19) and (B.20) vanish.

The interlaminar shear stress increment $\Delta\sigma_{xz}$ can be determined by substituting equations (B.18) and (B.19) into the incremental form of the equilibrium equation:

$$\frac{\partial\left(\Delta\sigma_x^{(k)}\right)_n}{\partial x} + \frac{\partial\left(\Delta\sigma_{xy}^{(k)}\right)_n}{\partial y} + \frac{\partial\left(\Delta\sigma_{xz}^{(k)}\right)_n}{\partial z} = 0 \quad \text{(B.25)}$$

and integrating the result:

$$\left(\Delta\sigma_{xz}^{(k)}\right)_n = -\frac{1}{I}\int_{-\frac{h}{2}}^{z_k} \left(f_1^{(k)}\right)_n \frac{d\Delta M}{dx} z dz \quad \text{(B.26)}$$

Using equation (B.14) in conjunction with equation (B.26), we obtain

$$\left(\Delta\sigma_{xz}^{(k)}\right)_n = -\frac{\Delta Q}{I}\int_{-\frac{h}{2}}^{z_k} \left(f_1^{(k)}\right)_n z dz \quad \text{(B.27)}$$

The integral in equation (B.27) assures continuity of the transverse shear stress at layer interfaces. The current interlaminar shear stress $\left(\sigma_{xz}^{(k)}\right)_n$ can be obtained from the incremental equation:

$$\left(\sigma_{xz}^{(k)}\right)_n = \left(\sigma_{xz}^{(k)}\right)_{n-1} + \left(\Delta\sigma_{xz}^{(k)}\right)_n \quad \text{(B.28)}$$

For homogeneous materials the integration can be evaluated in closed form with the result

$$\sigma_{xz} = -\frac{h^2 Q}{8I}\left[1 - \left(\frac{2z}{h}\right)^2\right] \quad \text{(B.29)}$$

For the beam under three-point bending, we have $Q = -P/2$. The above equation reduces to the closed-form solution for homogeneous SBS specimens, i.e, equation (3.14).

It is noted that since the axial and interlaminar shear responses are the major concern, no additional kinematic assumption is made in the above derivation. Nevertheless, the incremental approach can also be applied to various shear deformation beam theories for better prediction of deflection [47].

REFERENCES

[1] http://www.correlatedsolutions.com (Date Assessed: June, 2010).

[2] http://www.hexcel.com (Date Assessed: June, 2010).

[3] Abali, F., Pora, A., and Shivakumar, K., "Modified short beam test for measurement of interlaminar shear strength of composites," *Journal of Composite Materials*, vol. 37, no. 5, pp. 453–464, 2003.

[4] Adams, D. F., Carlsson, L. A., and Pipes, R. B., *Experimental Characterization of Advanced Composite Materials*. CRC Press LLC, third ed., 2002.

[5] Adams, D. F. and Lewis, E. Q., "Current status of composite material shear test methods," *the SAMPE Journal*, vol. 31, no. 6, pp. 32–41, 1994.

[6] Adams, D. O. and Hyer, M. W., "Effects of layer waviness on the compression strength of thermoplastic composite laminates," *Journal of Reinforced Plastics and Composites*, vol. 12, pp. 414–429, 1993.

[7] Adams, D. O. and Hyer, M. W., "Effects of layer waviness on the compression fatigue performance of thermoplastic composite laminates," *Fatigue*, vol. 16, pp. 385–391, 1994.

[8] American Society for Testing and Materials, *Standard test method for shear properties of composite materials by the V-notched beam method*, ASTM Standard D 5379/D 5379M, 2005.

[9] American Society for Testing and Materials, *Standard test method for tensile properties of polymer matrix composite materials*, ASTM Standard D 3039, 2005.

[10] American Society for Testing and Materials, *Standard test method for measuring the curved beam strength of a fiber-reinforced polymer-matrix composite*, ASTM Standard D 6415/D 6415M, 2006.

[11] American Society for Testing and Materials, *Standard test method for short-beam strength of polymer matrix composite materials and their laminates*, ASTM Standard D 2344/D 2344M, 2006.

[12] American Society for Testing and Materials, *Standard test method for in-plane shear properties of polymer matrix composite materials by the rail shear method*, ASTM Standard D 4255, 2007.

[13] American Society for Testing and Materials, *Standard test method for in-plane shear response of polymer matrix composite materials by tensile test of a* $\pm 45^\circ$ *laminate*, ASTM Standard D 3518, 2007.

[14] Amijima, S. and Adachi, T., "Nonlinear stress-strain response of laminated composites," *Journal of Composite Materials*, vol. 13, no. 3, pp. 206–218, 1979.

[15] Berg, C. A., Tirosh, J., and Israeli, M., *Composite Materials: Testing and Design (2nd Conference), ASTM STP 497*, ch. Analysis of short beam bending of fiber reinforced composites, pp. 206–218. Philadelphia, PA: ASTM, 1972.

[16] Bert, C. W., "Models for fibrous composites with different properties in tension and compression," *Journal of Engineering Materials and Technology - Transactions of the ASME*, vol. 99, no. 4, pp. 344–349, 1979.

[17] Camanho, P. P. and Lambert, M., "A design methodology for mechanically fastened joints in laminated composite materials," *Composites Science and Technology*, vol. 66, pp. 3004–3020, 2006.

[18] Chang, F. K. and Lessard, L. B., "Damage tolerance of laminated composites containing an open hole and subjected to compressive loadings: part I - analysis," *Journal of Composite Materials*, vol. 25, no. 1, pp. 2–43, 1991.

[19] Chang, F. K. and Springer, G. S., "The strengths of fiber reinforced composite bends," *Journal of Composite Materials*, vol. 20, pp. 30–45, 1986.

[20] Chen, J. L. and Sun, C. T., "A plastic potential function suitable for anisotropic fiber composites," *Journal of Composite Materials*, vol. 27, no. 14, pp. 1379–1390, 1993.

[21] Cui, W., Liu, J., Len, J., and Ruo, R., "Interlaminar tensile strength (ILTS) measurement of woven glass/polyester laminates using four-point curved beam specimen," *Composite Part A*, vol. 27A, pp. 1097–1105, 1996.

[22] Cui, W. C., Misnom, M. R., and Jones, M., "Failure mechanisms in three and four point short beam bending tests of unidirectional glass/epoxy," *Journal of Strain Analysis*, vol. 27, no. 4, pp. 235–243, 1992.

[23] Cui, W. C. and Wisnom, M. R., "Contact finite element analysis of three- and four-point short-beam bending of unidirectional composites," *Composites Science and Technology*, vol. 45, no. 4, pp. 323–334, 1992.

[24] Dassault Systèms, *ABAQUS Analysis User's Manual (Version 6.9)*, 2009.

[25] Dobyns, A., Rousseau, C. Q., and Minguet, P., *Comprehensive Composite Materials, Vol.6: Design and Applications*, ch. Helicopter Applications and Design, pp. 223–242. Elsevier Science Ltd., 2000.

[26] Feraboli, A. and Kedward, K. T., "Four-point bend interlaminar shear testing of uni- and multi-directional carbon/epoxy composite systems," *Composites: Part A*, vol. 34, pp. 1265–1271, 2003.

[27] Firswell, M. I. and Mottershead, J. E., *Finite Element Model Updating in Structural Dynamics*. Kluwer Academic Publishers, 1995.

[28] Ghazavi, A. and Gordaninejad, F., "Nonlinear bending of thick beams laminated from bimodular composite materials," *Composites Science of Technology*, vol. 36, no. 4, pp. 289–298, 1989.

[29] Griffin, O. H., Kamat, M., and Herakovich, C. T., "Three-dimensional inelastic finite element analysis of laminated composites," *Journal of Composite Materials*, vol. 15, no. 4, pp. 543–560, 1981.

[30] Hahn, H. T. and Tsai, S. W., "Nonlinear elastic behavior of unidirectional composite laminae," *Journal of Composite Materials*, vol. 7, no. 1, pp. 102–118, 1973.

[31] Hashin, Z., Bagchi, D., and Rosen, B. W., "Non-linear behavior of fiber composite laminates," Tech. Rep. NASA-CR-2313, 1974.

[32] Hiel, C. C., Sumich, M., and Chappell, D. P., "A curved beam test specimen for determining the interlaminar tensile strength of a laminated composite," *Journal of Composite Materials*, vol. 25, pp. 854–868, 1991.

[33] Ho, H. and Morton, J., "Nonlinear numerical analysis of the iosipescu specimen for composite materials," *Composites Science and Technology*, vol. 50, pp. 355–365, 1994.

[34] Jones, R., *Mechanics of Composite Materials*. CRC Press, 1998.

[35] Jones, R. M. and Morgan, H. S., "Analysis of nonlinear stress-strain behavior of fiber-reinforced composite materials," *AIAA Journal*, vol. 15, no. 12, pp. 1669–1676, 1977.

[36] Kedward, K. T., Wilson, R. S., and Mclean, S. K., "The flexure of simply curved composite shapes," *Composites*, vol. 20, no. 6, pp. 527–553, 1989.

[37] Lekhnitskii, S. G., *Anisotropic Plates*. New York: Gordon and Breach Publishers, 1968.

[38] Lekhnitskii, S. G., *Theory of Elasticity of an Anisotropic Body*. Moscow: Mir Publishers, 1981.

[39] Makeev, A., Christopher, I., He, Y., and Shonkwiler, B., "A test method for assessment of shear properties of thick components," *Journal of Composite Materials*, vol. 43, no. 25, pp. 3091–3105, 2009.

[40] Makeev, A., He, Y., Carpentier, P., and Shonkwiler, B., "A method for measurement of three-dimensional constitutive properties for composite materials," *Composites Science and Technology*. Under Review.

[41] Makeev, A., Seon, G., and Lee, E., "Failure predictions for carbon/epoxy tape laminates with wavy plies," *Journal of Composite Materials*, vol. 44, no. 1, pp. 95–112, 2010.

[42] Marwala, T., *Finite Element Model Updating Using Computational Intelligence Techniques: Applications to Structural Dynamics*. Springer, 2010.

[43] Murri, G. B., "Influence of ply waviness on fatigue life of tapered composite flexbeam laminates," Tech. Rep. NASA/TM-1999-209830, ARL-TR-2110, NASA, 1999.

[44] Pagano, N. J., "Analysis of the flexure test of bidirectional composites," *Journal of Composite Materials*, vol. 1, no. 4, pp. 336–342, 1967.

[45] Petit, P. H. and Waddoups, M. E., "A method of predicting the nonlinear behavior of laminated composites," *Journal of Composite Materials*, vol. 3, no. 1, pp. 2–19, 1969.

[46] Ramberg, W. and Osgood, W. R., "Description of stress-strain curves by three parameters," Tech. Rep. No. 902, National Advisory Committee For Aeronautics, 1943.

[47] Reddy, J., *Mechanics of Laminated Composite Plates and Shells: Theory and Analysis*. CRC Press, second ed., 2003.

[48] Renieri, G. D. and Herakovich, C. T., "Nonlinear analysis of laminated fibrous composites," Tech. Rep. VPI-E-76-10, 1976.

[49] Sandhu, R. S., "Non-linear behaviour of unidirectional and angle-ply laminates," *Journal of Aircraft*, vol. 13, pp. 104–111, 1976.

[50] Sandorff, P. E., "Saint-Venant effects in an orthotropic beam," *Composites Science and Technology*, vol. 14, no. 3, pp. 199–212, 1980.

[51] Shivakumar, K., Allen, H., and Avva, V., "Interlaminar tension strength of graphite/epoxy composite laminates," *AIAA Journal*, vol. 32, no. 7, pp. 1478–1484, 1994.

[52] Sullivan, J. L. and Van Oene, H., "An elasticity analysis for the generally and specially orthotropic beams subjected to concentrated loads," *Composites Science and Technology*, vol. 27, no. 2, pp. 133–155, 1986.

[53] Sun, C. T. and Chen, J. L., "A simple flow rule for characterizing nonlinear behavior of fiber composites," *Journal of Composite Materials*, vol. 23, no. 10, pp. 1009–1020, 1989.

[54] Sun, C. T. and Kelly, S. R., "Failure in composite angle structures, part I: initial failure," *Journal of Reinforced Plastics and Composites*, vol. 7, pp. 220–232, 1988.

[55] Sutton, A. M., Orteu, J. J., and Schreier, H., *Image Correlation for Shape, Motion and Deformation Measurements: Basic Concepts, Theory and Applications*. Springer, 2009.

[56] Timoshenko, S. P., *Mechanics of Materials*. Van Nostrand Reinhold Co., 1972.

[57] U.S. Department of Defense, *Military Handbook - MIL-HDBK-17-1F: Composite Handbook, Volume 1 - Polymer Matrix Composite Guidelines for Characterization of Structural Materials*, 2002.

[58] Whitney, J. M., "Cylindrical bending of unsymmetrically laminated plates," *Journal of Composite Materials*, vol. 3, no. 4, pp. 715–719, 1969.

[59] Whitney, J. M., "Elasticity analysis of orthotropic beams under concentrated loads," *Composites Science and Technology*, vol. 22, no. 3, pp. 167–184, 1985.

[60] Whitney, J. M., *Structural Analysis of Laminated Anisotropic Plates*. Technomic Publishing Company, 1987.

[61] Wisnom, M. R., "3-D finite element analysis of curved beams in bending," *Journal of Composite Materials*, vol. 30, no. 11, pp. 1178–1190, 1996.

[62] Wisnom, M. R. and Chang, F. K., "Modeling of splitting and delamination in notched cross-ply laminates," *Composites Science and Technology*, vol. 60, pp. 2849–2856, 2000.

[63] Wisnom, M. R. and Haeberle, J. G., "Prediction of buckling and failure of unidirectional carbon fibre-epoxy composite structures," *Composite Structures*, vol. 28, pp. 229–39, 1994.

[64] Xie, M. and Adams, D. F., "Contact finite element modeling of the short beam test for composite materials," *Computer & Structures*, vol. 57, no. 2, pp. 183–191, 1994.

[65] Xie, M. and Adams, D. F., "A plasticity model for unidirectional composite materials and its applications in modeling composite testing," *Composites Science and Technology*, vol. 54, no. 1, pp. 11–21, 1995.

[66] Xie, M. and Adams, D. F., "Study of three- and four-point shear testing of unidirectional composite materials," *Composites*, vol. 26, no. 9, pp. 653–659, 1995.